

# Bend-Forming: A Deformation Process for In-Space Manufacturing of Truss Structures

by

Harsh Girishbhai Bhundiya

Submitted to the Department of Aeronautics and Astronautics  
in partial fulfillment of the requirements for the degree of

Master of Science in Aeronautics and Astronautics

at the

MASSACHUSETTS INSTITUTE OF TECHNOLOGY

May 2022

© Massachusetts Institute of Technology 2022. All rights reserved.

Author .....  
Department of Aeronautics and Astronautics  
May 17, 2022

Certified by .....  
Zachary C. Cordero  
Boeing Assistant Professor of Aeronautics and Astronautics  
Thesis Supervisor

Accepted by .....  
Jonathan P. How  
R. C. Maclaurin Professor of Aeronautics and Astronautics  
Chair, Graduate Program Committee



# Bend-Forming: A Deformation Process for In-Space Manufacturing of Truss Structures

by

Harsh Girishbhai Bhundiya

Submitted to the Department of Aeronautics and Astronautics  
on May 17, 2022, in partial fulfillment of the  
requirements for the degree of  
Master of Science in Aeronautics and Astronautics

## Abstract

In-space manufacturing (ISM) is a candidate approach for constructing next-generation space structures with larger dimensions than modern deployable systems. While many ISM approaches have been proposed, analysis of their performance for building precision structures on orbit, such as large-diameter reflectors, is scarce. In this thesis, we present a quantitative comparison of materials and processes for ISM, using performance metrics for suitable feedstock materials and a fast and accurate manufacturing method. Our analysis finds that deformation processes are a promising ISM approach due to their low specific energy consumption, almost an order of magnitude lower than melt-based and extrusion processes which rely on heating of the feedstock. This low specific energy consumption potentially enables deformation processes to fabricate 100-meter diameter structures on orbit in less than a day, whereas melt-based processes may take more than a month and be limited to inferior feedstock materials.

Motivated by this comparison of ISM processes, we present an exemplar deformation process, termed Bend-Forming, for fabricating truss structures in space. The method relies on the combination of CNC wire bending with mechanical joints to form trusses from raw feedstock via plastic deformation. We demonstrate the method with exemplar structures on the order of 1 meter and provide a framework for fabricating arbitrary geometries with Bend-Forming, including reticulated columns, shells, and trusses. To guide the design of Bend-Formed structures for space applications, we next investigate the compressive behavior of Bend-Formed isogrid columns through experiments, finding that the structures undergo a smooth formation of buckling deformations. Finite element analyses accurately predict the maximum loads observed experimentally, highlighting the imperfection-insensitive nature of the Bend-Formed columns. Finally, we present a potential space application of Bend-Forming, namely the fabrication of support structure for an electrostatically-actuated reflector antenna. To demonstrate the concept, we design and fabricate a 1-meter diameter antenna prototype with Bend-Forming.

Overall, this research adds to the growing field of ISM by 1) providing a framework for assessing materials and processes suitable for ISM; and 2) introducing a

novel approach for constructing truss structures, called Bend-Forming, with potential application to ISM.

Thesis Supervisor: Zachary C. Cordero

Title: Boeing Assistant Professor of Aeronautics and Astronautics



## Acknowledgments

As they say, it takes a village. I will begin by thanking my research advisor, Prof. Zachary Cordero. I am grateful that he introduced me to this project and for the guidance and mentorship he has provided throughout this work. I look forward to our future collaborations. Next, I would like to thank Prof. Fabien Royer, for his invaluable help and stimulating discussions throughout this research. Also, thanks to the rest of the MIT Wirebenders team, Kaleb Overby and John Zhang, for their collaboration and help. Thanks to Sonny Jeon, Mark Silver, and Will Moulder at MIT Lincoln Laboratory and Prof. Jeffrey Lang for their feedback and input. And many thanks to my undergraduate assistants, Brennan Hoppa and Jack Ansley, for being the workhorses for fabrication of the structures presented in this thesis.

Outside of research, thanks to my friends from MIT Tennis Club for making my time in Boston unforgettable and keeping me (relatively) sane throughout this endeavor. I'm glad to have met such a fun group of friends. Thanks to my AeroAstro friends and lab mates, for our lovely weekly lunches and discussions. Thanks to my roommates, for our cooking sessions and great banter. And finally, thanks to my parents and extended family for their love and support. This thesis is dedicated to my grandparents in India.

## Foreword

The research in this thesis was sponsored by a grant from the MIT Lincoln Laboratory Advanced Concepts Committee (ACC), as well as a gift from Northrop Grumman Corporation.

# Contents

<b>1</b>	<b>Introduction</b>	<b>21</b>
<b>2</b>	<b>Background</b>	<b>24</b>
2.1	Historical Perspective on Large Space Structures . . . . .	24
2.2	Relevant Work on ISM . . . . .	26
2.3	Summary . . . . .	28
<b>3</b>	<b>Engineering Framework for Assessing Materials and Processes for ISM</b>	<b>29</b>
3.1	Introduction . . . . .	29
3.2	Material Considerations for ISM . . . . .	30
3.2.1	Thermal Stability . . . . .	31
3.2.2	Resistance to Disturbance Loads . . . . .	32
3.2.3	Minimal-Mass Buckling Strength . . . . .	36
3.2.4	Summary . . . . .	37
3.3	Process Considerations for ISM . . . . .	39
3.3.1	Energy Required . . . . .	40
3.3.2	Accuracy . . . . .	46
3.4	Material and Process Selection Case Study: ISM of a Tetrahedral Truss	53
3.5	Summary . . . . .	57
<b>4</b>	<b>Bend-Forming: A Deformation Process for ISM of Truss Structures</b>	<b>60</b>
4.1	Introduction . . . . .	60

4.2	Bend-Forming Process . . . . .	61
4.2.1	Finding Bend Paths . . . . .	62
4.2.2	Converting to Machine Instructions . . . . .	67
4.2.3	Joints . . . . .	70
4.3	Exemplar Structures . . . . .	72
4.3.1	Isogrid Column . . . . .	74
4.3.2	Curved Gridshell . . . . .	75
4.3.3	Truss Hoop . . . . .	76
4.3.4	Tetrahedral Truss . . . . .	77
4.3.5	Bunny . . . . .	77
4.4	Summary . . . . .	79
<b>5</b>	<b>Compressive Behavior of Isogrid Columns Fabricated with Bend-Forming</b>	<b>81</b>
5.1	Introduction . . . . .	81
5.2	Methods . . . . .	83
5.2.1	Fabrication of Isogrid Columns . . . . .	83
5.2.2	Experimental Setup . . . . .	83
5.2.3	Finite Element Analysis . . . . .	85
5.3	Results . . . . .	87
5.4	Discussion . . . . .	90
5.4.1	Initial Geometry . . . . .	90
5.4.2	Buckling and Post-Buckling Response . . . . .	91
5.5	Summary . . . . .	98
<b>6</b>	<b>Application of Bend-Forming for Fabricating Support Structure for an Electrostatically-Actuated Reflector Antenna</b>	<b>99</b>
6.1	Introduction . . . . .	99
6.2	Structural Concept . . . . .	101
6.3	Antenna Prototype . . . . .	102
6.3.1	Fabrication . . . . .	103



6.3.2	Finite Element Analysis . . . . .	103
6.3.3	Experiment . . . . .	106
6.4	Summary . . . . .	111
<b>7</b>	<b>Conclusions and Recommendations</b>	<b>113</b>
7.1	Summary and Conclusions . . . . .	113
7.2	Recommendations for Future Work . . . . .	117
<b>A</b>	<b>ISM Case Study Expressions</b>	<b>121</b>
<b>B</b>	<b>Bend-Forming Algorithms</b>	<b>123</b>

# List of Figures

3-1	Exemplar space structures: (a) truss boom supporting the solar panels of the International Space Station (credit: NASA); (b) artist concept of the NISAR spacecraft supporting a large microwave reflector antenna (credit: NASA) . . . . .	30
3-2	Material property diagram for selecting ISM feedstock with thermal stability, plotted for three material classes — metals, polymer/metal–matrix composites, and unfilled plastics [54]. Materials toward the upper left corner are thermally stable and undergo the least distortion in the presence of a through-thickness temperature gradient. Note all material properties are at room temperature. . . . .	33
3-3	Material property diagram for selecting ISM feedstock with minimal distortion from harmonic disturbance loads, plotted for the same materials as Fig. 3-2 [54]. Structures fabricated with materials toward the upper right corner have minimal distortion due to both high damping and high natural frequency. A trade-off between damping and stiffness is observed. . . . .	35
3-4	Material property diagram for selecting ISM feedstock with minimal-mass buckling strength, plotted for the same materials as Fig. 3-2 [54]. Materials in the upper left corner are optimal for buckling due to their superior combination of Young’s modulus, tensile strength, and density.	37

3-5	A comparison of specific energy consumption for three ISM processing methods: melt-based processing, extrusion of carbon fiber-reinforced thermoplastics/thermosets (with 50% fiber weight fraction), and deformation processing [54]. Each process is represented by a different color, and its specific energy consumption is plotted for relevant feedstock materials, including composites, metals, and plastics. For many materials, the energy consumption of deformation processing is the lowest. . . . .	44
3-6	Model setup of a thermomechanical simulation of an extruding CF/epoxy tube in space. Extrusion is simulated with a moving temperature boundary on a fixed-length beam. On the one side of the boundary, the tube is rigid and at fixed temperature; on the other side, it is subject to temperature boundary conditions which simulate the space environment. . . . .	48
3-7	Simulation results for extrusion of a partially cured CF/epoxy tube into space, modeled with COMSOL Multiphysics [69]. The extrusion velocity, nozzle temperature, and initial degree of cure are $v = 5$ mm/s, $T_0 = 450$ K, and $\xi_0 = 0.38$ , respectively. The extrusion is modeled for the first 200 s; afterward, the tube is subject to solar heat flux on its top surface and radiation to a low ambient temperature. (a)-(c) plot the average surface temperature, average surface degree of cure, and tip deflection as a function of time, while (d)-(f) show their distributions along the tube at the end of the simulation. Gradients in temperature and degree of cure across the cross section cause deflection at the tip.	49
3-8	Evolution of curvature in an extruding CF/epoxy tube from thermal expansion and chemical shrinkage, separately. . . . .	51
3-9	Effect of the nozzle temperature $T_0$ on (a) the average surface temperature, (b) average surface degree of cure, and (c) curvature of an extruding CF/epoxy tube in space. Generally, a higher nozzle temperature decreases curvature after extrusion. . . . .	52

3-10	Tetrahedral truss geometry, adapted from [4]. This layered truss structure is made of equal-length struts and is formed by repeating a tetrahedral unit cell to create rings. The resulting structure is hexagonal and supports a flat, faceted reflector. . . . .	53
3-11	(a) Approximate mass of a tetrahedral truss as a function of diameter between 10 m and 100 m, plotted for five candidate ISM feedstock materials. CFRP feedstocks yield the lowest truss mass, followed by aluminum-matrix composites and metals. (b) Truss fundamental frequency as a function of diameter. CFRP feedstocks yield the highest natural frequencies. . . . .	54
3-12	Approximate build times of a tetrahedral truss as a function of diameter, for various candidate ISM materials and processes. Deformation processes (denoted by def) generally achieve faster build times than extrusion (ext) or melting (melt) processes due to lower specific energy consumption. Note that while the specific energies required to deform Invar and CF/Al are different, their build time is similar since it is dominated by the time spent feeding material, which we model in Eq. 3.21 as independent of the feedstock material. . . . .	56
4-1	The Bend-Forming unit process, illustrated for a pentagon. With a single degree-of-freedom (DOF) bend head, planar trusses can be fabricated; if an additional out-of-plane rotational DOF is added to the bend head, 3D trusses can be fabricated. Note that this illustration is based off the D.I. Wire Pro machine [76]. . . . .	61

4-2 Block diagram for fabricating 2D or 3D truss structures with Bend-Forming. The first step (in yellow) is to find a continuous bend path through the desired truss geometry. This is achieved using the route inspection algorithm from graph theory. The second step (in orange) is to convert the bend path into instructions for a CNC wire bending machine. This is achieved via a geometric algorithm which uses the truss nodal coordinates. . . . . 62

4-3 The first step of the Bend-Forming process, illustrated for a 2D circular truss and a 3D bunny truss. Here the route inspection algorithm is used to find a continuous bend path for the desired truss. First the Make Eulerian algorithm adds doubled struts to the geometry until only two nodes remain with odd connectivity (highlighted in red). These doubled struts are visualized as curved black edges superimposed on the original geometry. Then the Hierholzer algorithm finds a continuous bend path which traverses each edge of the truss. Note the path found by this algorithm is not unique as many exist for the same geometry. Here one bend path is visualized with green arrows between the start and end nodes. The code for these algorithms can be found in Appendix B and in [75]. . . . . 64

4-4 Typical degrees of freedom for a CNC wire bender. Assuming a 2-DOF bend head, the machine can feed along the wire axis ( $L_{feed}$ ), bend clockwise or counterclockwise in the xy-plane ( $\pm\theta_{bend}$ ), and rotate out-of-plane about the feeding axis ( $\theta_{rotate}$ ). To avoid collision with the feedstock and the fabrication plane of the machine, the bend angle and rotation angle are restricted to  $0 \leq \theta_{bend}, \theta_{rotate} \leq 180^\circ$ . . . . . 67

4-5	The second step of the Bend-Forming process, illustrated for a 2D circular truss and a 3D bunny truss. Here a geometric algorithm is used to convert a continuous bend path into a series of feed, bend, and rotate instructions for a typical CNC wire bender. These instructions are then used to fabricate the desired truss from a spool of raw feedstock. The code for this algorithm can be found in Appendix B and in [75]. . . .	68
4-6	Illustration of the geometric algorithm for converting a simple bend path with four nodes ( $x_1$ - $x_4$ ) into a series of machine instructions. The feed length $L_{feed}$ is computed as the Euclidean distance between subsequent nodes. The bend angle $\theta_{bend}$ is computed using the angle between every three nodes in the bend path ( $\alpha_i$ ). Finally the rotation angle $\theta_{rotate}$ is computed using normal vectors to the current and next planes of the path ( $\hat{n}_{current}$ and $\hat{n}_{next}$ ). Note that the black arrows show the progress of the fabricated truss as the machine instructions are implemented. . . . .	69
4-7	Examples of low-power joining methods compatible with Bend-Forming: (a) snap-fit joints which rely on interference and (b) soldered joints. Here the snap-fit joints are made of plastic and 3D printed using a stereolithography (SLA) printer [84]. . . . .	71
4-8	Exemplar 3D truss structures fabricated with Bend-Forming: (a) 1-m long isogrid column, (b) 1-m diameter curved gridshell, (c) 1-m diameter truss hoop, (d) 0.2-m wide tetrahedral truss, and (e) 0.3-m tall bunny. Each prototype is made from a single, continuous steel wire using a desktop CNC wire bending machine [76]. The nodes consist of either soldered joints or 3D-printed joints which snap together with interfering pins (see inset images). . . . .	73

4-9	Geometry and bend path for an isogrid column fabricated with Bend-Forming. The 3D geometry is first unrolled about a spiral edge (in red). Then a zig-zag bend path is computed (illustrated with green arrows) and converted to machine instructions. Once fabricated, the 2D geometry is rolled about the cylinder axis to obtain an isogrid column.	74
4-10	Geometry and bend path for a curved gridshell fabricated with Bend-Forming. First the 3D geometry is flattened using angular defects ( $\beta_i$ ). Then a continuous bend path is computed through the 2D geometry and converted to machine instructions for fabrication. . . . .	76
4-11	Geometry and bend path for a truss hoop fabricated with Bend-Forming. A 3D bend path is computed for the hoop which completely traverses each bay before moving to the next. The continuous bend path is then converted to machine instructions for fabrication. . . . .	77
4-12	Geometry and bend path for a tetrahedral truss fabricated with Bend-Forming. A 3D bend path is computed for the truss and converted to machine instructions for fabrication. . . . .	78
4-13	Geometry and bend path for a bunny fabricated with Bend-Forming. A 3D bend path is computed for the truss and converted to machine instructions for fabrication. . . . .	78
5-1	Four isogrid columns fabricated with Bend-Forming, using 1-mm diameter steel wire and plastic snap-fit joints. Each column was tested in compression, with only one geometric parameter varied between columns: diameter, height, or triangle sidelength. The baseline column was spray-painted white for shape measurement with a white light 3D scanner. . . . .	84
5-2	Boundary conditions for compression of Bend-Formed isogrid columns. (a) Both sides of the column are embedded in epoxy-filled endcaps. (b) Load is applied with a marble to minimize effects of any tilt misalignment.	85

5-3	Illustration of the finite element analysis for compression of Bend-Formed isogrid columns. (a) Rotational boundary conditions are applied to roll the 2D triangular lattice into a cylinder. (b) Kinematic constraints are applied to merge the leftmost and rightmost nodes and compute the equilibrium state of the column. (c) A compressive force is applied at the top of the column. . . . .	86
5-4	Experimental results for compression of four Bend-Formed isogrid columns. The load-displacement curve is plotted for each column with images at three points during the test. The locations of the largest-amplitude deformations are highlighted with red arrows. All four columns display an initially linear response, followed by nonlinear softening, and a gradual decrease of the load which corresponds the formation of localized deformations along the height of the column. . . . .	89
5-5	Shape deviations between the simulated and actual shape of a Bend-Formed isogrid column. The simulated shape is calculated through a finite element analysis while the actual shape is measured using a white light 3D scanner [104]. The maximum deviations occur near the top of the column. . . . .	90
5-6	Buckling eigenmodes of the baseline isogrid column, computed using a linear buckling analysis in Abaqus. (a) Primary eigenmodes of the baseline column, only one of which is axisymmetric. (b) Secondary eigenmode calculated using an iterative solver. . . . .	92
5-7	Comparison of the load-displacement curve for the baseline column, obtained via experiment (dotted) and simulation (red and blue). Here F1 - F4 correspond to the various buckling eigenvalues of the structure. The blue path is obtained by seeding the initial geometry with the first eigenmode (F1) while the red path is obtained by using the secondary eigenmode (F4) as the imperfection. Deformed shapes at the end of the simulation are shown in (b) and (c). . . . .	93



5-8	Comparison of load-displacement curves for three Bend-Formed isogrid columns, obtained via experiment (dotted) and simulation (solid). The simulated post-buckling paths match well with experimental results, as do the maximum loads. Deformed shapes at the end of the simulations are shown in (d)-(f). . . . .	96
6-1	Illustration of an electrostatically-actuated reflector antenna. The curved reflector surface is achieved via distributed electrodes on a command surface, which deforms a thin membrane into the target shape. Note this illustration is adapted from [113]. . . . .	100
6-2	Structural concept for an electrostatically-actuated reflector antenna fabricated with Bend-Forming. On the left, an illustration of the conductive membrane and command surface attached to the support structure. On the right, a perspective and side view of the supporting truss structure fabricated with Bend-Forming. . . . .	102
6-3	Fabrication process for Bend-Formed support structure of an electrostatically-actuated reflector antenna. A continuous bend path (a) which traverses both the truss hoop and inner triangular grid is converted to machine instructions for a CNC wire bender, resulting in the fabricated prototype shown in (b). Here soldered joints are used at each node. . . . .	104
6-4	Finite element model for compression of the Bend-Formed support structure, with both radial and vertical components of the mesh tension. The load is applied at each attachment point, and simply supported boundary conditions are applied at the outer nodes of the truss hoop. The buckling eigenvalues are found via a linear analysis about the undeformed structure, and a post-buckling path is obtained with the Riks solver by seeding the initial geometry with the first buckling eigenmode. . . . .	105

6-5	Buckling eigenvalues for radial and vertical loading on the Bend-Formed support structure. Here the eigenvalue is the load applied at each attachment point of the perfect structure to cause a bifurcation. . . . .	106
6-6	Simulated load-displacement curve for radial loading of the Bend-Formed support structure, measured at the labeled node. Here the y-axis represents the radial load applied at each attachment point of the truss hoop. The deformed shape depicts buckling of the circumferential struts as well as struts in the triangular cross section of the truss hoop. . . . .	107
6-7	Truss hoop fabricated with Bend-Forming, experimentally tested for radial compression with a whiffle tree experimental setup. . . . .	108
6-8	Experimental and simulation setups for radial compression of a truss hoop fabricated with Bend-Forming. A whiffle tree setup with pulleys and spreader bars is used to translate the vertical displacement of the crosshead into radial displacement at each attachment point. In the simulation, we apply concentrated radial loads at each attachment point and use simply support boundary conditions at the outer nodes of the truss hoop. . . . .	108
6-9	Experimental results for radial compression of a truss hoop fabricated with Bend-Forming. The structure achieves a maximum load of $P_{max} = 189$ N before sequential buckles form on the right side of the hoop (highlighted with red arrows). The final drop in load occurs when a soldered joint breaks (highlighted with the red circle). . . . .	109
6-10	Simulation results for radial compression of a truss hoop fabricated with Bend-Forming. On the left, the first buckling eigenmode of the perfect structure. On the right, five simulated post-buckling paths, using the first buckling eigenmode as an imperfection on the initial geometry with varying amplitudes, and images of the deformed shape. . . . .	110

# List of Tables

3.1	Candidate ISM feedstock materials for optimizing performance of a large space structure, particularly thermal stability, resistance to disturbance loads, and minimal-mass buckling strength. Materials which maximize the listed material indices are highlighted in bold. . . . .	38
3.2	Material properties used for the exemplar CF/epoxy composite CY-COM 5320-1. The density ( $\rho$ ), specific heat ( $C_p$ ), and longitudinal, transverse thermal conductivities ( $k_1, k_2$ ) are obtained via rule of mixtures. The heat of the reaction ( $H_r$ ) is used as an exothermic heat source during curing. All other orthotropic elastic constants are obtained from [70]. . . . .	48
4.1	Fabrication details for exemplar structures fabricated with Bend-Forming shown in Figure 4-8. Note that the listed mass includes both the wire and the joints. . . . .	72
5.1	Geometric parameters of four Bend-Formed isogrid columns tested in compression. Note some values are expressed as ranges due to tolerance stack-up during fabrication. . . . .	84
5.2	Experimentally measured axial stiffness and maximum compressive load of four Bend-Formed isogrid columns. . . . .	88
5.3	Relative error between experimental and simulated values of axial stiffness and maximum load for Bend-Formed isogrid columns tested in compression. The simulation consistently overpredicts the axial stiffness but accurately predicts the maximum load. . . . .	95



# Chapter 1

## Introduction

Large space structures have been of interest for decades due to the performance benefits they offer for various space missions: communications [1, 2], remote sensing [3], astronomy [4], power generation [5], and propulsion [6]. A prime example of the enabling capabilities of large space structures is in remote sensing, where reflectors with diameter greater than 100 meters could enhance the gain, sensitivity, and spatial resolution of existing systems as well as enable new sensing applications, such as microwave radiometry in geostationary orbit for continuous climate monitoring [7]. Performance benefits are also expected in communications, where larger reflectors could enable higher data rates and smaller ground station antennas [1]; in power generation, where larger support structure could enable MW-scale space solar power stations [8]; and in propulsion, where kilometer-scale membranes could enable solar sails to reach previously inaccessible orbits [6].

Given the performance benefits offered by large space structures, various approaches have been explored for achieving such systems in space. Today, the state-of-the-art approach for achieving large space structures is through deployable systems, which are tightly packaged before launch and unfurl into a larger volume on orbit. For instance, deployable booms made of high-strain composites are routinely used to deploy optics, solar arrays, and solar sails [9, 10, 11]. Further, deployable antennas such as the AstroMesh have decades of flight heritage for communication and radar satellites [12].

While such deployable systems have been used extensively in space, they do have limitations, especially as their size increases. For instance, deployable structures are generally designed to withstand launch loads, which adds weight to the spacecraft; they are costly, due to the testing and integration required to ensure successful deployment; and their size is limited by the packaging and precision constraints of the deployed shape. Indeed, modern deployable reflector antennas exhibit a trade-off between surface precision and diameter, which has limited their practical size to tens of meters [13]. Additionally, composite deployable booms undergo stress relaxation during stowage [14], which affects their precision and decreases reliability.

Given these challenges, there is growing interest in a new paradigm for constructing large structures on orbit, called in-space manufacturing (ISM). ISM refers to launching raw feedstock to space along with a robotic system which manufactures the desired structure using power on orbit. The key advantages of this approach are that it allows fabrication of structures optimized for the space environment; it enables mission flexibility through on-demand fabrication; and with enough feedstock, it can construct larger structures than can be deployed with systems today.

A wide range of feedstock materials and processing methods have been proposed for ISM. Some examples include: additive manufacturing of structures from metallic and fiber-reinforced composite feedstocks [15, 16]; extrusion of fiber-reinforced plastics with high specific stiffness and strength [17, 18]; and deformation processing of complex structures through plastic deformation [19, 20]. However, there has been no systematic comparison of the relative benefits of each approach, making it difficult to determine the optimal ISM approach for a given application. Hence in this thesis, we contribute to the growing field of ISM by 1) providing an engineering framework for assessing materials and processes suitable for ISM; and 2) introducing a novel approach for constructing truss structures called Bend-Forming, with potential application to ISM.

The work is organized as follows. Chapter 2 summarizes previous work relevant to both large space structures and in-space manufacturing. Chapter 3 presents a quantitative comparison of materials and processes for ISM, using performance met-

rics for suitable feedstock materials and a fast and accurate manufacturing method. This analysis highlights specific materials suited for ISM and finds that deformation processing is a promising ISM approach due to its low specific energy consumption.

Motivated by this analysis, Chapter 4 presents a deformation process for fabricating truss structures from a spool of raw feedstock, with potential application to ISM. The method, called Bend-Forming, relies on CNC wire bending and mechanical joints to form trusses via plastic deformation. We demonstrate the method with exemplar structures on the order of 1 meter and provide a framework for fabricating arbitrary geometries with Bend-Forming, including reticulated columns, shells, and trusses.

To guide the design of Bend-Formed structures for space applications, Chapter 5 investigates the mechanical behavior of columns fabricated with Bend-Forming. In particular, we conduct compressive tests on Bend-Formed isogrid columns with varying geometries to understand their buckling and post-buckling behavior. These experiments show that the structures undergo a smooth formation of buckling deformations, and that contrary to thin cylindrical shells, they do not exhibit an abrupt destabilization past their first bifurcation. With finite element models, we accurately predict the maximum loads the columns can withstand, highlighting the imperfection-insensitive nature of the Bend-Formed columns.

Next, Chapter 6 introduces a potential space application of Bend-Forming, namely the fabrication of support structure for an electrostatically-actuated reflector antenna. We demonstrate a structural concept for this application by fabricating a 1-meter diameter antenna prototype with Bend-Forming. We also verify the structural design with finite element simulations and a preliminary experiment for applying radial compression to the structure. Finally, Chapter 7 concludes the thesis with a summary and recommendations for future work.

# Chapter 2

## Background

### 2.1 Historical Perspective on Large Space Structures

Large space structures have been of interest for decades, and various approaches have been studied in the past. Of the many applications of large space structures, large-diameter reflector antennas have received the most interest because of their practical significance for communication and sensing satellites. Multiple structural designs have been proposed and tested for this application, including designs which rely on inflatable structures [21, 22], orbital assembly [23, 24], in-space manufacturing [19, 20], and deployable structures [25, 26, 27].

The first large inflatable designs to be tested were metallized balloon satellites launched as part of Project Echo in the 1960s [21]. These balloons expanded to a diameter of up to 40 meters on orbit and served as passive antennas, successfully reflecting microwave transmissions across the United States. Later, the Space Shuttle was used as a platform for demonstrating concepts for in-space assembly (ISA). One such concept proposed using the manipulator arm to assemble small truss modules into a large curved aperture [23], while another concept relied on astronauts assembling struts into a large mast during extravehicular activities (EVAs). In 1985, in-space manual assembly was first demonstrated when two astronauts assembled a 14-meter long truss outside the Shuttle bay in 25 minutes [24]. Research into such ISA concepts culminated in the assembly of the largest space structure to date, the



International Space Station.

Other approaches, known as in-space manufacturing (ISM), considered the use of a robot in space to form feedstock into desired shapes. At the end of the 1970s, two such concepts culminated in ground demonstrations: the Grumman Beam Builder which constructed long metallic trusses by forming and spot-welding thin strips of aluminum [19]; and SCAFEDS which constructed trusses out of a graphite fiber-reinforced plastic by roll forming and ultrasonic welding [20]. Both these systems were envisioned to manufacture trusses up to 300 meters in length on orbit, for applications such as large solar arrays and antennas.

Finally, many deployable designs for large antenna reflectors have also been developed. Some examples include the radial-rib antenna, which unfurls similar to an umbrella [25]; the wrap-rib antenna, which deploys by unraveling thin ribs wrapped around a central hub [26]; and the tension truss antenna, which supports a faceted parabolic mesh with tensioned ties [27]. As systems lending themselves to meaningful ground-based demonstrations, these concepts have matured significantly, enabling the largest antennas on orbit today.

Despite decades of research on these various approaches to large structures in space, today there are only a few examples of structures with dimensions greater than 35 meters, due to challenges with high costs, complex designs, and decreasing performance. For instance, concepts for manual assembly of large trusses were abandoned due to the costs and risks of extended EVAs, such as astronaut fatigue during assembly [24]. Concepts for robotic assembly were not realized due to the low technology readiness level for assembling hierarchical struts and joints [24]. Likewise, concepts for in-space manufacturing were hampered due to the unreliability of manufacturing processes, high energy consumption of operations like welding, and concerns of thermally induced strains during fabrication [24, 28]. While some early deployable and inflatable designs have been adapted for modern reflector antennas, original designs for 100-meter scale structures have also been difficult to implement because of issues with the accuracy and reliability of deployment mechanisms [14], excessive support structure required to survive launch loads, and thermal distortions in

the space environment, which cause unwanted surface error and degrade performance. Indeed, modern deployable reflectors exhibit a trade-off between surface precision and diameter, which has limited their practical size to tens of meters [13].

## 2.2 Relevant Work on ISM

With this historical backdrop in view, rapidly decreasing launch costs and recent advances in controls and robotics have given rise to resurgent interest in constructing large space structures, especially via in-space manufacturing (ISM). This approach offers the unique opportunity for on-demand fabrication of structures optimized for the space environment. Recent analytical models [29, 30, 31] have found three specific applications of ISM which could offer significant mass and cost savings for current mission architectures: on-demand spares manufacturing, large external structure manufacturing, and planetary surface infrastructure manufacturing. The first refers to the fabrication of spare parts and tools for long-duration missions, for which ISM approaches offer large mass savings by eliminating the need to carry spares during launch [29]. The second refers to the fabrication of large support structures in space, for which ISM offers the largest cost savings by enabling the construction of large-diameter antennas in geostationary orbit [30]. Finally, the third application of ISM refers to the in-situ fabrication of infrastructure on planetary surfaces, which can enable long-duration missions for human spaceflight and planetary exploration [31].

These promising applications have stimulated both government and commercial interest in developing technologies for ISM. Guided by the national strategy for in-space servicing, assembly, and manufacturing [32], NASA is currently pursuing two missions, termed OSAM-1 and OSAM-2, to demonstrate manufacturing in space. These spacecraft, set to launch in 2025, will test the robotic assembly of a 3-meter diameter reflector antenna, as well as extrusion of a 10-meter long composite boom on orbit [33, 34]. The European Space Agency (ESA) has developed its own strategy for ISM, pursuing projects through the “Out of Earth Manufacturing” initiative, such as additive manufacturing of metals in microgravity and construction of infrastructure

from lunar regolith [35, 36]. The China National Space Administration (CNSA) is also investigating methods for constructing large structures on orbit, for space-based solar power stations and human spaceflight missions [37].

In industry, various companies are pursuing ISM concepts for fabrication of on-demand spares, large support structures, and planetary surface infrastructure. For manufacturing of on-demand spares, Redwire Space (formerly Made In Space) has developed the Additive Manufacturing Facility, which is capable of 3D printing polymer parts via fused deposition modeling. Commercially operating since 2016 aboard the International Space Station (ISS), the facility has produced over 200 components for both government and commercial customers [38]. The same company has also developed the Ceramics Manufacturing Module aboard the ISS for manufacturing ceramic components using stereolithography [39], as well the BioFabrication Facility for manufacturing human tissue in microgravity [40]. Future plans seek to increase the build volumes of these systems and to achieve multi-material additive manufacturing in space, with combined metal, composite, and polymer feedstocks [41].

For construction of large space structures, many approaches have been proposed since the original NASA beam builders developed in 1979. Tethers Unlimited, for instance, has developed a robotic system for extrusion of composite trusses from comingled yarn of carbon fiber and polyether ether ketone (PEEK) [17], demonstrated on the ground in 2017. Redwire Space has also developed a system for fused deposition modeling of beams from carbon fiber-reinforced thermoplastic polymers [16]. This process will soon be demonstrated in space with the fabrication of two 10-meter long beams, as part of the NASA OSAM-2 mission [34]. Other recent concepts for constructing large space structures include robotic assembly of metal beams for commercial space stations [42, 43], as well as self-assembling tiles which reconfigure into large apertures using electromagnetic forces [44].

Finally, given the recent emphasis on human planetary exploration of the Moon and Mars, technologies are under development for in-situ fabrication of infrastructure on planetary surfaces. For instance, the Zero Launch Mass 3D Printer developed by KSC Swamp Works fabricates structures from regolith simulant and a thermoplastic

binder, using big area additive manufacturing (BAAM) [45]. Another concept, the MARSHA prototype developed by AI SpaceFactory [46], uses a similar BAAM process with basalt fiber and polylactic acid (PLA) and won first place at the NASA 3D Printed Habitat Centennial Challenge in 2019. Yet another concept, the MIRA3D, envisions additive layer manufacturing of lunar regolith using a robotic arm which directly heats the feedstock material [47].

## 2.3 Summary

In summary, constructing large structures in space has been of interest since the beginning of the space age, but early concepts for 100-meter scale structures were abandoned due to technical challenges with fabrication in the space environment, as well as the maturing technology of deployable structures. Today, there is a resurgent interest in in-space manufacturing (ISM), particularly for the applications of fabricating on-demand spares, large support structures on orbit, and infrastructure on planetary surfaces. Numerous approaches have been proposed for these applications, with varying levels of maturity and technological readiness for fabrication in space. Given this burgeoning field of ISM, in this thesis we provide guidelines for assessing feedstock materials and processes for ISM, as well as introduce a new approach for fabricating truss structures from raw feedstock, particularly for the construction of large support structures on orbit.

# Chapter 3

## Engineering Framework for Assessing Materials and Processes for ISM

### 3.1 Introduction

While many approaches have been proposed for manufacturing structures in space, there has been no comparison of the various potential feedstock materials and manufacturing processes, making it difficult to select an optimal ISM approach for a given application. Hence, in this chapter we pursue a system-level comparison of materials and processes suitable for ISM, using relevant performance metrics for precision space structures such as the examples shown in Fig. 3-1. By using material indices for thermal stability, resistance to disturbance loads, and minimal-mass buckling strength, we identify specific metals, composites, and polymers as candidate construction materials for ISM of such structures. Correspondingly, using the process metrics of energy consumption and accuracy, we compare manufacturing processes amenable to ISM. We then apply these material and process considerations in a case study on ISM of a large tetrahedral truss supporting a reflector surface. This analysis highlights deformation processing as a promising ISM method which has low energy consumption and limited thermal distortion during forming. Note that this chapter is adapted from the published article in [48].

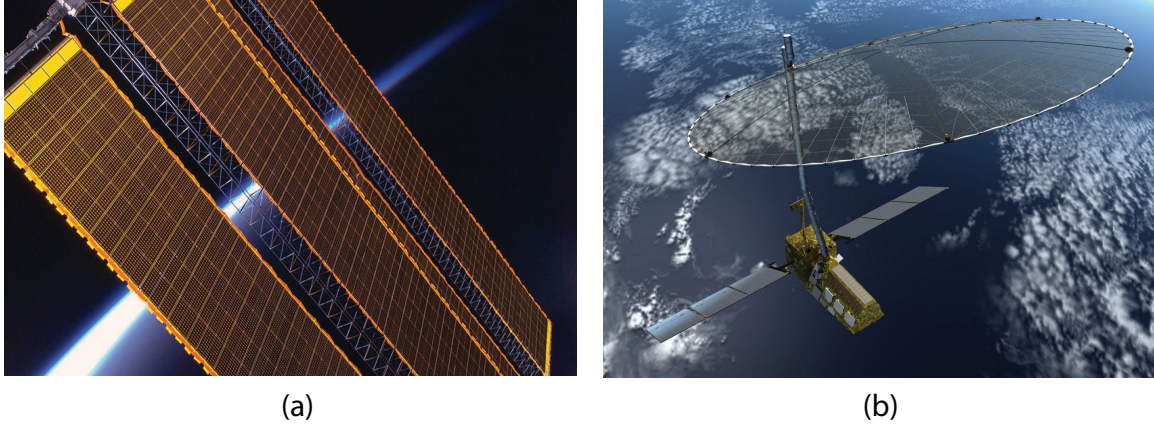


Figure 3-1: Exemplar space structures: (a) truss boom supporting the solar panels of the International Space Station (credit: NASA); (b) artist concept of the NISAR spacecraft supporting a large microwave reflector antenna (credit: NASA)

### 3.2 Material Considerations for ISM

We first identify candidate construction materials for ISM of an exemplar structure: a large curved reflector like the one shown in Fig. 3-1b. For such an application, the key design objective is to maintain a specified gain and resolution during the lifetime of the mission. In the space environment, however, there are many sources of inaccuracy which can degrade antenna performance. There are surface distortions from thermal gradients during orbit, which become amplified for larger apertures [49]; there is unwanted deformation from quasi-static and periodic loads, such as from slewing and attitude control [4]; and there are local compressive loads which cause buckling of individual struts [50]. Given these challenges, the optimal design for a reflector antenna would be one in which (1) surface errors from thermal distortion are minimized; (2) surface errors from inertial and periodic disturbances are minimized; and (3) individual members have maximum buckling strength per unit mass. To identify construction materials which satisfy these performance requirements, we use groupings of material properties, termed material indices, originally developed by Ashby and co-workers [51]. These indices serve as quantitative guides in material selection for engineering design, as optimal materials for a given application are generally those which achieve extremal values of a cost function whose inputs are material indices. In

what follows, we use material indices to determine which materials are most suitable for ISM feedstock. Of course, the native performance of structures made from these materials could be enhanced via coatings, active control, and other complementary methods.

### 3.2.1 Thermal Stability

Thermal distortions in a large space structure generally result from through-thickness temperature gradients during orbit [49, 52]. To mitigate such distortions, materials must be chosen which have minimal distortion in the presence of a temperature gradient. The relevant material index can be determined by considering a simple conduction model of a simply-supported beam of length  $L$  and thickness  $h$ , heated on one side with a fluctuating heat flux of magnitude  $q$ . Assuming the period of fluctuations is greater than the thermal response time of the beam, a steady-state temperature distribution  $T(y)$  will develop through the beam thickness. For an unconstrained beam, this will cause a curvature to develop, with magnitude [53]

$$\kappa = \alpha \frac{dT}{dy} = \frac{\alpha}{\lambda} q. \quad (3.1)$$

Here  $\alpha$  is the coefficient of thermal expansion, and Fourier's Law is used to rewrite the temperature gradient in terms of the incoming heat flux  $q$  and the beam thermal conductivity  $\lambda$ . By integrating the curvature twice and using simply-supported boundary conditions, the central transverse deflection of the beam is obtained as

$$\delta_{max} = \frac{1}{8} q L^2 \left( \frac{\alpha}{\lambda} \right). \quad (3.2)$$

From Eq. 3.2, minimizing the thermal distortion requires maximizing the material index

$$M_1 = \frac{\lambda}{\alpha}. \quad (3.3)$$

We seek materials which maximize this performance metric for thermal stability.

To this end, Fig. 3-2 shows the relevant material property diagram, which plots the thermal conductivity  $\lambda$  against the thermal expansion coefficient  $\alpha$  for a wide range of ferrous and non-ferrous metals, polymer and metal–matrix composites, and unfilled thermoplastics and thermosets. Figure 3-2 shows a contour line for the material index  $M_1$  with slope of 1. This line serves as a guide for selecting materials with minimal thermal distortion, and it can be shifted across the plot to identify materials which have the same value of  $M_1$ . To select materials which perform best, a line is picked which isolates a search area containing a small number of candidates, as depicted in Fig. 3-2. Inspection of Fig. 3-2 shows that among metals, copper alloys, beryllium, and Invar are attractive feedstock materials with minimal thermal distortion. Among composites, the metal–matrix composite of carbon fiber/aluminum is an optimal choice, given its remarkably high thermal conductivity. Other good feedstock candidates are SiC/aluminum, carbon fiber/PEEK, and carbon fiber/epoxy. Comparatively all unfilled polymers have low thermal stability, but among thermoplastics, polyetherketoneketone (PEKK) and self-reinforced polyphenylene (SRP) perform best; and among thermosets, polyimides (PI) perform best.

### 3.2.2 Resistance to Disturbance Loads

Next consider the objective of minimizing distortion of a fabricated space structure from disturbance loads. For a large space antenna, unwanted surface error can result when the structure accelerates in response to slewing, attitude control, or gravity gradient loads. If such loads are harmonic, Lake et al. showed that the upper bound on rms surface error ( $x_{rms}$ ) of a passive structure is given by [4]

$$x_{rms} \leq \frac{a_{rms}}{4\pi^2 f_0^2}, \quad (3.4)$$

where  $a_{rms}$  is the rms magnitude of the accelerations, and  $f_0$  is the fundamental natural frequency of the structure. Equation 3.4 shows that minimizing surface error from disturbance loads requires maximizing the fundamental natural frequency of the structure. Modeling the aperture of a space antenna as a flat, isotropic circular plate



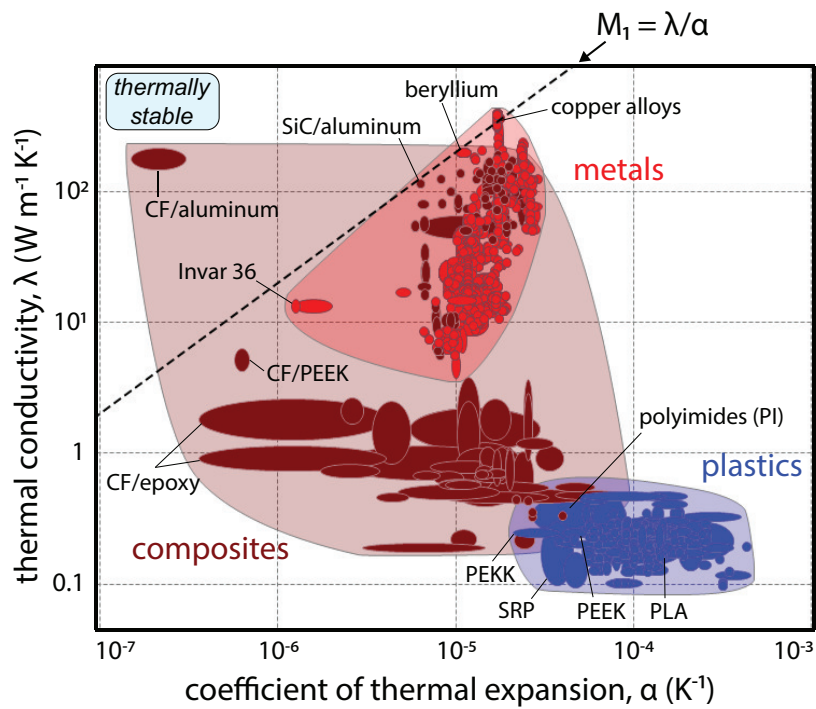


Figure 3-2: Material property diagram for selecting ISM feedstock with thermal stability, plotted for three material classes — metals, polymer/metal–matrix composites, and unfilled plastics [54]. Materials toward the upper left corner are thermally stable and undergo the least distortion in the presence of a through-thickness temperature gradient. Note all material properties are at room temperature.

with fixed diameter and bending stiffness but varying depth, the relevant material index which maximizes its natural frequency is [53]

$$M_u = \left( \frac{E^{1/3}}{\rho} \right)^{1/2}. \quad (3.5)$$

The above material index, a function of the Young's modulus  $E$  and density  $\rho$ , does not consider damping, as it assumes the harmonic loads do not excite the natural frequencies of the structure. However, if the excitation covers a wide frequency range which includes the resonant frequencies of the structure, damping becomes important. In that case, a relevant material index can be derived by considering the passive damping of the feedstock through the material loss coefficient  $\eta$  [53]. The resulting material index is

$$M_2 = \eta M_u^{k-1}, \quad (3.6)$$

where the constant  $k$  (typically greater than 2) describes the power spectral density of the excitation. In particular,  $k = 2$  represents a disturbance with constant input velocity and finite power;  $k > 2$  represents an excitation more concentrated at low frequencies; and  $k \rightarrow \infty$  represents a disturbance that does not excite any resonant frequencies. In this way, the constant  $k$  represents the relative importance of the material damping  $\eta$  to the material index  $M_u$  for maximizing natural frequency. The smaller the value of  $k$ , the closer the excitation to the resonant frequencies and the more important the inherent damping. Note that Eq. 3.6 only considers passive damping of the feedstock. For a large structure, the damping from mechanical interfaces and the resulting interface friction will ultimately contribute greater damping which is not considered by this simplified material index. Nonetheless, a larger value of  $k$  can represent the increased importance of maximizing natural frequency in such cases.

To identify materials which maximize this performance metric for minimal distortion, we plot the relevant material property diagram in Fig. 3-3. Here the material index  $M_u$ , which represents the maximum natural frequency achievable for a flat

plate, is plotted against the material loss coefficient  $\eta$ , a measure of energy dissipated per loading cycle. To guide material selection, a contour line for  $M_2$  with a slope of  $1/(1 - k)$  is overlaid. Here we use a value of  $k = 2$ , corresponding to a disturbance with finite power and a scenario where material damping is as important as maximizing the natural frequency.

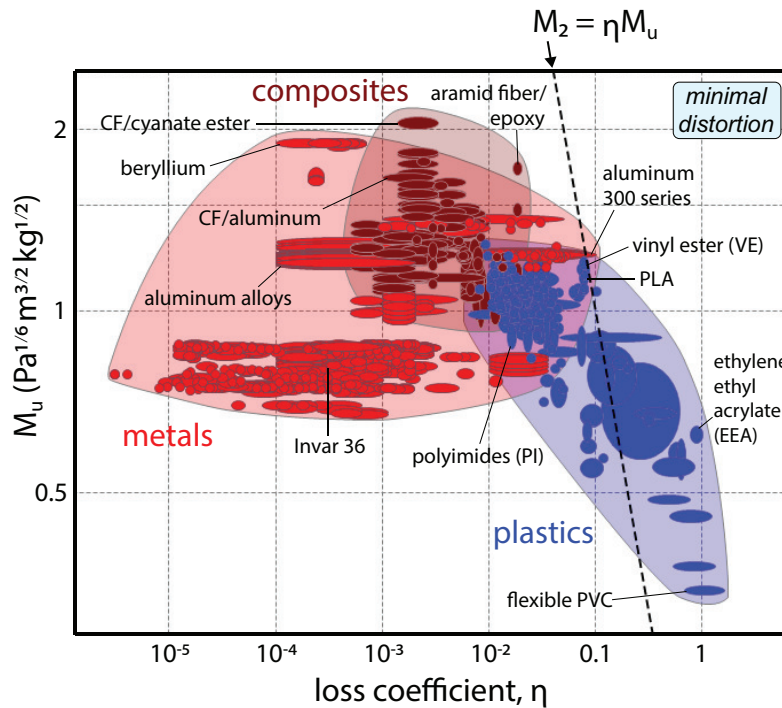


Figure 3-3: Material property diagram for selecting ISM feedstock with minimal distortion from harmonic disturbance loads, plotted for the same materials as Fig. 3-2 [54]. Structures fabricated with materials toward the upper right corner have minimal distortion due to both high damping and high natural frequency. A trade-off between damping and stiffness is observed.

In Fig. 3-3, optimal feedstock materials are located near the upper right corner, as they offer great damping as well as a high natural frequency which minimizes distortion. The chart shows an inverse trend between loss coefficient  $\eta$  and the material index  $M_u$ . Thus, identifying an ISM feedstock material which minimizes distortion from disturbances represents a trade-off between damping and stiffness. Compliant plastics like polyvinyl chloride (PVC) and ethylene ethyl acrylate (EEA) offer great passive damping but lack stiffness, while stiff composites like carbon fiber/cyanate ester and carbon fiber/PEEK create structures with high natural frequency but poor

damping. This contrast is magnified by the thermal stability considerations of the previous subsection: Monolithic plastics have high thermal expansion and temperature-sensitive damping, while high-performance composites are thermally stable. Given these trends, maximizing the material index for resistance to disturbances suggests selecting feedstock materials which have relatively high values of both  $\eta$  and  $M_u$ , such as the thermoplastic polylactic acid (PLA), the thermoset vinyl ester (VE), or 300-series aluminum alloys. However, if the chief concern is disturbances at low frequencies where damping is not vital, using a composite material like CFRP is an optimal choice.

### 3.2.3 Minimal-Mass Buckling Strength

Lastly consider the objective of selecting ISM feedstock which maximizes buckling strength per unit mass of a space structure. Assuming the structure comprises slender members which support fixed compressive loads without buckling, the mass of each member is minimized if the selected material maximizes the index [51]

$$M_3 = \frac{(\phi_{max}E)^{1/2}}{\rho}. \quad (3.7)$$

Here  $E$  is the Young's modulus,  $\rho$  the density, and  $\phi_{max}$  the maximum achievable shape factor of the cross section, approximated as [51]

$$\phi_{max} \approx 2.3 \left( \frac{E}{\sigma_f} \right)^{1/2}, \quad (3.8)$$

where  $\sigma_f$  is the tensile strength of the material. Note that Eq. 3.8 assumes that each member has a cross section optimized for buckling with matching local and global buckling loads.

Figure 3-4 shows the relevant material property diagram for this index, where Young's modulus is multiplied by the dimensionless shape factor given in Eq. 3.8 and plotted against density for the same three material classes as above. A contour line for  $M_3$  with a slope of 2 is overlaid to guide material selection for this index. Among metals, beryllium and its alloys are optimal ISM feedstock materials for minimal-mass

buckling, due to their high specific stiffness and strength. Among composites, carbon fiber-reinforced thermosets and aluminum–matrix composites offer similar performance. While unfilled plastics are generally less efficient for buckling, thermoplastics like self-reinforced polyphenylene (SRP) and thermosets like polyurethane (PUR) appear to be fair feedstock candidates.

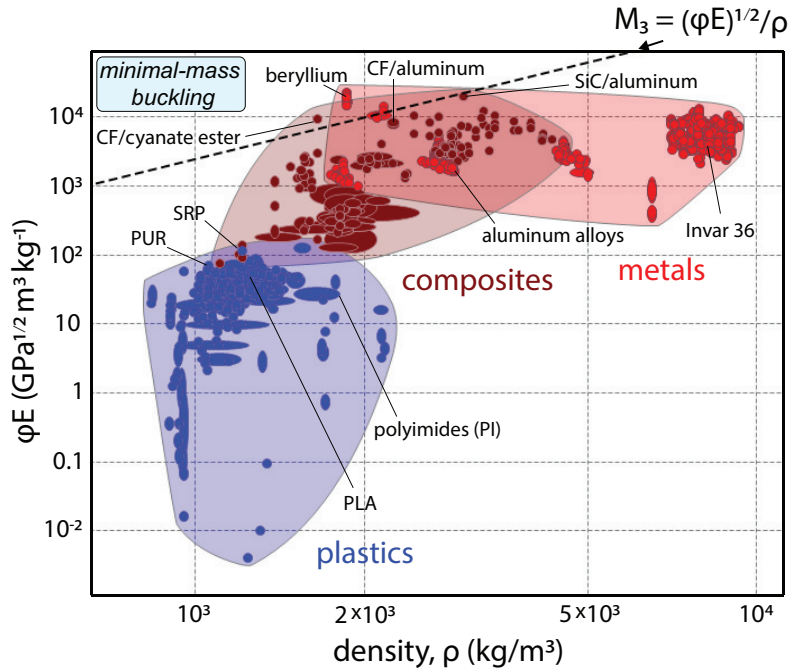


Figure 3-4: Material property diagram for selecting ISM feedstock with minimal-mass buckling strength, plotted for the same materials as Fig. 3-2 [54]. Materials in the upper left corner are optimal for buckling due to their superior combination of Young’s modulus, tensile strength, and density.

### 3.2.4 Summary

Figures 3-2, 3-3 and 3-4 suggest selecting different feedstock materials for in-space manufacturing of a large structure based on its performance objectives: high- $\lambda$  metals and low- $\alpha$  composites for thermal stability; plastics and composites for minimizing surface error from disturbances; and metals and composites for minimal-mass buckling strength. To better understand which materials are optimal for each objective, material index values for promising feedstock candidates from each material class are listed in Table 3.1.

Table 3.1: Candidate ISM feedstock materials for optimizing performance of a large space structure, particularly thermal stability, resistance to disturbance loads, and minimal-mass buckling strength. Materials which maximize the listed material indices are highlighted in bold.

		<b>Thermal Stability</b>	<b>Resistance to Disturbance Loads</b>		<b>Minimal-Mass Buckling</b>
		$M_1 = \lambda/\alpha$	$\eta$	$M_u = (E^{1/3}/\rho)^{1/2}$	$M_3 = (\phi E)^{1/2}/\rho$
		[MW/m]	[ $10^{-3}$ ]	[Pa <sup>1/6</sup> m <sup>3/2</sup> kg <sup>-1/2</sup> ]	[kPa <sup>1/2</sup> m <sup>3</sup> kg <sup>-1</sup> ]
Metals	Al alloys	10.7	2	1.25	20
	<b>Beryllium</b>	20.6	1	1.92	<b>82</b>
	Cu alloys	23.6	1	0.75	9
	Invar	26.9	0.5	0.8	9.1
Composites	<b>CF/Al</b>	<b>1230</b>	3	1.69	41
	<b>CF/cyanate ester</b>	0.163	3.3	<b>2.1</b>	59
	CF/epoxy	5.1	3.3	1.85	34
	CF/PEEK	10.3	3.3	1.85	33
Plastics	PI	0.018	16.4	0.95	3.2
	PLA	0.0013	80	1.11	6.1
	<b>PVC</b>	0.0016	<b>1600</b>	0.35	0.1
	SRP	0.01	9.2	1.3	9.1

The above analysis highlights the following takeaways. First, no one feedstock material is optimal for all performance objectives of a large space structure. While carbon fiber-reinforced aluminum and Invar have excellent thermal stability, they are not optimal for minimal distortion or buckling strength. This suggests that the ideal ISM process is one which can fabricate structural members from all three material classes, thereby leveraging the unique properties of each. Second, Figs. 3-2, 3-3 and 3-4 highlight the tradeoff between material properties of stiffness and damping. While CFRPs have great specific stiffness and result in structures with high natural frequency, a large structure built from such a material would be vulnerable to disturbances due to relatively low passive damping. Hence, selecting and developing ISM feedstocks with damping are important, particularly for large space structures. Lastly, we verify our simple analysis by noting that the material candidates in Table 3.1 are indeed used in space applications today. The hexagonal mirror segments of the James Webb Space Telescope, for instance, are constructed from beryllium due to its high flexural stiffness and stability at cryogenic temperatures [55]. Deployable

booms, routinely used for deploying optics, solar arrays, and solar sails [9, 10, 11], are constructed from CFRPs due to their high specific stiffness. And metal-matrix composites such as SiC/aluminum are used to fabricate precision space optics due to their damping properties and stiffness at elevated temperatures [56]. In this way, the three presented material indices serve as guidelines when selecting feedstock for manufacturing precision space structures. Additionally, this analysis guides future development of ISM feedstocks, such as high-performance composites with larger loss coefficients which are better suited to handle disturbance loads in space.

### 3.3 Process Considerations for ISM

Having identified candidate feedstock materials for ISM in Section 3.2, we now compare several processes, amenable to these different materials, which have shown promise as potential manufacturing methods in space. These include: melt-based additive manufacturing (AM) of metals and plastics, extrusion of fiber-reinforced polymers, and deformation processing of metals. These processing approaches have been pursued to varying levels of maturity [15, 16, 17, 18]. NASA, for instance, has developed a metal AM process which melts wire feedstock onto a substrate via an electron beam [15]. This process has been demonstrated via groundtesting with Al-, Ti-, Ni-, and Fe-based alloys and in microgravity with an Al alloy, at a build rate of 4.5 kg/h and a nominal power draw of 10 kW. Another example of melt-based AM is the process reported by Redwire Space, which uses fused-deposition modeling to fabricate beams from carbon fiber-reinforced thermoplastic polymers [16]. This process will soon be demonstrated in space with the fabrication of two 10-m-long beams, as part of the NASA OSAM-2 mission [34]. Additionally, Tethers Unlimited has developed an extrusion-based process which fabricates trusses from comingled yarn of carbon fiber and PEEK. During a ground demonstration in 2018, this process fabricated a 10-m-long triangular boom at a build rate of 0.1 kg/h and nominal power draw of 100 W [17]. Finally, Kleos Space has reported a pultrusion-based process to construct beams from a thermoset plastic reinforced by continuous carbon fibers [18].

To compare these various ISM processes, we use two performance metrics important for constructing precision space structures, namely the specific energy consumption and the achievable accuracy. Given power constraints, the energy consumption is directly tied to the build rate: For a spacecraft with fixed power output  $P$ , the build rate  $\dot{m}$  of an arbitrary structure is

$$\dot{m} = P/u, \tag{3.9}$$

where  $u$  is the specific energy consumption of the manufacturing process. Hence, ISM processes with lower energy consumption can achieve faster build rates, thereby mitigating issues with stability and thermal management during fabrication on orbit. The second metric for comparison is the process accuracy, which affects the performance of space structures through fabrication tolerances of each member. If an ISM process can maximize accuracy, fabricated structures such as curved reflectors and truss booms can achieve maximal gain and tip accuracy.

### 3.3.1 Energy Required

Given that energy consumption varies greatly with machine parameters and process details, we present here an order-of-magnitude comparison of the minimum energy required for the three ISM processes identified above—melt-based additive manufacturing, extrusion of fiber-reinforced composites, and deformation processing—based on the physics of their primary shaping mechanisms. This discussion follows closely that presented by Ashby in [51] on energy-efficient material processing.

The first process, melt-based processing of metals and plastics, requires melting of feedstock before depositing onto a build platform. In extrusion methods like fused deposition modeling (FDM), melting is achieved through heating of the nozzle, while for directed energy deposition (DED) and powder bed fusion (PBF) methods, it is achieved by a laser or electron beam. Given the common processing step of melting, we estimate the minimum energy per unit mass as the sum of the energy required to reach the melting temperature and the latent heat of melting, expressed as [51]



$$u_{melt} = C_p(T_m - T_0) + L_m, \quad (3.10)$$

where  $C_p$  is the specific heat,  $T_m$  the melting temperature,  $T_0$  the ambient temperature, and  $L_m$  the latent heat of fusion. Assuming the feedstock material is heated in space from a low ambient temperature,  $T_m \gg T_0$ . Furthermore, using the approximate correlation  $L_m \approx 0.4C_pT_m$  and an overall process efficiency of 15% to account for heat losses [51, 57], the required process energy per kilogram is approximately

$$u_M^* \approx 9.3C_pT_m. \quad (3.11)$$

Note that Eq. 3.11 only considers the energy required for melting, as it is the primary shaping mechanism of melt-based AM. We do not include the energy required for secondary processing steps, such as feeding material into the nozzle/build tray or moving the nozzle around the build platform, as these steps generally require a relatively small fraction of the total energy [58].

Similar to melt-based processes, extrusion of fiber-reinforced polymers in space requires heating of feedstock close to its melting point. However, in this case the feedstock is heterogenous, and its specific heat ( $C_{FRP}$ ) is given by the rule of mixtures,

$$C_{FRP} = w_f C_f + (1 - w_f) C_m, \quad (3.12)$$

where  $w_f$  is the weight fraction of the fiber, and  $C_f$ ,  $C_m$  are the specific heats of the fiber and matrix, respectively [59]. Additionally, the processing energy differs between thermoplastic and thermoset matrices. Extrusion of fiber-reinforced thermoplastics relies on heating the matrix beyond its glass transition temperature before it is cooled in the desired shape, while extrusion of fiber-reinforced thermosets relies on a chemical curing reaction which causes permanent polymerization and cross-linking. Hence, we consider each scenario separately. In the case of a thermoplastic matrix, we estimate the energy required to heat the polymer matrix to its melting temperature, with a process efficiency of 15%,

$$u_{FRP-TP}^* \approx 9.3C_{FRP}T_m. \quad (3.13)$$

Here,  $C_{FRP}$  is the specific heat of the composite, and  $T_m$  is the melting temperature of the thermoplastic matrix.

For thermoset matrices, we derive a different expression based on the curing reaction. While the curing is generally exothermic, it requires an activation energy input in the form of heat or pressure. For extrusion of complex shapes, the thermoset matrix is also heated to allow its flow into a shaping tool and proper wetting of the fibers. While these steps do not require complete melting of the matrix, they require, in most cases, heating of the matrix to its glass transition temperature,  $T_g$ . Thus, we estimate the process energy per unit mass as the energy required to heat the composite to the glass transition temperature of the matrix. Using a process efficiency of 15%, we obtain

$$u_{FRP-TS}^* \approx 6.7C_{FRP}T_g, \quad (3.14)$$

Equations 3.13 and 3.14 do not consider secondary shaping steps specific to extrusion of composites, such as pulling of the feedstock through a die to achieve the desired cross section. The mechanical work per unit mass for such a step can be approximated as

$$u_{mechanical} \approx \frac{\mu}{\rho} \dot{\epsilon}, \quad (3.15)$$

where  $\mu$  is the dynamic viscosity of the matrix near its melting temperature,  $\rho$  the density of the composite, and  $\dot{\epsilon}$  the strain rate during deformation. To compare the relative magnitude of this mechanical work with the energy required for heating the feedstock, we consider an exemplar extrusion process which uses a conical die to decrease the cross-sectional area of the heated material. In this case, the strain rate is approximated as [60]

$$\dot{\epsilon} \approx 6v \left( \frac{d_o^2}{d_o^3 - d_f^3} \right) \ln \left( \frac{d_o^2}{d_f^2} \right), \quad (3.16)$$

where  $v$  is the velocity of extrusion and  $d_o$ ,  $d_f$  are the initial and final diameters of the extrudate, respectively. Using representative values of  $d_o = 5$  cm,  $d_f = 2.5$  cm, and  $v = 5$  cm/min, the strain rate is approximately  $\dot{\epsilon} \approx 0.16$  s<sup>-1</sup>. Then, assuming a 15% process efficiency and using a typical melt viscosity of  $\mu = 3 \times 10^4$  Pa · s and a density of  $\rho = 1600$  kg/m<sup>3</sup>, for PEEK reinforced with 60% carbon fibers by volume [61], we obtain the following estimate of the mechanical work per kilogram:

$$u_{mechanical, CF/PEEK} \approx 20.1 \text{ J/kg.}$$

We can compare this value with the energy required for heating the CF/PEEK composite to the melting point of the matrix, obtained from Eq. 3.13, using  $w_f = 0.6$ ,  $C_f = 715$  J/(kg · K),  $C_m = 1340$  J/(kg · K), and  $T_m = 380^\circ\text{C}$ :

$$u_{heating, CF/PEEK} \approx 3.4 \text{ MJ/kg.}$$

The energy required for heating the CF/PEEK composite is thus orders of magnitudes larger than the mechanical work during extrusion. This result also holds for a composite with a thermoset matrix. The above calculation supports our assumption that the majority of energy required for extrusion of fiber-reinforced plastics goes into heating the feedstock, which can be approximated with Eqs. 3.13 and 3.14.

The third ISM processing technique, deformation processing, does not rely on heating of feedstock but instead on plastic deformation to achieve the desired shape. To estimate the energy required for this process, we assume an average flow stress of  $(\sigma_y + \sigma_{uts})/2$  and a strain of order 1. Dividing the resulting strain energy by the density of the material, and using an efficiency of 15%, the energy required to deform a material per unit mass is given by [51]

$$u_D^* \approx 3 \frac{\sigma_y + \sigma_{uts}}{\rho}. \quad (3.17)$$

By only considering the mechanical work from plastic deformation, Eq. 3.17 does not consider the energy for any secondary processing steps, such as feeding or straightening the material.

Using the expressions developed above, Fig. 3-5 compares the energy requirements for melt-based processing, extrusion of fiber-reinforced plastics, and deformation processing for a range of possible ISM feedstock materials. The energies required for melt-based and deformation processing, given by Eqs. 3.11 and 3.17, are plotted for unfilled plastics and ferrous/nonferrous metals. The energies required for extrusion of fiber-reinforced plastics, given by Eqs. 3.13 and 3.14, are plotted for both thermoplastic and thermoset matrices reinforced with 50% carbon fibers by weight.

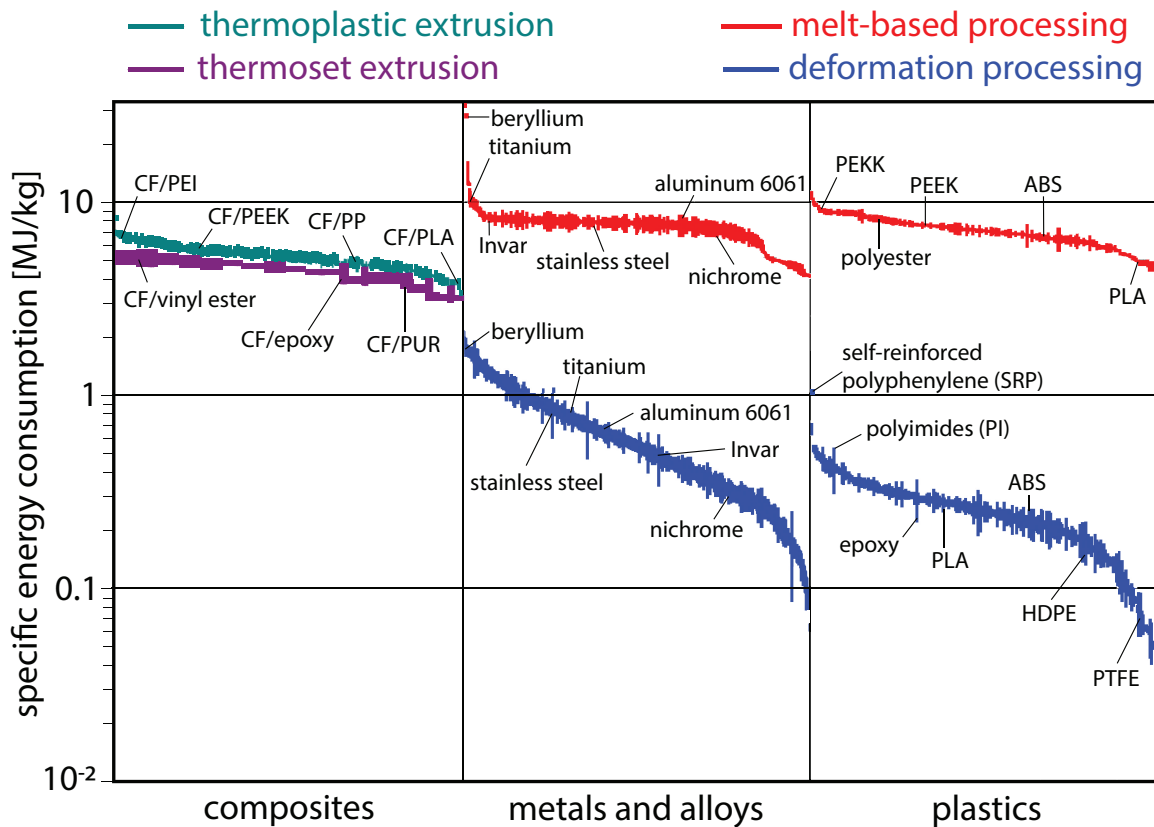


Figure 3-5: A comparison of specific energy consumption for three ISM processing methods: melt-based processing, extrusion of carbon fiber-reinforced thermoplastics/thermosets (with 50% fiber weight fraction), and deformation processing [54]. Each process is represented by a different color, and its specific energy consumption is plotted for relevant feedstock materials, including composites, metals, and plastics. For many materials, the energy consumption of deformation processing is the lowest.

Figure 3-5 shows that, out of the three processes under consideration, melt-based processes require the greatest energy per unit mass, around 8 MJ/kg for most metals and between 5 and 8 MJ/kg for most plastics. Extrusion of carbon fiber-reinforced thermoplastics and thermosets requires less energy, between 3 and 6 MJ/kg, due to the lower specific heat of the composite feedstock and lower heating requirements. Comparatively, deformation processing of metals and plastics requires the least specific energy, between 0.1-2 MJ/kg for metals and 0.05-1 MJ/kg for plastics, which is expended only on plastic deformation. This comparison of approximate energy consumption is directly tied to the maximum build rates of the ISM processes, given by Eq. 3.9. Using the specific energies of Fig. 3-5 and assuming a medium-sized spacecraft with 1 kW power output (i.e., from commercially available solar panels), we find that an ISM process which melts metals or plastics can achieve build rates up to 0.72 kg/h; one which extrudes fiber-reinforced plastics can achieve up to 1.2 kg/h; and one which deforms metals or plastics can achieve up to 36 kg/h. This comparison highlights the relatively low energy requirements of deformation processing compared to other processes which rely on material heating. While the assumed efficiencies of 15% may differ in actual processes, it suggests that if limited by energy consumption, the fastest ISM process relies on deformation processing for shaping feedstock.

While the above analysis is approximate, the calculated process energies of Fig. 3-5 compare favorably with the energy consumption of prototype ISM systems which have been ground-tested. The metal AM system developed by NASA [15], for instance, has fabricated aluminum parts at a build rate of 4.5 kg/h and power draw of 10 kW, yielding a specific energy of 7.9 MJ/kg, a value which matches the energy for melt-based processing in Fig. 3-5. Similarly, the extrusion-based process reported by Tethers Unlimited [17] has constructed trusses from CF/PEEK at a build rate of 0.1 kg/h and power draw of 100 W, placing it at 3.6 MJ/kg, a value which matches the calculated energy range for extrusion of thermoplastics. Lastly, the exemplar deformation process of Bend-Forming (as described in this thesis) can achieve a build rate of a 0.27 kg/h and power draw of 25 W, placing it at 0.33 MJ/kg, which too matches the calculated energy range in Fig. 3-5.

The above comparison motivates deformation processing as a relatively low-energy and fast manufacturing method, but it does not consider material compatibility with the process. One such issue is the tendency of brittle feedstock to fracture during forming, which prevents the use of metals like beryllium or composites like CF/PEEK and SiC/aluminum, which have low strain to failure (around 1%). Ductile metals and polymers, such as steels, aluminum alloys, and polyesters, are more suitable to plastic deformation as they can achieve greater than 10% strain to failure. Furthermore, hybrid feedstock materials in which ductile and brittle constituents are selectively patterned to achieve functionally graded ductility may be amenable to processes with localized plastic deformation.

### **3.3.2 Accuracy**

A second key performance metric for an ISM process is accuracy, which is of critical importance for fabrication of structures such as curved reflectors for space antennas and telescopes, whose performance requires minimal surface error [49]. While the accuracy of different manufacturing processes can be difficult to compare as it depends on the tolerances of individual steps and the geometry of the final structure, in this section we highlight factors which limit the accuracy of the three ISM processes under consideration, focusing on factors unique to the space environment. We also suggest strategies to minimize distortion in space, without considering a particular structural geometry. Note that for specific space structures such as a truss-supported reflector, frameworks exist for predicting surface distortion from fabrication errors like member length deviations [62].

For terrestrial structures fabricated with AM, key factors which limit the dimensional accuracy include layer heights, residual thermal stresses, and positional tolerances of the nozzle and laser/electron beam [63, 64]. In the space environment, additional considerations are necessary. For instance, the lack of convective cooling and the presence of solar heating may magnify thermal stresses during fabrication and cause degradation of mechanical properties. While in terrestrial manufacturing, the volumetric shrinkage during solidification may be mitigated by stress relief an-

nealing of the part and build plate, it is unclear how to accomplish something similar in space. Furthermore, microgravity will affect the adhesion of feedstock to previously built layers by eliminating body forces and increasing the dominance of surface tension-driven capillary forces. Indeed, aluminum prototypes built in microgravity by the metal AM system developed by NASA have shown uneven layer heights due to such adhesion issues [65]. The experiments also showed issues like balling of molten material at the end of the wire feedstock, which inhibited metal transfer and resulted in an uneven build surface. Such challenges, unique to the space environment, need to be considered for an ISM process which relies on melt-based AM.

For extrusion of fiber-reinforced plastics under gravity, inaccuracies can result from non-uniformity of heating, viscous flow under gravitational body forces, and positional tolerances of the nozzle and die [66, 67]. In space, microgravity might alleviate some challenges, such as distortion of the extrudate during curing [68]. However, achieving uniform heating in space may be difficult given varying solar heat fluxes and thermal radiation. For thermoset polymer matrices, this thermal environment can give rise to distortion from nonuniform shrinkage during curing, particularly if the structure has not fully cured before exiting the nozzle. To illustrate this challenge, we present a thermomechanical finite element model of a fiber-reinforced thermosetting beam extruded into space.

The model setup is shown in Fig. 3-6: A tube of length  $L = 1$  m, with outer radius  $R = 0.02$  m and wall thickness  $t = 0.001$  m, is extruded with velocity  $v$  into the space environment. The extrusion is simulated with moving temperature and displacement boundary conditions on the outer surface of the tube. Inside the nozzle, the tube is held rigid and at an initial temperature  $T_0$ ; after extrusion, the tube is free to deform, radiates to an ambient temperature of 3 K, and is subject to solar heating of  $1360$  W/m<sup>2</sup> on its top surface. The model, implemented in the COMSOL Multiphysics software [69], accounts for curing kinetics of the thermoset matrix, heat transfer, and solid mechanics, following the analytical model presented in [70] for curing shrinkage of a carbon fiber-reinforced epoxy composite (CYCOM 5320-1). In our model, we assume that the tube is made of the same material, with stacked unidi-

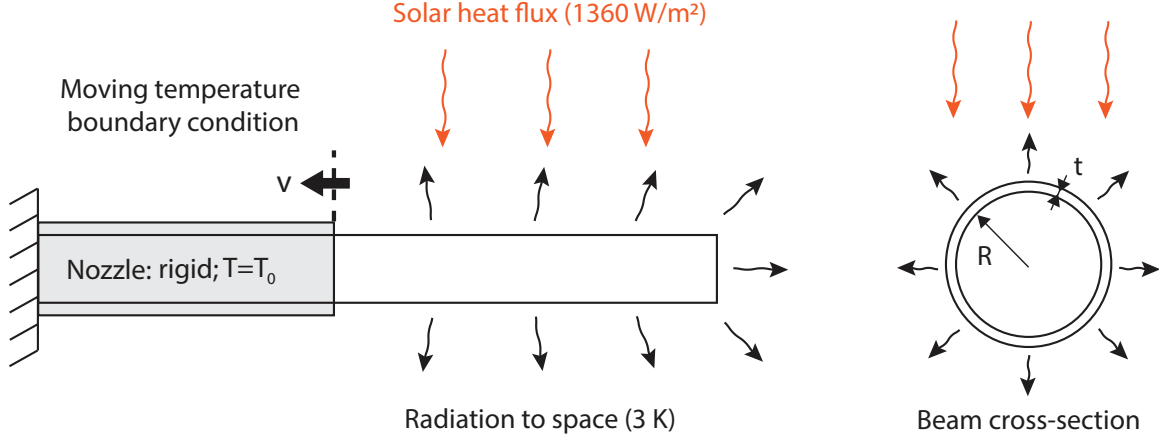


Figure 3-6: Model setup of a thermomechanical simulation of an extruding CF/epoxy tube in space. Extrusion is simulated with a moving temperature boundary on a fixed-length beam. On the one side of the boundary, the tube is rigid and at fixed temperature; on the other side, it is subject to temperature boundary conditions which simulate the space environment.

rectional plies along the extrusion axis. Hence, we use expressions for the orthotropic elastic constants, thermal expansion coefficients, and chemical shrinkage coefficients obtained for a unidirectional ply in [70]. Other material properties used in the model are listed in Table 3.2. Note that while the model presented in [70] was derived for a curing cycle at constant temperature, we use the same model to calculate deformation under varying heat flux and radiative boundary conditions which simulate the space environment.

Table 3.2: Material properties used for the exemplar CF/epoxy composite CYCOM 5320-1. The density ( $\rho$ ), specific heat ( $C_p$ ), and longitudinal, transverse thermal conductivities ( $k_1$ ,  $k_2$ ) are obtained via rule of mixtures. The heat of the reaction ( $H_r$ ) is used as an exothermic heat source during curing. All other orthotropic elastic constants are obtained from [70].

$\rho$	$C_p$	$k_1$	$k_2$	$H_r$
[kg/m <sup>3</sup> ]	[kJ/(kg · K)]	[W/(m · K)]	[W/(m · K)]	[kJ/kg]
1588	0.871	5.88	0.46	500

Each simulation starts with the tube at a uniform temperature of  $T_0$  and a uniform degree of cure ( $\xi$ ) of  $\xi_0 = 0.38$ , which represents the gelation point of the epoxy resin.



Then, the moving temperature boundary condition is implemented at velocity  $v = 5$  mm/s, and the governing differential equations are solved for the temperature, degree of cure, and displacement at each node along the tube. With a simulation time of 800 s, the tube is fully extruded in the first 200 s and subsequently subject to only the temperature boundary conditions of the space environment.

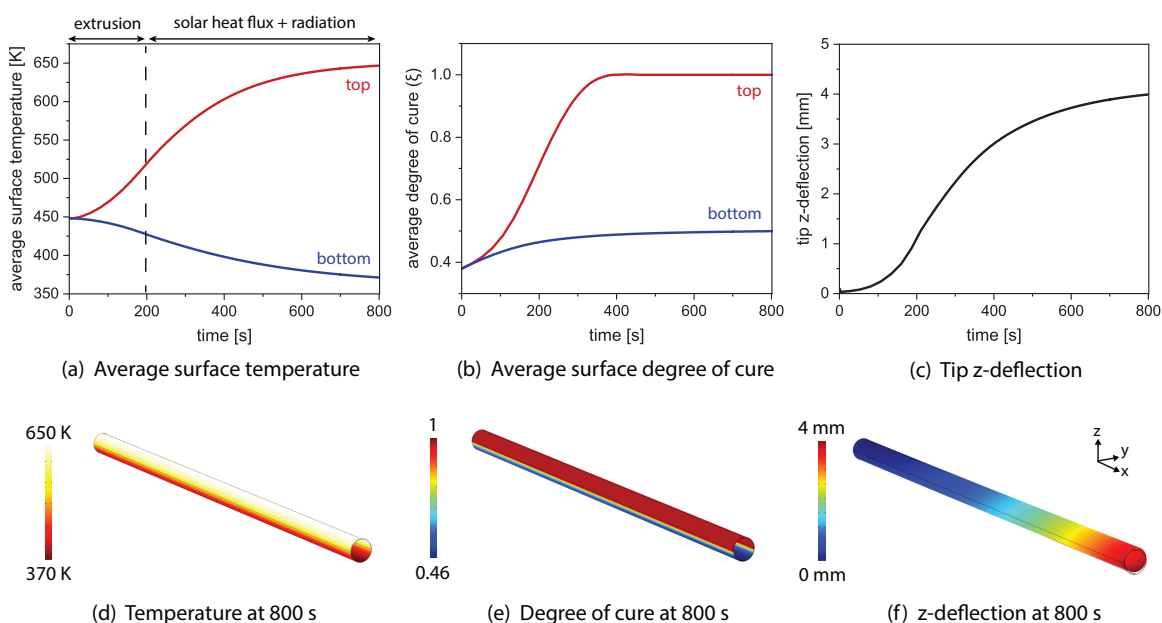


Figure 3-7: Simulation results for extrusion of a partially cured CF/epoxy tube into space, modeled with COMSOL Multiphysics [69]. The extrusion velocity, nozzle temperature, and initial degree of cure are  $v = 5$  mm/s,  $T_0 = 450$  K, and  $\xi_0 = 0.38$ , respectively. The extrusion is modeled for the first 200 s; afterward, the tube is subject to solar heat flux on its top surface and radiation to a low ambient temperature. (a)-(c) plot the average surface temperature, average surface degree of cure, and tip deflection as a function of time, while (d)-(f) show their distributions along the tube at the end of the simulation. Gradients in temperature and degree of cure across the cross section cause deflection at the tip.

Figure 3-7(a)-(c) plots the evolution of the average surface temperature, average surface degree of cure, and tip displacement as functions of time for an initial nozzle temperature of  $T_0 = 450$  K. We see that during and after extrusion, the mean and maximum temperatures of the tube increase due to solar heating, while the minimum temperature decreases due to radiation into space. The resulting temperature and degree of cure distributions are non-uniform across the cross section and give rise to transverse deflection of up to 4 mm via both thermal expansion and chemical

shrinkage. Figure 3-7(d)-(f) plots the temperature, degree of cure, and displacement of the tube at the end of the simulation. Although none of the three dependent variables reach steady-state values after 800 s, the top surface fully cures and reaches a temperature of 650 K, while the bottom surface only cures to  $\xi = 0.46$  and is roughly 280 K cooler. The lower temperature on the bottom surface causes slower curing kinetics, ultimately giving rise to distortion from uneven curing.

To deconvolute the effects of non-uniform cure and temperature gradients across the cross section, Fig. 3-8 shows the average curvature of the tube from thermal expansion and chemical shrinkage separately. For comparison, we also overlay approximate expressions for the two curvatures, given by

$$\kappa_{TE} = \frac{1}{h}[\alpha_1(T_t - T_b)], \quad (3.18)$$

$$\kappa_{CS} = \frac{1}{h}[\beta_1(\xi_t - \xi_b)]. \quad (3.19)$$

Here  $h$  is the thickness of the extruded profile (i.e., tube diameter);  $\alpha_1$ ,  $\beta_1$  are the coefficients of thermal expansion and chemical shrinkage along the extrusion direction (i.e., coincident with fiber direction);  $T_t$ ,  $T_b$  are the average temperatures of the top and bottom surfaces; and  $\xi_t$ ,  $\xi_b$  are the average degrees of cure of the top and bottom surfaces, respectively. In Fig. 3-8, we plot Eqs. 3.18 and 3.19 as functions of time by substituting the average surface temperatures and degrees of cure of the CF/epoxy tube from Fig. 3-7(a)-(b) and the approximate values  $\alpha_1 = -0.96 \times 10^{-6} \text{ K}^{-1}$ ,  $\beta_1 = -25 \times 10^{-6}$  obtained for a unidirectional ply in Ref [70].

Figure 3-8 shows that the majority of the tube curvature is due to the thermal expansion of the CF/epoxy material, almost an order of magnitude greater than that from chemical shrinkage. Nonetheless, for different composite materials with larger chemical shrinkage coefficients, the distortion due to chemical shrinkage may become significant and impact the accuracy. For instance, while the epoxy modeled here has a chemical shrinkage coefficient of  $\beta = 0.022$ , other bisphenol epoxies have been measured to have shrinkage coefficients of  $\beta = 0.095$  [71], a difference which

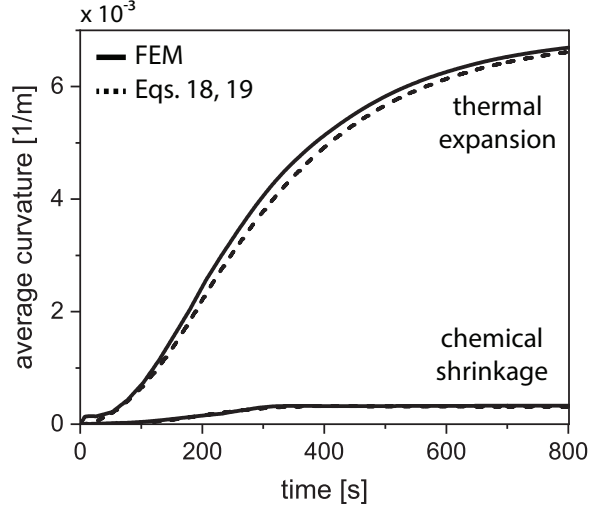


Figure 3-8: Evolution of curvature in an extruding CF/epoxy tube from thermal expansion and chemical shrinkage, separately.

would increase the magnitude of chemical shrinkage strains. In addition, while our model considered a CF/epoxy tube with circular cross section, chemical shrinkage may dominate distortion for laminates with L-cross section [72], as there are additional couplings between in-plane and out-of-plane strains. Hence, Fig. 3-8 suggests that both thermal expansion and chemical shrinkage are important sources of distortion during extrusion in space, and their magnitudes can be approximated well with Eqs. 3.18 and 3.19. From these expressions, we see that the distortion can be minimized by choosing feedstock with high transverse thermal conductivity and low longitudinal thermal expansion/chemical shrinkage coefficients. Given the difference in thermal properties of the carbon fibers and polymer matrix, this suggests selecting feedstock material with high fiber volume fraction and aligning fibers with the extrusion axis.

The evolution of degree of cure after the tube exits the nozzle suggests that distortion can be minimized by tailoring extrusion rate and nozzle temperature such that the degree of cure of the cold surface is close to that of the hot surface. To understand the effect of the nozzle temperature  $T_0$  on the extrusion of the tube, we conduct identical simulations with  $v = 5$  mm/s and  $\xi_0 = 0.38$ , but for the range of nozzle temperatures:  $T_0 = 450$  K; 475 K; 500 K. The resulting changes in average surface temperatures, surface degrees of cure, and curvature of the CF/epoxy tube

are shown in Fig. 3-9. The plots show that increasing  $T_0$  decreases the gradient in  $\xi$  across the cross section of the tube, resulting in smaller curvature after 800 s. These simulations suggest that ISM processes with higher nozzle temperatures may minimize distortion from thermal expansion and uneven curing in space.

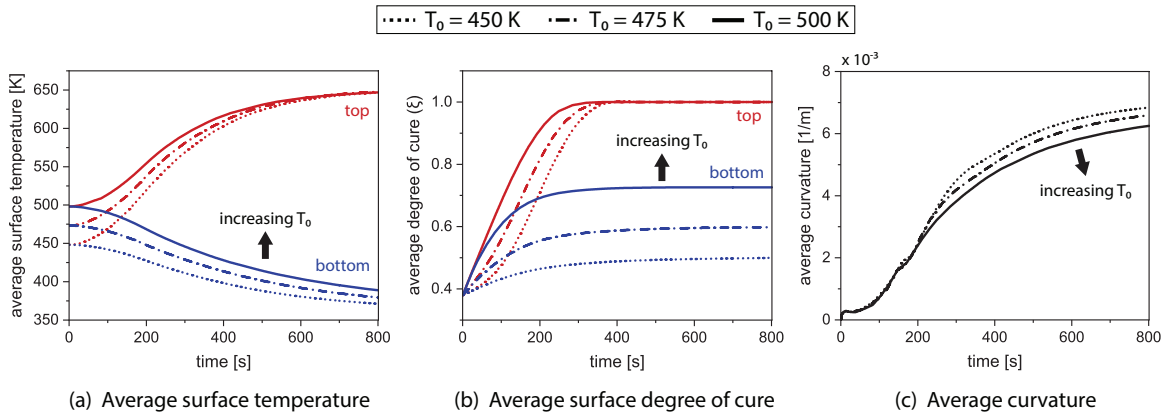


Figure 3-9: Effect of the nozzle temperature  $T_0$  on (a) the average surface temperature, (b) average surface degree of cure, and (c) curvature of an extruding CF/epoxy tube in space. Generally, a higher nozzle temperature decreases curvature after extrusion.

The discussion above highlights challenges with maintaining accuracy in ISM techniques which rely on large thermal excursions, as in melt-based processing of metals, or precisely controlled thermal environments, as in extrusion processing of thermoset materials. Importantly, since deformation processing of certain ductile materials does not require elevated temperatures, this process might be less sensitive to the unique thermal environment of space. The primary source of inaccuracy in deformation processing is elastic springback, which is controlled by the shape, stiffness, and strength of the feedstock as well as the bend radius of the tool [73]. In conventional deformation processing, springback is mitigated through calibration experiments or through process modifications which give more spatially uniform plastic strains (e.g., stretch forming). Because stiffness and strength can vary with temperature, achieving high accuracy via deformation processing in space would require calibrating springback over the thermal cycle expected on orbit.

### 3.4 Material and Process Selection Case Study: ISM of a Tetrahedral Truss

We next synthesize the material and process selection considerations of Sections 3.2 and 3.3 with a case study: in-space manufacturing of a tetrahedral truss supporting a reflector surface, as illustrated in Fig. 3-10. We contrast various materials and ISM processes for constructing this truss structure with three performance metrics, namely the truss mass  $M_t$ , the truss fundamental natural frequency  $f_0$ , and the total build time  $t$ . For applications such as support structure for a space telescope, a small truss mass, high natural frequency, and fast build times are generally desired, to maximize structural efficiency of the truss and minimize thermal effects during fabrication. Here we focus on a specific truss geometry with a depth-to-diameter ratio of 0.2 and derive expressions for  $M_t$ ,  $f_0$ , and  $t$  as a function of diameter for various strut feedstock materials and processing methods. We choose this particular depth-to-diameter ratio as it results in an efficient truss geometry with minimal truss mass fraction. We assume a reflector surface with an areal density of  $\rho_A = 18 \text{ kg/m}^2$ , which corresponds to the beryllium mirrors of the James Webb Space Telescope [74].

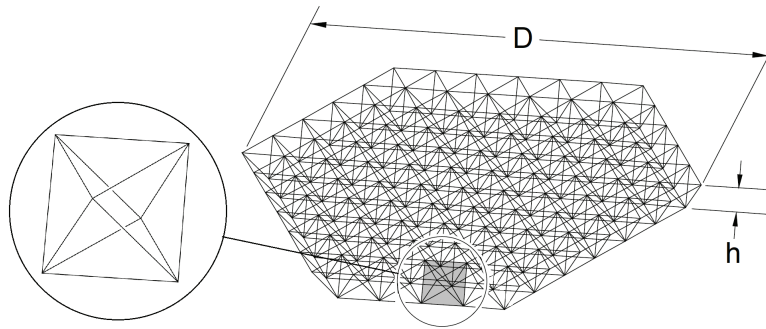


Figure 3-10: Tetrahedral truss geometry, adapted from [4]. This layered truss structure is made of equal-length struts and is formed by repeating a tetrahedral unit cell to create rings. The resulting structure is hexagonal and supports a flat, faceted reflector.

Following the analysis of Lake et al. [4], summarized in Appendix A, we compute the mass and fundamental frequency of a tetrahedral truss with a strut radius of  $r = 5 \text{ mm}$ . Figure 3-11 plots the two variables as a function of truss diameter between

10 m and 100 m, for five candidate feedstock materials selected from Table 3.1. Note that here we assume the strut radius remains constant as the truss diameter increases; other strut radii may be considered for specific applications.

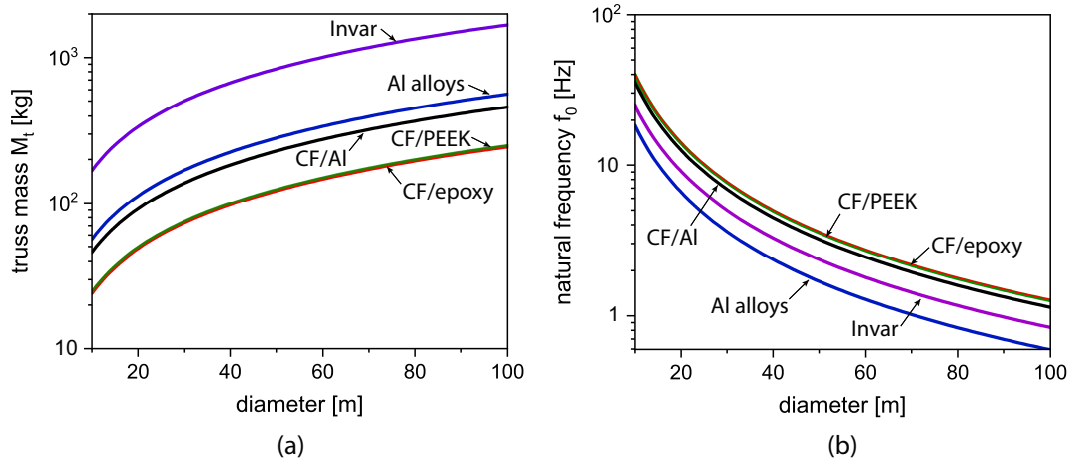


Figure 3-11: (a) Approximate mass of a tetrahedral truss as a function of diameter between 10 m and 100 m, plotted for five candidate ISM feedstock materials. CFRP feedstocks yield the lowest truss mass, followed by aluminum-matrix composites and metals. (b) Truss fundamental frequency as a function of diameter. CFRP feedstocks yield the highest natural frequencies.

We see from Fig. 3-11(a) that using CFRP feedstocks yields tetrahedral trusses with the lowest mass, ranging between 25 kg and 250 kg for the range of diameters considered. Trusses constructed from carbon fiber-reinforced aluminum are second in performance, as their mass stays between 45 kg and 460 kg. Comparatively, heavier feedstock materials like aluminum alloys and Invar yield masses that are approximately an order of magnitude larger, up to almost 1700 kg for the largest structures considered. This material comparison is also reflected in the evolution of fundamental natural frequency in Fig. 3-11(b): composite feedstock materials yield trusses with higher natural frequency than metals. Note that the comparative performance of Invar and aluminum alloys is reversed for the frequency metric, as the higher Young's modulus of Invar compensates for its higher density.

The third performance metric, total build time, relates to the specific energies discussed in Section 3.3 and differs for the type of process used to fabricate the

tetrahedral truss. For melt-based AM and extrusion processes, the total build time  $t_{m,e}$  is directly proportional to the truss mass since all the struts are melted or cured during fabrication. Hence, inverting the build rate given by Eq. 3.9 and multiplying by the truss mass  $M_t$ , the total build time for melt-based and extrusion processes is

$$t_{m,e} = \frac{uM_t}{P}, \quad (3.20)$$

where  $u$  is the specific process energy and  $P$  is the power delivered by the spacecraft. Equation 3.20 assumes that the build rate is only limited by the power available on orbit.

For processes which feed and deform continuous feedstock into truss structures (such the Bend-Forming process described in this thesis), the build time  $t_d$  depends on the machine feed rate  $v_f$ , the total arclength of feedstock  $L_{tot}$ , and the total mass of deformed material  $M_d$ , which is concentrated at the truss nodes. In this case, the build time can be approximated as

$$t_d = \frac{uM_d}{P} + \frac{L_{tot}}{v_f}. \quad (3.21)$$

For the given tetrahedral truss, expressions for  $M_d$  and  $L_{tot}$  are derived in Appendix A. Since the tetrahedral truss has straight members, the amount of deformed material is a small fraction of the truss mass ( $M_d \gg M_t$ ), and most of the building time comes from feeding the material to the machine.

By evaluating Eqs. 3.20 and 3.21, we now compare build times as a function of truss diameter, for various materials and manufacturing processes. We assume a constant strut radius of  $r = 5$  mm and a fixed output of  $P = 1$  kW, which corresponds to the solar panel output of a medium-sized spacecraft. Additionally, for deformation processes, we use a feeding velocity of  $v_f = 1.5$  m/min, a typical feeding velocity for an exemplar CNC wire bending machine [76]. With these parameters, we plot in Fig. 3-12 the total build time as a function of reflector diameter, for the same five candidate materials and their corresponding ISM processes.

Figure 3-12 highlights the large differences in build time between melting/extrusion

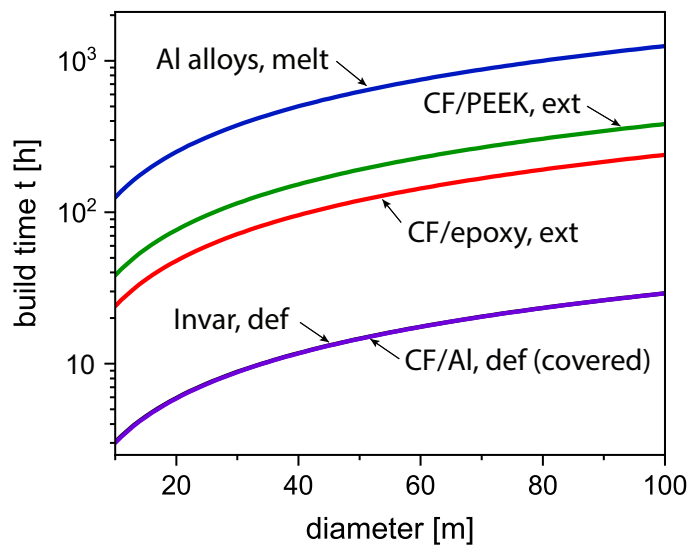


Figure 3-12: Approximate build times of a tetrahedral truss as a function of diameter, for various candidate ISM materials and processes. Deformation processes (denoted by def) generally achieve faster build times than extrusion (ext) or melting (melt) processes due to lower specific energy consumption. Note that while the specific energies required to deform Invar and CF/Al are different, their build time is similar since it is dominated by the time spent feeding material, which we model in Eq. 3.21 as independent of the feedstock material.



and deformation processes. The total build time of the tetrahedral truss with deformation processing of Invar is between several hours and a day, whereas it increases to about 10 days for extrusion of CF/PEEK and up to 50 days for melt-based processing of aluminum alloys. In practice, however, many factors may decrease the build rate for deformation processes. This simple calculation, for instance, does not consider the time required to connect structural components, or the effects of orbital mechanics during fabrication in space.

The above analysis, specific to the tetrahedral truss architecture shown in Fig. 3-10, suggests that deformation processing can enable dramatically faster build times than extrusion and melt-based processes. However, the current materials compatible with deformation processes yield structures which have lower mass efficiency than those made from carbon fiber-reinforced plastics. Given this tradeoff and the high thermal stability required for precision, deformation processing of carbon fiber-reinforced aluminum appears to be a promising approach for constructing trusses in space. Since carbon fibers have low strain to failure, the feedstock and process would need to be carefully designed to avoid failure during forming.

### 3.5 Summary

The analysis presented in this chapter suggests specific materials and approaches for in-space manufacturing as well as key opportunities for further research and development. Material selection for ISM based on three performance metrics important for a large space structure—thermal stability, resistance to disturbances, and minimal-mass buckling strength—highlights several candidate feedstock materials, such as carbon fiber-reinforced aluminum for high thermal stability, carbon fiber-reinforced plastics for minimizing distortion, and beryllium for minimal-mass buckling. However, there is no one material which maximizes all three metrics, motivating the development of hybrid feedstock materials and multi-material ISM to achieve greater structural performance.

The performance of proposed ISM processes (i.e., melt-based processing, extru-

sion processing, and deformation processing) for constructing structures from these feedstock materials was assessed through a comparison of their respective energy consumption and potential sources of inaccuracies, two important metrics for a fast and accurate ISM approach. Approximate expressions for the specific energy consumption of each process showed that deformation processing requires between 5 and 10 times less energy than both melt-based and extrusion processing (i.e.,  $<1$  MJ/kg compared to 5-10 MJ/kg). Therefore, for the same amount of power available on orbit, deformation processing allows for dramatically faster build times. Furthermore, consideration of the unique challenges particular to the space environment illustrates potential issues with achieving accurate structures via processes involving large thermal excursions. For melt-based processes, solar heating and microgravity complicate material deposition, while for extrusion processes, thermomechanical effects such as uneven chemical shrinkage may cause curvature to develop during curing, as demonstrated with a finite element model of an extruding CF/epoxy tube. Since deformation processes do not require heating of feedstock, their accuracy may be less sensitive to temperature variations and instead depend purely on mechanical sources (e.g., elastic springback).

The relative advantages of these different processes and materials were emphasized through a case study, presented in Section 3.4, on in-space manufacturing of a tetrahedral truss supporting a reflector surface. Comparing candidate feedstock materials and manufacturing processes for this application showed that deformation processing can achieve build times as low as a day for a 100 m truss, while extrusion processes require build times close to a week. However, feedstock materials amenable to extrusion processes result in higher structural efficiencies, reducing the total truss mass by a factor of three compared to deformation processes.

These results, considered together, show that deformation processing is a promising method of construction in space due to its low energy consumption and potential for high accuracy. While early concepts for deformation processing [19, 20] have not been implemented on orbit due to challenges with achieving robust joints and geometrically complex structures, with resurgent interest in ISM today and advancements in controls and robotics, deformation processes are worth revisiting. For their successful

application in space, automated processes need to be developed which are amenable to forming multi-material feedstock and to the varying thermal environment of space. In addition, an understanding is needed of the orbital mechanics during fabrication, as large changes in center of mass and moment of inertia during forming may affect the attitude and stability of the spacecraft.

# Chapter 4

## Bend-Forming: A Deformation Process for ISM of Truss Structures

### 4.1 Introduction

The system-level comparison of ISM approaches presented in Chapter 3 motivates deformation processing as a promising method for fabricating large structures on orbit, as it has relatively low energy consumption, offers fast build times, and has low sensitivity to thermal effects. In this chapter, we introduce a novel deformation process, termed Bend-Forming, for fabricating truss structures from a spool of raw feedstock, with application to ISM. As a low-power and low-temperature process, Bend-Forming can quickly fabricate large reticulated structures on-demand to support various mission needs. Given the relatively low loads in the space environment [50], Bend-Forming can fabricate spare parts and support structure for applications such as solar arrays, space telescopes, and antenna apertures. Additionally, although Bend-Forming relies on only a few degrees of freedom, it can create arbitrarily complex geometries, such as reticulated columns, curved gridshells, and tetrahedral trusses.

In this chapter, we describe the Bend-Forming process, including fabrication algorithms, joining methods, and exemplar structures. The chapter is organized into three sections. Section 4.2 presents fabrication algorithms for arbitrary truss geometries, as well as joining techniques for stiff structures. The pseudocode for these algorithms is

summarized in Appendix B and can also be found in [75]. Then Section 4.3 presents exemplar structures fabricated with the process, including reticulated columns, shells, and trusses. Finally Section 4.4 summarizes the chapter and provides context for the application of Bend-Forming in space.

## 4.2 Bend-Forming Process

Bend-Forming uses CNC wire bending to form ductile feedstock into complex truss shapes. The unit process of Bend-Forming is illustrated in Fig. 4-1, which shows a CNC wire bender plastically deforming a straight wire into a pentagon. Depending on the degrees of freedom imparted to the machine, the process can form feedstock in two or three dimensions.

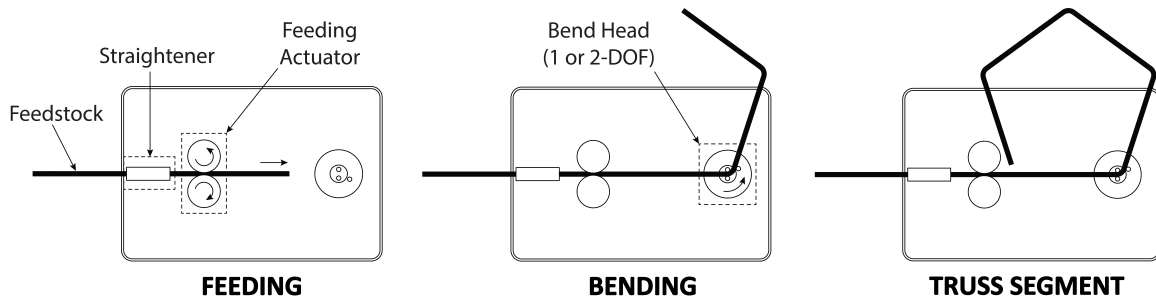


Figure 4-1: The Bend-Forming unit process, illustrated for a pentagon. With a single degree-of-freedom (DOF) bend head, planar trusses can be fabricated; if an additional out-of-plane rotational DOF is added to the bend head, 3D trusses can be fabricated. Note that this illustration is based off the D.I. Wire Pro machine [76].

To fabricate larger trusses, a sequence of straight sections and bends, called a bend path, is prescribed to the machine, such that the straight sections serve as truss members and the bends serve as truss nodes. A robust joining method (either mechanical or solid-state) is then used to hold the feedstock at each node. The final result is a stiff truss made from a continuous strand of wire feedstock. By combining different truss geometries, Bend-Forming can fabricate stiff, lightweight structures from wire feedstock, including Al alloys, Ti alloys, steels, Invar, and other ductile materials.

Below we summarize the process of fabricating arbitrary truss structures with Bend-Forming. The process consists of two steps, summarized in the block diagram in Fig. 4-2. The first step (in yellow) is to find a bend path which traverses the desired truss geometry such that it can be fabricated from continuous feedstock. Classical algorithms from graph theory can be used to find such paths for any 2D or 3D truss geometry, as described in Section 4.2.1. The second step (in orange) is to convert the bend path into instructions for a CNC wire bender, namely a list of feed, bend, and rotate instructions which can be inputted into the machine for fabrication. A geometric algorithm which uses the truss nodal coordinates is implemented in this step to generate the machine instructions, as described in Section 4.2.2. The machine instructions are then used to fabricate the desired truss with a CNC wire bender and with the joining methods described in Section 4.2.3.

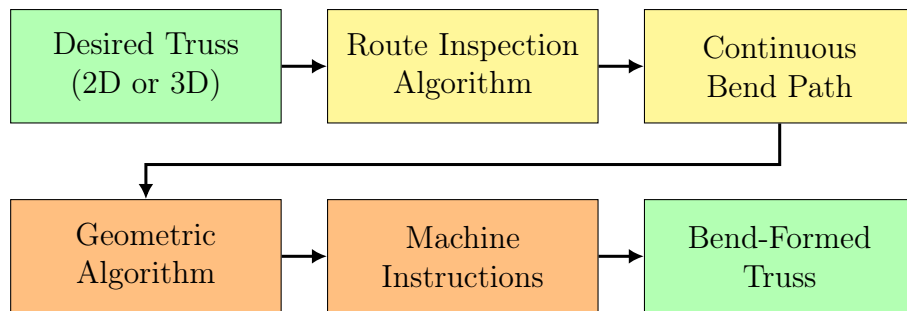


Figure 4-2: Block diagram for fabricating 2D or 3D truss structures with Bend-Forming. The first step (in yellow) is to find a continuous bend path through the desired truss geometry. This is achieved using the route inspection algorithm from graph theory. The second step (in orange) is to convert the bend path into instructions for a CNC wire bending machine. This is achieved via a geometric algorithm which uses the truss nodal coordinates.

### 4.2.1 Finding Bend Paths

To fabricate trusses with Bend-Forming, the first step is to find a bend path which traverses the desired geometry, such that it can be fabricated from continuous feedstock. To minimize mass, we seek bend paths with the shortest length. This problem is a version of the route inspection problem from graph theory (also known as the Chinese postman problem), which seeks the shortest closed path which visits each

edge of a graph [77]. As any truss geometry can be represented as a graph with nodes and edges, the algorithm which solves this problem is directly applicable to finding bend paths for truss structures fabricated with Bend-Forming. Thus, here we describe the route inspection algorithm (as outlined in [77]), but specifically for application to Bend-Forming. Note that this methodology is similar to that presented in [78], where the route inspection algorithm is used to program minimal-time tool paths for 3D printing with fused deposition molding.

### **Route Inspection Algorithm**

The goal of the route inspection algorithm to compute a continuous bend path for an arbitrary truss geometry. To achieve this, the algorithm relies on Euler's theorem, which holds that there exists a continuous bend path which traverses each edge of a truss if and only if there are no more than two nodes with an odd number of connections [77]. Therefore to find continuous bend paths (also called Euler paths), we first check whether the desired geometry satisfies this condition. If not, we add the minimum number of doubled struts to the graph until this condition is satisfied and the graph is made Eulerian. Then, we find a continuous bend path which fully traverses the truss geometry using an algorithm from graph theory called Hierholzer. These two steps of the route inspection algorithm, further described below, are illustrated in Fig. 4-3 for an exemplar 2D and 3D truss.

#### **Make Eulerian:**

The first step in the route inspection algorithm is to add the minimum number of edges to the desired truss geometry until it satisfies Euler's theorem. Physically, these added edges represent doubled struts in the truss which are necessary to fabricate it from a continuous strand of feedstock. To do this, we use the Make Eulerian algorithm (Fig. 4-3). This algorithm works by identifying nodes in the desired truss with odd connectivity (highlighted in red) and connecting them to each other with the shortest paths. These shortest paths are superimposed onto the original truss geometry, resulting in doubled struts at certain locations.

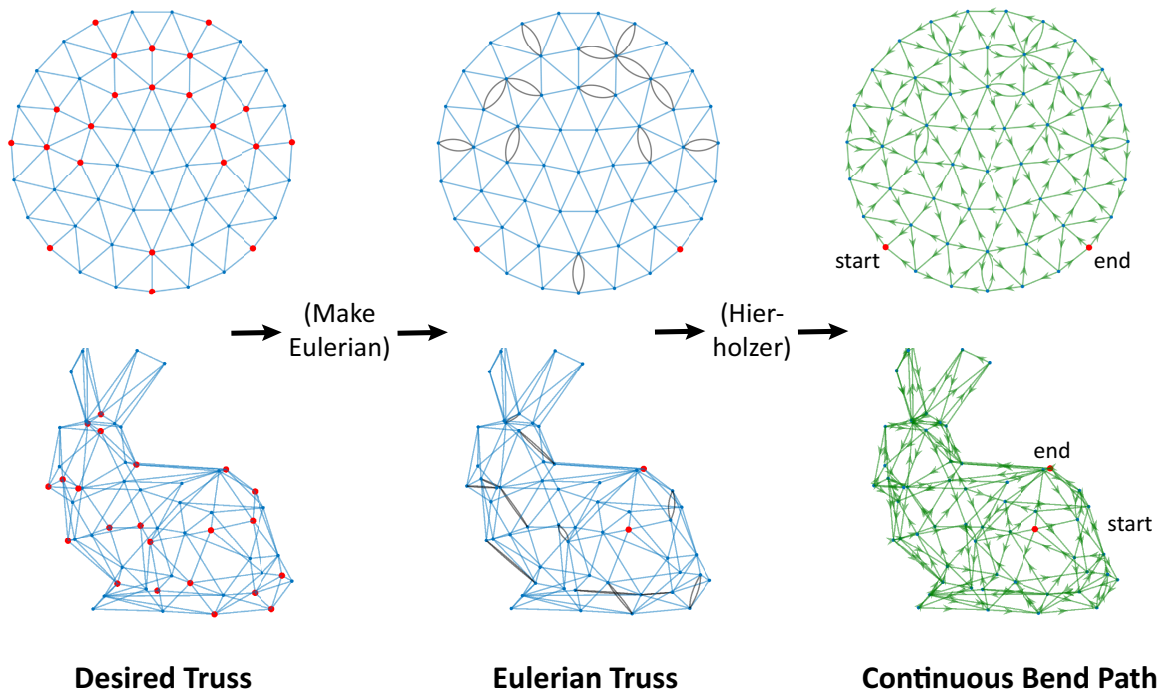


Figure 4-3: The first step of the Bend-Forming process, illustrated for a 2D circular truss and a 3D bunny truss. Here the route inspection algorithm is used to find a continuous bend path for the desired truss. First the Make Eulerian algorithm adds doubled struts to the geometry until only two nodes remain with odd connectivity (highlighted in red). These doubled struts are visualized as curved black edges superimposed on the original geometry. Then the Hierholzer algorithm finds a continuous bend path which traverses each edge of the truss. Note the path found by this algorithm is not unique as many exist for the same geometry. Here one bend path is visualized with green arrows between the start and end nodes. The code for these algorithms can be found in Appendix B and in [75].



The minimum number of paths to add to satisfy Euler’s theorem is given by

$$N_{pathstoadd} = N_{odd}/2 - 1, \quad (4.1)$$

where  $N_{odd}$  is the number of nodes with odd connectivity in the original geometry. To find the paths to add, we loop through every pair of nodes with odd connectivity and calculate the shortest path between them, using breadth-first search [77]. Then, we sort these paths using their total length, resulting in a list of paths between all odd nodes with the minimum number of doubled struts. Finally, we select from this list the  $N_{pathstoadd}$  shortest paths (making sure not to double count odd nodes) and add them to the original truss geometry. The resulting truss has only two nodes with odd connectivity and the minimum number of doubled struts to satisfy Euler’s theorem. Formally, the resulting truss contains a minimum-weight perfect matching between all but two nodes with odd degree, where the length of each edge is used as its weight [79].

The pseudocode for Make Eulerian is summarized in Appendix B, Algorithm 1. It runs with complexity  $O(|V|^3)$ , where  $V$  is the number of nodes in the truss geometry [77]. The input to the function is the nodal coordinates ( $pos$ ) and connectivity matrix ( $g$ ) of the original truss geometry, and the output is an updated connectivity matrix ( $g_{Eulerian}$ ) which contains the minimum number of doubled struts to satisfy Euler’s theorem.

**Hierholzer:**

Once the desired truss has been made Eulerian, we compute a continuous bend path through it, which represents a sequence of struts to be fabricated with the CNC wire bender to achieve the desired geometry. While many such bend paths exist for an arbitrary truss which satisfies Euler’s theorem, here we compute one at random, using the Hierholzer algorithm (Fig. 4-3). This algorithm is efficient at computing bend paths and runs with linear complexity  $O(|E|)$ , where  $E$  is the number of struts [77].

The Hierholzer algorithm works by finding closed loops in the truss geometry and

combining them into one continuous path which traverses each edge. Specifically, for trusses which satisfy Euler’s theorem, the path starts at either a random node in the geometry (if the truss is Eulerian) or at a node with odd degree (if the truss is semi-Eulerian). Next, a neighboring node is selected at random and added to the path. Then the edge connecting the two nodes is deleted, and the process is repeated with the neighboring node. This continues until a node is reached with no neighbors, which results in a closed loop. Then the algorithm backtracks to the last node with neighbors and continues the same process from there, resulting in another closed loop. By repeating this process until all edges have been covered and concatenating the closed loops, the algorithm finds a continuous path which traverses the entire truss geometry.

The pseudocode for Hierholzer is summarized in Appendix B, Algorithm 2. The input to the function is the connectivity matrix of a truss which satisfies Euler’s theorem ( $g_{Eulerian}$ ), and the output is a sequence of nodes which represents a continuous bend path through the truss ( $bendpath$ ). Since the Hierholzer algorithm picks neighboring nodes at random, this bend path is not unique and different paths are obtained each time the algorithm is run.

In this way, by using both the Make Eulerian and Hierholzer algorithms, the route inspection algorithm computes a continuous bend path for any 2D or 3D truss geometry. Due to Euler’s theorem, such bend paths require an even number of connections ( $Z$ ) at a majority of nodes in the truss. Since the necessary condition for rigidity of large pin-jointed trusses also requires even connectivity at each node ( $Z = 6$  in 2D and  $Z = 12$  in 3D) [80], continuous bend paths generated with this process can potentially fabricate rigid trusses with zero mechanisms and zero states of self-stress. Moreover, while the process described above gives only one of many possible bend paths for an arbitrary truss structure, additional algorithms, such as those described in [81, 82], can be implemented to compute bend paths which optimize for specific criteria, such as the stiffness of the intermediate structure during fabrication.

## 4.2.2 Converting to Machine Instructions

After finding a continuous bend path with the route inspection algorithm, the next step in fabricating a truss structure with Bend-Forming is to convert the bend path into instructions for a CNC wire bender. These instructions can be divided into three categories which represent the degrees of freedom (DOFs) of the machine: feeding, bending, and rotating the wire feedstock, as depicted in Fig. 4-4. Here we assume the machine has a 2-DOF bend head which can form the feedstock out-of-plane. Hence to construct the desired truss with a CNC wire bender, we convert the sequence of nodal coordinates which represent the bend path into a list of feed, bend, and rotate instructions which can be used to fabricate the truss. Below, we describe the algorithm used to calculate these machine instructions (Fig. 4-5), which uses solely the geometry of the bend path. While this algorithm is specific to the D.I. Wire Pro machine [76] used to fabricate the prototype structures in this chapter, it is general enough to be applied to any CNC wire bender.

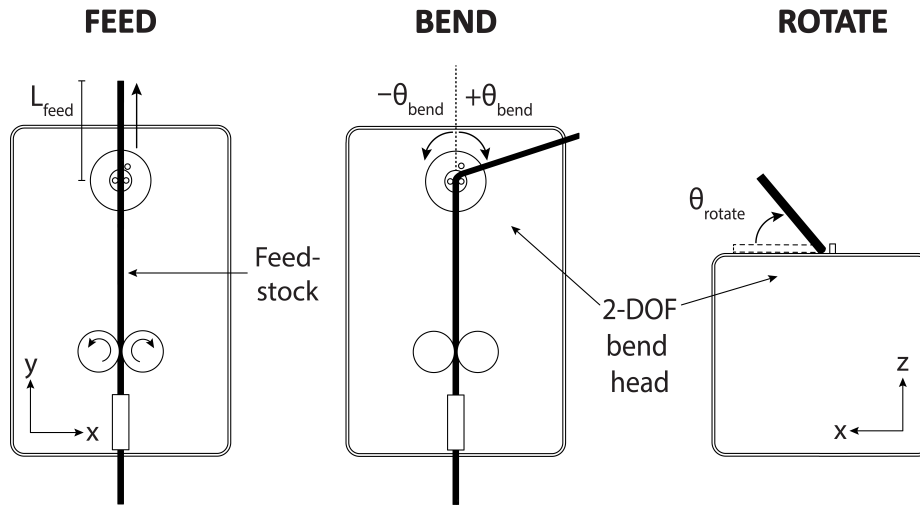


Figure 4-4: Typical degrees of freedom for a CNC wire bender. Assuming a 2-DOF bend head, the machine can feed along the wire axis ( $L_{feed}$ ), bend clockwise or counterclockwise in the  $xy$ -plane ( $\pm\theta_{bend}$ ), and rotate out-of-plane about the feeding axis ( $\theta_{rotate}$ ). To avoid collision with the feedstock and the fabrication plane of the machine, the bend angle and rotation angle are restricted to  $0 \leq \theta_{bend}, \theta_{rotate} \leq 180^\circ$ .

## Geometric Algorithm

The goal of the geometric algorithm (Fig. 4-5) is to compute a list of machine instructions for fabricating the desired truss, using the continuous bend path found by the route inspection algorithm.

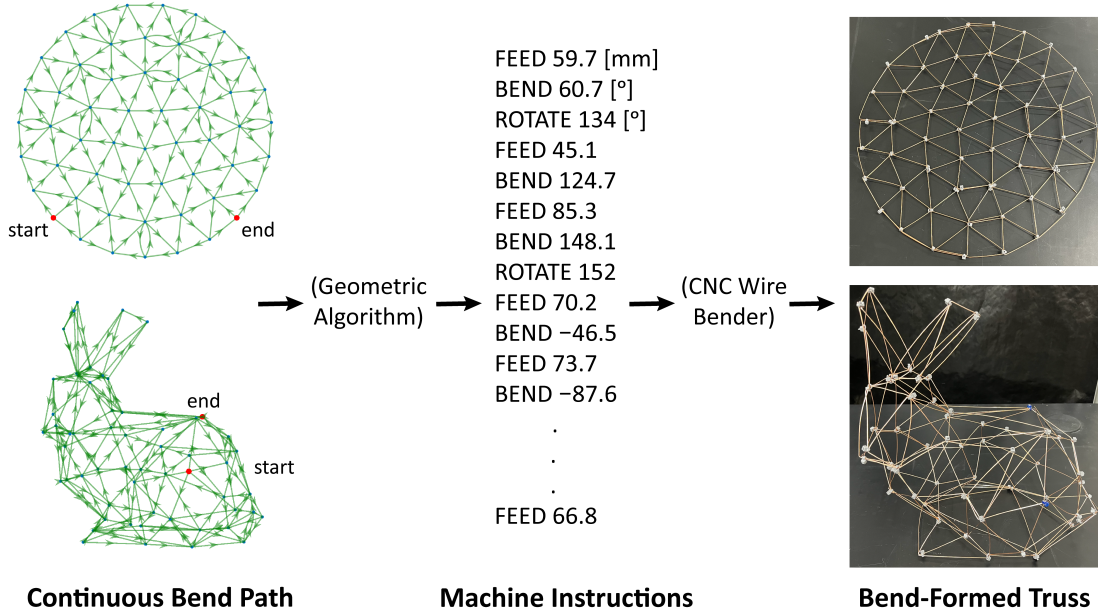


Figure 4-5: The second step of the Bend-Forming process, illustrated for a 2D circular truss and a 3D bunny truss. Here a geometric algorithm is used to convert a continuous bend path into a series of feed, bend, and rotate instructions for a typical CNC wire bender. These instructions are then used to fabricate the desired truss from a spool of raw feedstock. The code for this algorithm can be found in Appendix B and in [75].

The input to the geometric algorithm is a sequence of nodes which represent the bend path and their coordinates. From this we calculate a list of feed, bend, and rotate instructions at each node of the path. An illustration of the algorithm for a simple bend path geometry is shown in Fig. 4-6. Starting with the initial node of the bend path, we determine the feed length  $L_{feed}$  by computing the Euclidean distance between the first two neighboring nodes. Then, we determine the bend angle  $\theta_{bend}$  by computing the angle between the first three nodes in the path, using the definition of the dot product. Next, we keep track of the normal vector to the plane made by the first three nodes of the path ( $\hat{n}_{current}$ ). For subsequent nodes in the path, we

compare this vector to the normal vector made by the next three coordinates ( $\hat{n}_{next}$ ). If the vectors differ, we calculate the angle between them, which corresponds to the complement of the rotation angle  $\theta_{rotate}$ . At the same time, to avoid collision with the fabrication plane of the machine, we ensure that the required rotation between the two normal planes is aligned with the allowed rotation axis of the machine ( $\vec{v}_{rotaxis}$ ). If not, we calculate the rotation angle using the opposite normal vector to the current plane and change the bend angle sign for future bends. In this way, we keep track of both the sign of each bend and the normal vector to every three nodes in the path. This allows the algorithm to calculate the required bend angle  $\theta_{bend}$  and rotation angle  $\theta_{rotate}$  at each step of the bend path, while also handling edge cases like doubled struts for which  $|\theta_{bend}| = 180^\circ$ .

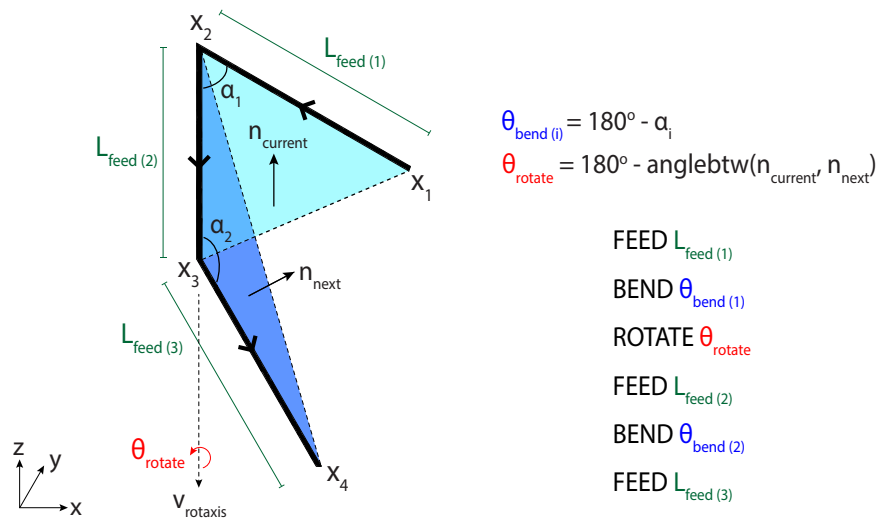


Figure 4-6: Illustration of the geometric algorithm for converting a simple bend path with four nodes ( $x_1-x_4$ ) into a series of machine instructions. The feed length  $L_{feed}$  is computed as the Euclidean distance between subsequent nodes. The bend angle  $\theta_{bend}$  is computed using the angle between every three nodes in the bend path ( $\alpha_i$ ). Finally the rotation angle  $\theta_{rotate}$  is computed using normal vectors to the current and next planes of the path ( $\hat{n}_{current}$  and  $\hat{n}_{next}$ ). Note that the black arrows show the progress of the fabricated truss as the machine instructions are implemented.

The detailed psuedocode for the geometric algorithm is shown in Appendix B, Algorithm 3. The function input is a continuous bend path through the desired

truss (i.e., a nodal sequence *bendpath* and nodal coordinates *pos*), and its output is a text file which contains a series of feed, bend, and rotate instructions (*MachineInstructions*). Note that the additional functions “ $\text{proj}(\vec{a}, \vec{b})$ ” and “ $\text{anglebtw}(\vec{a}, \vec{b})$ ” in the pseudocode correspond to a vector projection of  $\vec{a}$  onto  $\vec{b}$  and the angle between  $\vec{a}$  and  $\vec{b}$ , respectively.

Once a series of machine instructions is generated for the desired truss, it is inputted into a CNC wire bender for fabrication. For a machine such as the D.I. Wire Pro, this corresponds to inputting the instructions into software compatible with the machine. The software converts the feed and bend instructions into appropriate movements of the feeding actuator and bend head, which are calibrated for springback of the feedstock material. The rotate instructions, however, are not automated on machines such as the D.I. Wire Pro with a 1-DOF bend head. Instead, they can be implemented manually after pausing the machine before each wire rotation. On more advanced CNC wire benders with multiple-DOF bend heads (such as the iX-S Wire Former [83]), these rotate instructions can be automated as well. For future application of Bend-Forming in space, all machine instructions would need to be automated and calibrated to the space environment.

### 4.2.3 Joints

The algorithms presented in Sections 4.2.1 and 4.2.2 can be used to fabricate arbitrary 2D or 3D trusses from continuous feedback. The final step in achieving a stiff truss with Bend-Forming is to place rigid joints at the nodes to transfer load between adjacent struts. Various joining methods can be implemented, but for space applications with limited power availability, low-energy joining processes are preferred. Here we describe two such joining methods compatible with Bend-Forming: interference snap-fit joints and soldered joints.

The first joining method relies on snap-fit joints to mechanically stiffen the nodal region. An example of such a joint is shown in Fig. 4-7a. This joint contains two parts: a bottom part with grooves which position the feedstock inside the joint and a top part with pins which snap into holes in the bottom part via an interference

fit. When compressed, the two pieces snap together around the feedstock at each node. The key advantages of this joining method are that it is simple to implement, easy to automate, and requires no heating. However, for complex 3D trusses, unique joint geometries are needed which conform to the strut orientations at each joint. In addition, the joints may lead to anisotropic load transfer between struts, as dictated by the continuous bend path used to fabricate the truss. Since the joints are mated through an interference fit, they may also be susceptible to fracture during application if they are made from brittle materials.

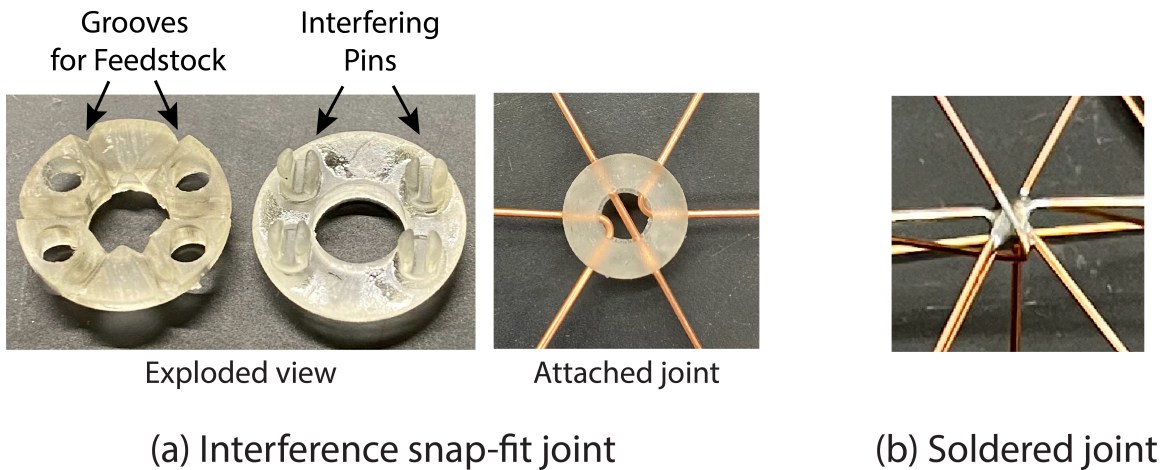


Figure 4-7: Examples of low-power joining methods compatible with Bend-Forming: (a) snap-fit joints which rely on interference and (b) soldered joints. Here the snap-fit joints are made of plastic and 3D printed using a stereolithography (SLA) printer [84].

The second joining method uses brazing or soldering to connect neighboring struts. An example of a soldered joint is shown in Fig. 4-7b. By using a filler metal with a lower melting point than the feedstock material, the energy required for joining adjacent struts remains low with this method. Other key advantages of soldering are that it can create stronger bonds than mechanical joints, is amenable to complex geometries, and is easy to automate. At the same time, accurately positioning the struts around each joint is difficult, and heating the feedstock may lead to thermal distortion and unwanted self-stress in the truss.

Other low-power joining methods which are compatible with Bend-Forming include: resistance spot welding [85, 86, 87], friction stir welding [88, 89], ultrasonic

welding [90, 91, 92], and cold welding [93]. Previous deformation processes proposed for in-space manufacturing have used spot welding to connect thin-gauge metal feedstock [19] and ultrasonic welding to join composite feedstock [20]. Other on-orbit assembly concepts have considered quick-attachment joints which snap together between adjacent struts [24]. Similar joining processes can be developed for Bend-Forming which are low-power, automatic, and amenable to the space environment. In this thesis, we demonstrate Bend-Forming with snap-fit and soldered joints; other joining methods will be the subject of future work.

### 4.3 Exemplar Structures

Using the fabrication and joining processes outlined in Section 4.2, Fig. 4-8 presents exemplar structures fabricated with Bend-Forming, with dimensions on the order of 1 meter. Here the feedstock was 1-mm diameter steel wire and bending was performed with the D.I. Wire Pro machine [76]. Although this machine has a 1-DOF bend head, the required out-of-plane rotations for 3D trusses were implemented manually, simulating a second degree of freedom. Both snap-fit joints and soldered joints were used to fabricate these structures, as shown in the inset images. For each prototype, Table 4.1 lists the total length of feedstock used, the number of bends and joints, and its mass. Further details regarding the geometry, bend path, and fabrication of each structure are presented below.

Table 4.1: Fabrication details for exemplar structures fabricated with Bend-Forming shown in Figure 4-8. Note that the listed mass includes both the wire and the joints.

<b>Prototype</b>	<b>Feedstock Length</b>	<b># Bends</b>	<b># Joints</b>	<b>Mass</b>
Isogrid Column	27.4 m	271	136	218 g
Curved Gridshell	28.5 m	241	90	183 g
Truss Hoop	22.7 m	215	72	114 g
Tetrahedral Truss	5.6 m	79	24	29 g
Bunny	11.9 m	176	57	60 g



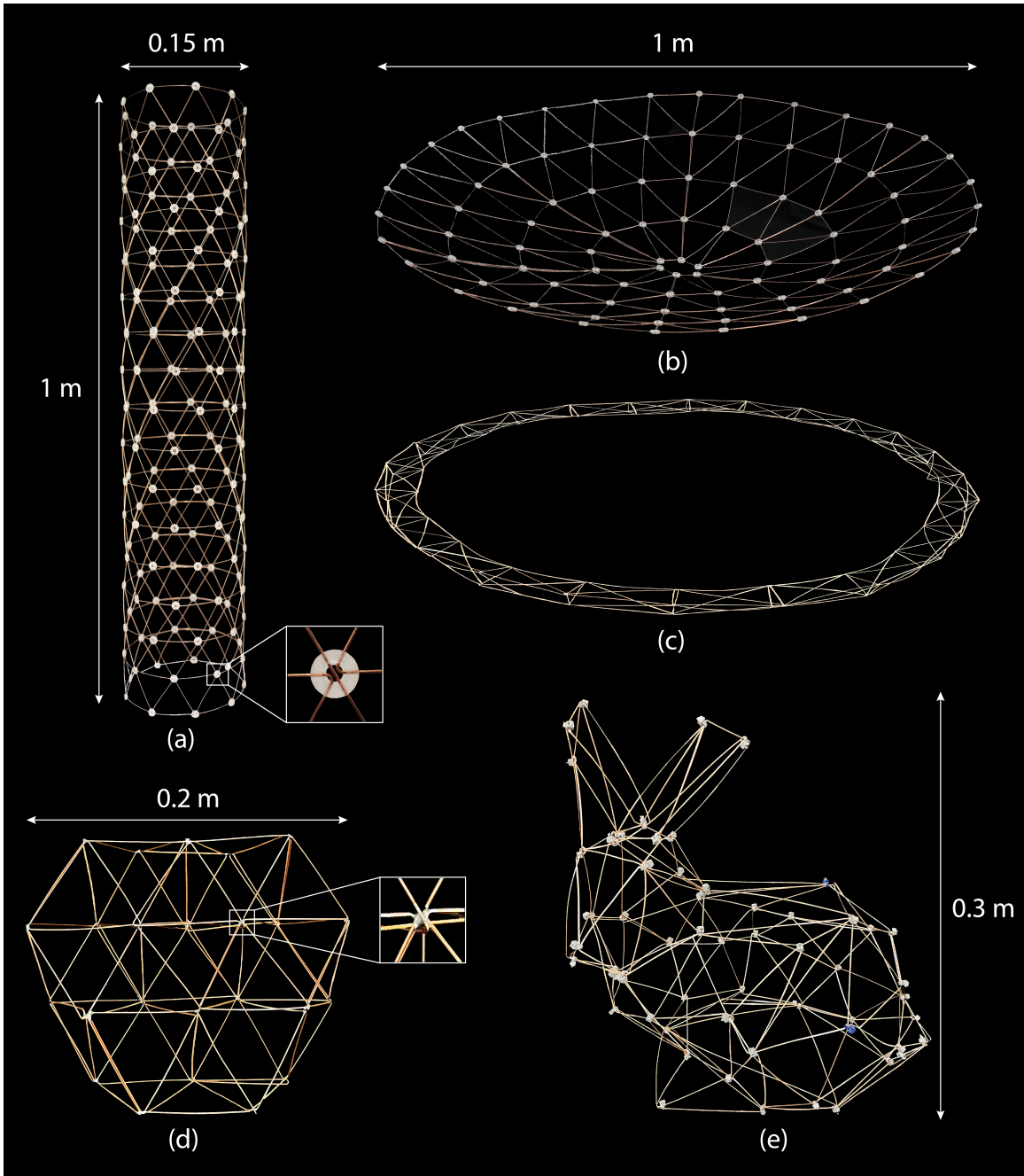


Figure 4-8: Exemplar 3D truss structures fabricated with Bend-Forming: (a) 1-m long isogrid column, (b) 1-m diameter curved gridshell, (c) 1-m diameter truss hoop, (d) 0.2-m wide tetrahedral truss, and (e) 0.3-m tall bunny. Each prototype is made from a single, continuous steel wire using a desktop CNC wire bending machine [76]. The nodes consist of either soldered joints or 3D-printed joints which snap together with interfering pins (see inset images).

### 4.3.1 Isogrid Column

The geometry and bend path of the isogrid column are depicted in Fig. 4-9. The column is parameterized by the diameter  $D$ , height  $H$ , and triangle side length  $L$ .

To fabricate the column with a 1-DOF wire bender such as the D.I. Wire Pro, the geometry is first unrolled about a spiral edge of the cylinder (Fig. 4-9b). Then a continuous bend path is found through the resulting truss and converted to machine instructions using the algorithms presented in Section 4.2. In particular, a zigzag bend path is computed (Fig. 4-9c) which traverses each longeron of the column separately to avoid wire overlaps. The 2D unrolled geometry is fabricated with this bend path, and joints are placed at each node to form a stiff truss. For the prototype shown in Fig. 4-8, plastic snap-fit joints were used to clamp adjacent struts at each node, as described in Section 4.2.3. Finally, the 3D isogrid column is achieved by rolling the 2D truss about the axis of the cylinder until the leftmost and rightmost nodes merge.

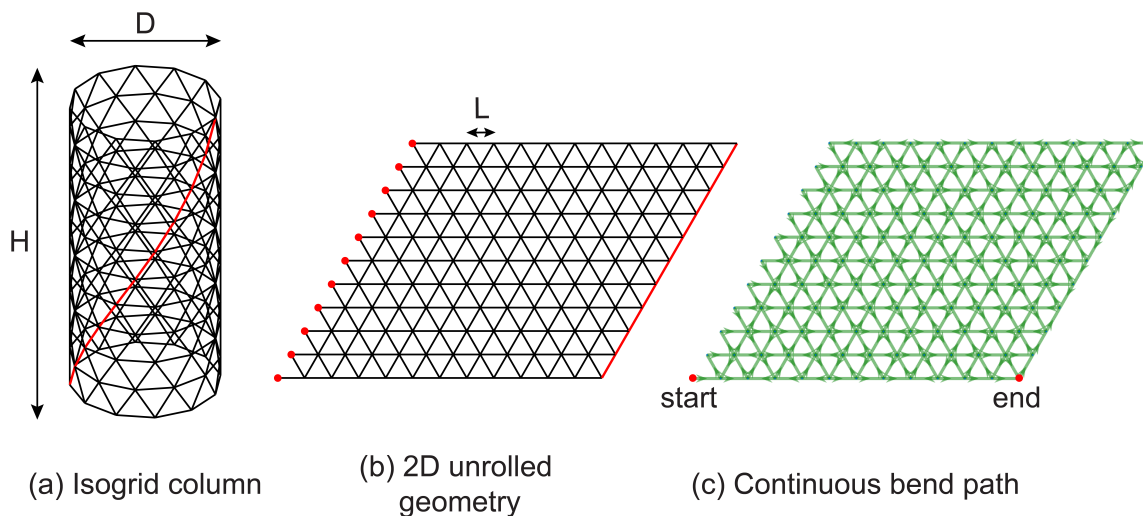


Figure 4-9: Geometry and bend path for an isogrid column fabricated with Bend-Forming. The 3D geometry is first unrolled about a spiral edge (in red). Then a zig-zag bend path is computed (illustrated with green arrows) and converted to machine instructions. Once fabricated, the 2D geometry is rolled about the cylinder axis to obtain an isogrid column.

While this fabrication process uses a 2D bend path and results in isogrid columns with curved struts, the process can be altered to fabricate isogrid columns with straight struts, by using a 3D bend path. In particular, the first step of unrolling

the column can be omitted and a 3D bend path can be directly computed for the original column geometry. This bend path can then be converted to machine instructions for a 2-DOF CNC wire bender, using the same algorithms of Section 4.2.

### 4.3.2 Curved Gridshell

The geometry and bend path of the curved gridshell are depicted in Fig. 4-10. The gridshell is parameterized by the diameter  $D$ , approximate triangle sidelength  $L$ , and focal length-to-diameter ratio  $F/D$ . The triangular mesh on the gridshell is obtained with Delaunay triangulation [94].

To fabricate the gridshell, the 3D geometry is first flattened to a plane. This is achieved with local angular defects, denoted by  $\beta_i$ , which are added between sections of the original geometry at specific radii (Fig. 4-10b). The magnitude of angular defects is related to the gridshell curvature through the approximate relation [95]

$$\beta_i \approx \kappa_i A, \tag{4.2}$$

where  $\kappa_i$  is the Gaussian curvature of the gridshell at radius  $r_i$  and  $A$  is the area of the faceted surface between  $r \in [0, r_i]$ . Thus, Eq. 4.2 is used to calculate the required angular defect at each ring of the geometry ( $i = 1, 2, 3$ ) such that when the angular defects are closed, the resulting gridshell achieves the desired curvature. After computing the 2D geometry with angular defects, a continuous bend path is found and converted to machine instructions for a 1-DOF CNC wire bender, using the algorithms of Section 4.2. The 2D geometry is fabricated with this bend path, and joints are placed at each node. For the prototype in Fig. 4-8, plastic snap-fit joints were used, as described in Section 4.2.3. Finally, the angular defects are closed with additional joints to achieved the desired curvature of the gridshell.

Note that similar to the fabrication of isogrid columns, the above process relies on computing a 2D bend path for the gridshell, which is then fabricated with a 1-DOF CNC wire bender. However, for machines with a 2-DOF bend head, the curved gridshell can be directly fabricated with a 3D bend path using out-of-plane rotations

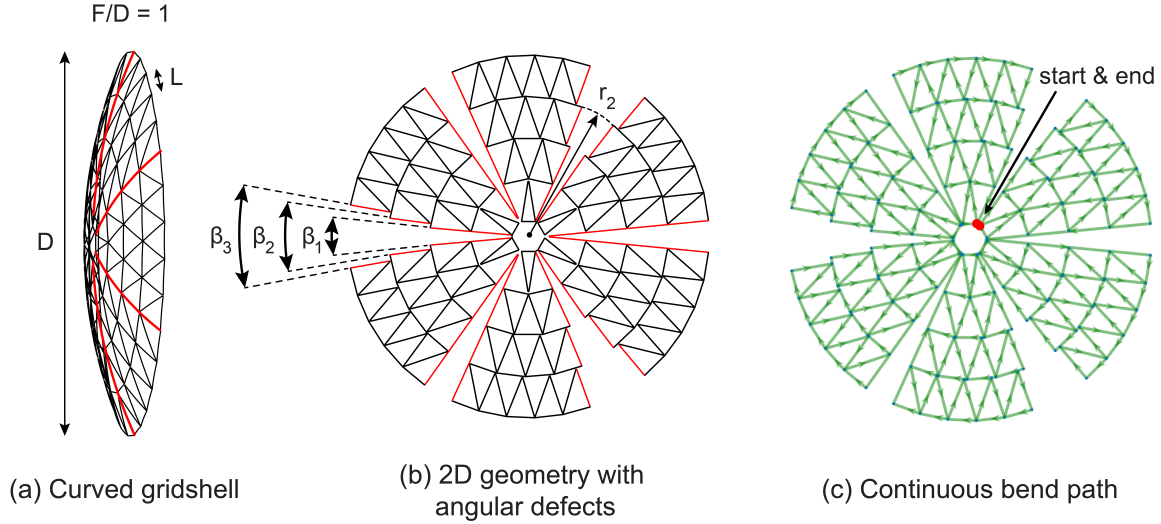


Figure 4-10: Geometry and bend path for a curved gridshell fabricated with Bend-Forming. First the 3D geometry is flattened using angular defects ( $\beta_i$ ). Then a continuous bend path is computed through the 2D geometry and converted to machine instructions for fabrication.

of the feedstock. Such bend paths and the corresponding machine instructions can be computed via the same algorithms presented in Section 4.2.

### 4.3.3 Truss Hoop

The geometry and bend path of the truss hoop are depicted in Fig. 4-11. The hoop is defined with five geometrical parameters: the inner diameter ( $D_{inner}$ ), the cross section diameter ( $D_{CS}$ ), the number of polygonal sides of the cross section ( $N_{CS}$ ), the number of polygonal sides of the hoop ( $N_{hoop}$ ), and the number of bays per side ( $N_{side}$ ). Note that the total number of bays in the hoop is given by  $N_{bay} = N_{hoop} \times N_{side}$ .

To fabricate the truss hoop, a continuous bend path is found through the 3D geometry and converted to machine instructions using the algorithms of Section 4.2. In particular, a bend path is found which completely traverses each bay before moving onto the next (Fig. 4-11b). No additional steps are taken to flatten the geometry. Instead, the machine instructions for the 3D bend path are implemented on the D.I. Wire Pro machine by manually rotating the feedstock out-of-plane, thereby simulating a 2-DOF bend head. Once fabricated, joints are placed at each node to form a stiff

truss. For the prototype in Fig. 4-8, adjacent struts were soldered together at each joint, as described in Section 4.2.3.

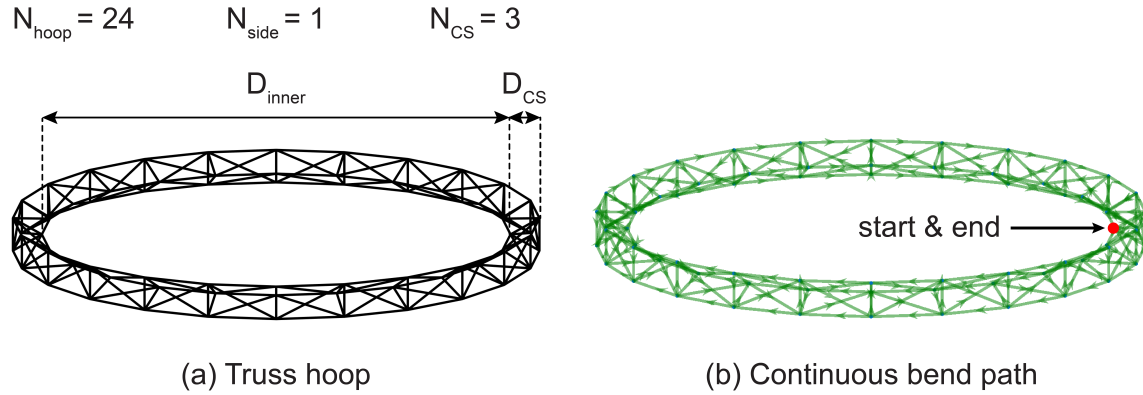


Figure 4-11: Geometry and bend path for a truss hoop fabricated with Bend-Forming. A 3D bend path is computed for the hoop which completely traverses each bay before moving to the next. The continuous bend path is then converted to machine instructions for fabrication.

#### 4.3.4 Tetrahedral Truss

The geometry and bend path of the tetrahedral truss are depicted in Fig. 4-12. The tetrahedral truss is parameterized by the corner-to-corner diameter  $D$  and depth  $H$ . The depth  $H$  is related to the triangle sidelength  $L$  as  $H = L\sqrt{2/3}$ .

To fabricate the tetrahedral truss, a continuous bend path is found through the 3D geometry (Fig. 4-12b) and converted to machine instructions using the algorithms of Section 4.2. Again no additional steps are taken to flatten the geometry. Instead, the machine instructions for the 3D bend path are implemented on the D.I. Wire Pro machine by manually rotating the wire out-of-plane. Finally, soldered joints are placed at each node, resulting in the prototype in Fig. 4-8.

#### 4.3.5 Bunny

The geometry and bend path of the bunny truss are depicted in Fig. 4-13. This geometry is based off the Stanford bunny, a common 3D test model in computer graphics [96]. Here the bunny is parameterized by the height  $H$  and approximate

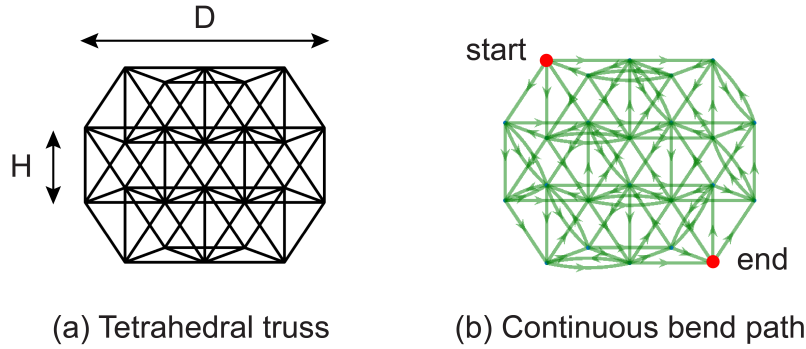


Figure 4-12: Geometry and bend path for a tetrahedral truss fabricated with Bend-Forming. A 3D bend path is computed for the truss and converted to machine instructions for fabrication.

triangle size  $L$ .

To fabricate the bunny, a continuous bend path is found through the 3D geometry (Fig. 4-13b) and converted to machine instructions using the algorithms of Section 4.2. The machine instructions for the 3D bend path are implemented on the D.I. Wire Pro machine with manual out-of-plane rotations, resulting in the prototype shown in Fig. 4-8.

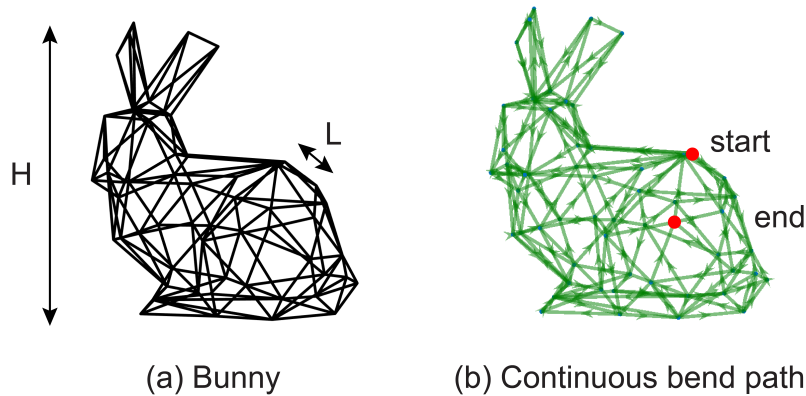


Figure 4-13: Geometry and bend path for a bunny fabricated with Bend-Forming. A 3D bend path is computed for the truss and converted to machine instructions for fabrication.

As illustrated by these five exemplar structures, Bend-Forming can fabricate complex 3D truss geometries via plastic deformation of continuous feedstock. Although the process uses a forming machine with only a few degrees of freedom, by converting the desired truss geometries into simple machine instructions, Bend-Forming can

fabricate arbitrarily complex reticulated shapes.

## 4.4 Summary

Bend-Forming is a low-power method for fabricating truss structures from continuous feedstock. It relies on CNC wire bending and low-power joining methods to form complex truss shapes using plastic deformation. This chapter provided a methodology for fabricating 2D and 3D truss geometries with Bend-Forming. Specifically, we described the process of finding a continuous bend path, converting it to machine instructions for a CNC wire bender, and fabricating the desired truss with stiff joints. This process relies on geometric algorithms which find an Euler path through the desired truss and convert it to machine instructions using the three degrees of freedom of the CNC wire bender: feeding, bending, and rotating. In this way, Bend-Forming can fabricate arbitrarily complex truss geometries from a spool of continuous feedstock, as demonstrated with exemplar isogrid columns, reticulated shells, and tetrahedral trusses.

As a low-power manufacturing method, Bend-Forming can potentially fabricate large structures in space with minimal energy. However, the fabrication process needs to be improved for application on orbit. The first area of improvement is to fully automate the Bend-Forming process. All the prototypes presented in this chapter were fabricated by manually attaching joints to the truss nodes; in space, the joints would need to be attached to the truss simultaneously during forming. This would add stiffness to the truss at each step of fabrication, resulting in a more accurate geometry. Second, the process for computing continuous bend paths as described in this chapter needs to be improved to optimize for fabrication in space. For instance, bend paths should be selected to minimize wire rotation and to avoid collision of the intermediate structure with the machine during fabrication, thereby increasing robustness of the process. Third, for precision space applications, a model needs to be developed for predicting the accuracy of Bend-Formed structures based on the tolerance of individual steps. This model can be used to predict the RMS error

of Bend-Formed trusses and to understand which tolerances result in the largest deviations from the desired geometry. Each of these areas of improvement will be the subject of future work.



# Chapter 5

## Compressive Behavior of Isogrid Columns Fabricated with Bend-Forming

### 5.1 Introduction

The Bend-Forming process described in Chapter 4 can fabricate arbitrary truss structures from continuous feedstock. However, for optimal design of trusses for specific space applications such as support structure for solar arrays and antennas, an understanding is needed of their mechanical behavior. As structures formed via plastic deformation and mechanical joints, Bend-Formed trusses may exhibit constitutive behavior different from pin-jointed trusses studied in the past [97]. Hence understanding their response to various loading scenarios is a necessary step before their implementation in space. Although the loading on orbit is generally low compared to that on the ground, space structures are subject to disturbance loads from solar pressure, slewing, attitude control, and gravity gradients [4]. For Bend-Formed trusses made of thin struts, these loads can lead to buckling, an often unpredictable failure mode for large space structures. To investigate this potential failure mode, in this chapter we study the compressive behavior of isogrid columns fabricated with Bend-Forming,

via both experimental and numerical analyses. We chose this geometry in particular due to its relevance to space applications such as deployable masts [98].

Isogrid columns have been studied previously, both theoretically [50, 99, 100, 101] and experimentally [102]. Generally the accepted approach is to use the continuum properties of a flat lattice to predict the stiffnesses of the column (axial, flexural, and torsional) as well as its buckling load [50]. Other studies have investigated the validity of this approach by comparing it with a discrete model for each strut. These studies found that the continuum analysis overpredicts the buckling load when the characteristic buckling wavelength is on the order of the strut length, or when the axial load in the struts is on the order of their Euler buckling load [99]. In addition, the continuum properties accurately predict the stiffnesses of isogrid columns with a triangular lattice, but they result in an overprediction for other geometries like the Kagome lattice [100]. While the majority of previous work has focused on reticulated columns made of straight struts, one experimental study [102] derived a relationship between initial strut imperfections and the resulting reduction in column stiffnesses, using experiments in compression, bending, and torsion.

Compared to these previous analyses, Bend-Formed isogrid columns are fabricated with a different manufacturing process which complicates their mechanical behavior. As described in Section 4.3.1, the Bend-Formed isogrid columns are manufactured by rolling a flat triangular lattice made of a continuous strand of feedstock. During rolling, each strut of the lattice undergoes 3D deformations which result in both curvature and prestress, affecting the global buckling behavior of the column. To study these effects, here we conduct compressive tests on Bend-Formed columns and characterize their buckling and post-buckling behaviors. We further analyze the experimental responses through finite element simulations which include the initial curvature and prestress of the struts. Through this work, we generate a framework for predicting the strength of Bend-Formed isogrid columns, and identify future research avenues to improve their design and analysis. Note that this chapter is adapted from the published article in [103].

## 5.2 Methods

In this section, we describe the fabrication of Bend-Formed isogrid columns, the experimental setup for compression tests, and the finite element analysis setup.

### 5.2.1 Fabrication of Isogrid Columns

To fabricate isogrid columns with Bend-Forming, we use the process outlined in Section 4.3.1. In particular, we unroll the desired column geometry about a spiral edge, compute a continuous bend path through the resulting triangular lattice, and fabricate the lattice from continuous feedstock with a CNC wire bender. We then add snap-fit joints to stiffen the truss at each node and finally roll the geometry about the cylinder axis to achieve the isogrid column.

Using this process, we fabricated four isogrid columns with varying diameter ( $D$ ), height ( $H$ ), and triangle sidelength ( $L$ ). Fig. 5-1 shows images of the fabricated columns, and Table 5.1 lists the geometric parameters, total feedstock length, and number of bends for each prototype. All columns were fabricated with 1-mm diameter steel wire and the plastic snap-fit joints described in Section 4.2.3. CNC wire bending was implemented with the D.I. Wire Pro machine [76] and the joints were 3D printed from clear resin using the Form 3 SLA printer [84]. Note that for each column, the joints were manually attached to the 2D lattice before rolling it to achieve the final cylindrical geometry. After fabrication, the baseline column was spray-painted white and scanned with a white light 3D scanner (the Creaform GoScan 50 [104]) to obtain a shape measurement of the initial geometry.

### 5.2.2 Experimental Setup

A displacement-controlled compression test was conducted on each Bend-Formed isogrid column, using an Instron 5565 electromechanical load frame. For compatibility with the compression platens of the load frame, flat endcaps which replicate clamped boundary conditions were attached to each end of the column. The endcaps consisted of a circular plate with an outer ring of epoxy to hold the wire, as depicted in

Table 5.1: Geometric parameters of four Bend-Formed isogrid columns tested in compression. Note some values are expressed as ranges due to tolerance stack-up during fabrication.

Column	Diameter [mm]	Height [mm]	Sidelength [mm]	Feedstock Length	# Bends
Baseline	$210 \pm 3$	$562 \pm 2$	82.5	16.5 m	143
Small sidelength	$206 \pm 3$	$569 \pm 2$	65	20.2 m	219
Wide	$259 \pm 3$	$562 \pm 2$	82.5	20.5 m	179
Long	$206 \pm 3$	$850 \pm 2$	82.5	24.75 m	207

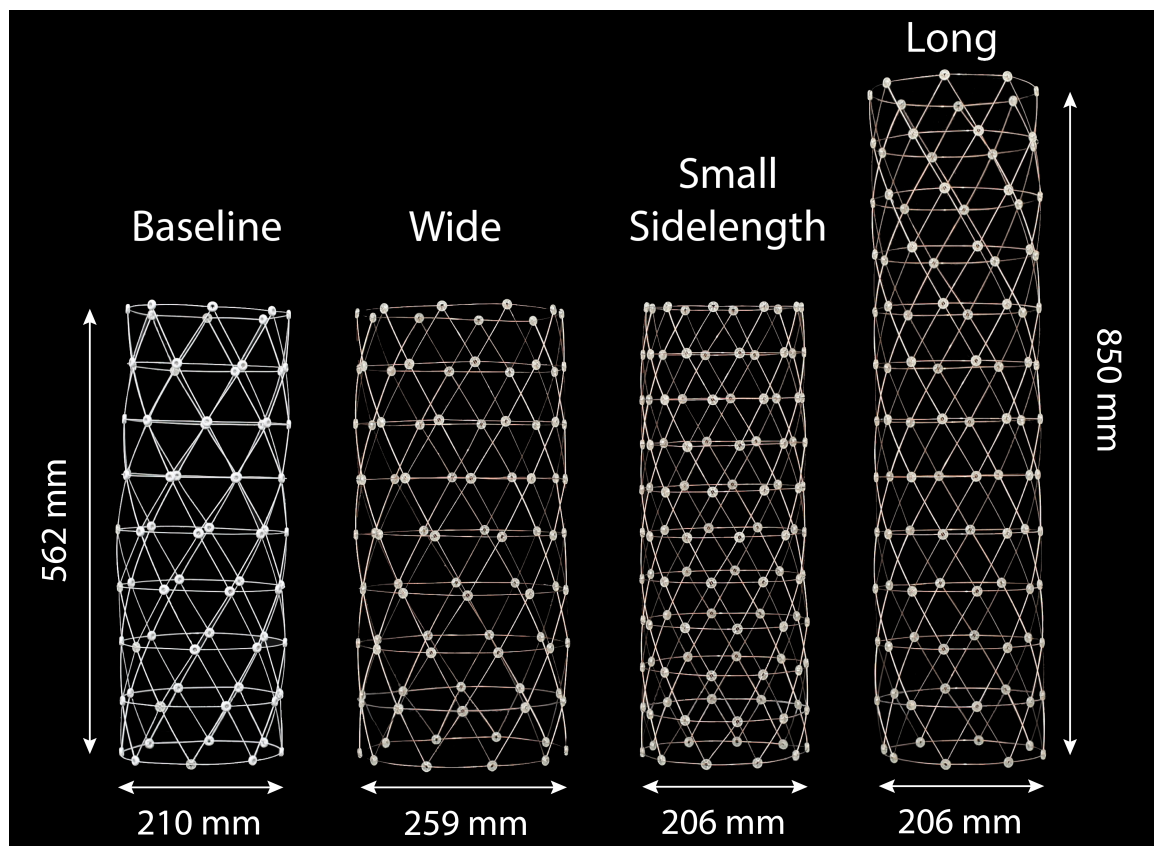
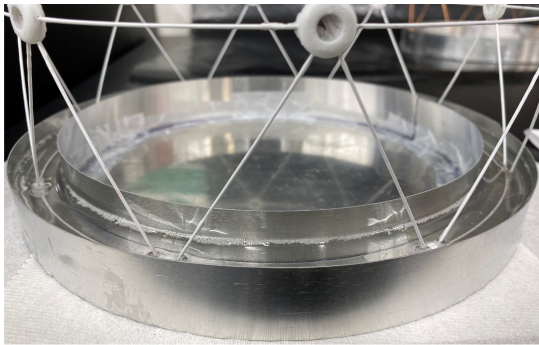
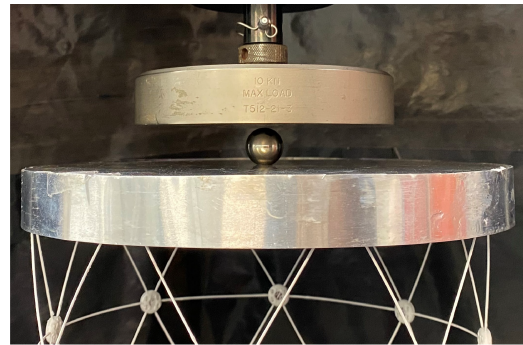


Figure 5-1: Four isogrid columns fabricated with Bend-Forming, using 1-mm diameter steel wire and plastic snap-fit joints. Each column was tested in compression, with only one geometric parameter varied between columns: diameter, height, or triangle sidelength. The baseline column was spray-painted white for shape measurement with a white light 3D scanner.

Fig. 5-2a. To keep the loading axis perpendicular to the endcaps, the columns were vertically lowered into the epoxy-filled endcaps. In addition, to minimize the effects of misalignment between the top and bottom endcaps, a marble was placed between the top compression platen and the top endcap, as shown in Fig. 5-2b. The marble rested in a small hole at the center of the top endcap and permitted rotation of the endcap during the compression test. This resulted in purely vertical load application and minimized the effect of tilt misalignment between the endcaps. During each compression test, a displacement of 10 mm was applied to the top endcap at a rate of 0.01 mm/s, and a video was taken of the column to characterize its deformation.



(a) Epoxy-filled endcap



(b) Load application with marble

Figure 5-2: Boundary conditions for compression of Bend-Formed isogrid columns. (a) Both sides of the column are embedded in epoxy-filled endcaps. (b) Load is applied with a marble to minimize effects of any tilt misalignment.

### 5.2.3 Finite Element Analysis

The columns shown in Fig. 5-1 were modeled using the finite element software Abaqus to investigate their compressive behavior. In particular, we captured the effect of rolling the triangular lattice during fabrication on the buckling and post-buckling behavior of the column. To this end, the 2D unrolled geometry depicted in Fig. 4-9b was imported into Abaqus and meshed using linear beam elements (B31). Each element was 6.35 mm long and assigned a circular cross-section with 0.9 mm diameter, matching the cross section of the wire used to fabricate the prototypes. The elements were assigned isotropic elastic properties of steel wire, with Young's modulus  $E = 200$

GPa and Poisson ratio  $\nu = 0.29$ . To simplify modeling of the joints, each strut was fully connected to adjacent struts at the truss nodes, with kinematic coupling of all six degrees of freedom. The implications of this modeling choice are discussed further in the next sections.

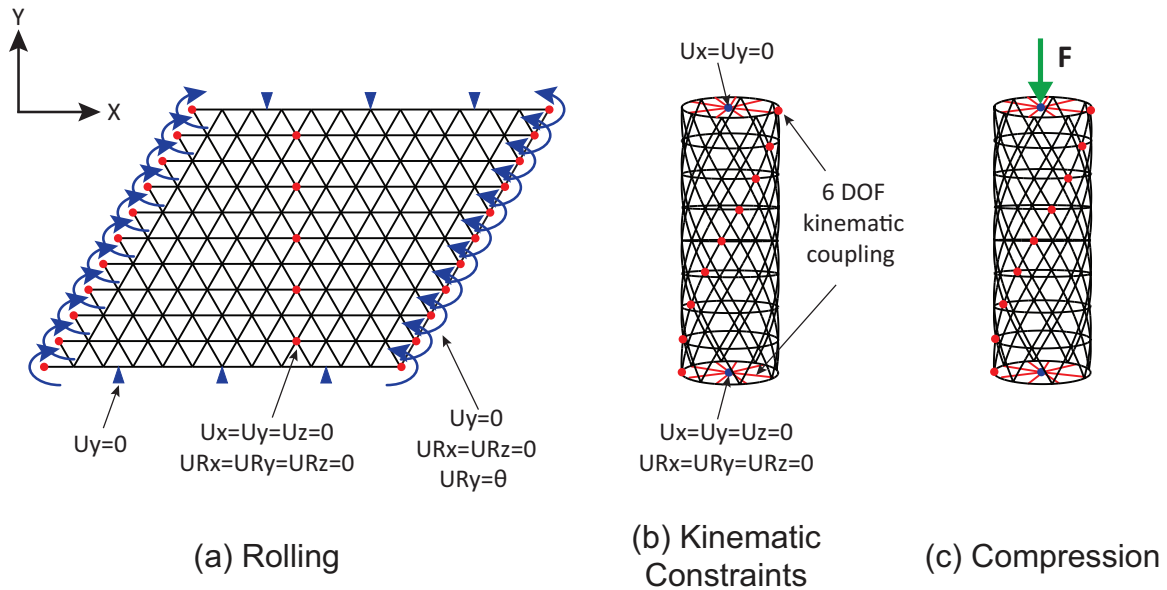


Figure 5-3: Illustration of the finite element analysis for compression of Bend-Formed isogrid columns. (a) Rotational boundary conditions are applied to roll the 2D triangular lattice into a cylinder. (b) Kinematic constraints are applied to merge the leftmost and rightmost nodes and compute the equilibrium state of the column. (c) A compressive force is applied at the top of the column.

The analysis follows multiple steps, as illustrated in Fig. 5-3. In the first step (Fig. 5-3a), the initially flat triangular lattice is rolled into a cylinder via rotational boundary conditions applied to its leftmost and rightmost nodes. During this step, all edges parallel to the  $x$ -axis are constrained from moving vertically, and a series of nodes which form the centerline of the lattice are fully clamped. The simulation is quasi-static, considers nonlinear changes in geometry, and uses the Newton-Raphson solver of Abaqus Standard. As rotations are applied to the boundary nodes, curvature and prestress develop in the struts, and the analysis step is completed when the leftmost and rightmost nodes become coincident.

In the second analysis step (Fig. 5-3b), all degrees of freedom of the leftmost and rightmost nodes are coupled through kinematic constraints to maintain the rolled

shape of the column. Physically, this corresponds to the final attachment of mechanical joints during fabrication of the column to achieve the cylindrical geometry. In our simulation, these kinematic constraints are implemented with a Fortran subroutine which defines multi-point constraints (MPCs) after the rolling step. In addition, the same type of constraints are used to couple the top and bottom boundaries of the column to reference points along the column axis, thereby replicating the attachment of the column to the epoxy-filled endcaps. Once these additional constraints are added, the rotational boundary conditions used in the rolling step are released and the stress and deformation states are recomputed to ensure that the column is in equilibrium.

Finally, in the last analysis step (Fig. 5-3c), a compressive force is applied to the top reference point, which is allowed to rotate similar to the marble in the experiment. A buckling eigenvalue analysis is performed and the full post-buckling response is computed using a Riks solver. The Riks solver computes the load and displacement of the column simultaneously by incrementing the arclength along the static equilibrium path, enabling the resolution of unstable responses. Generally for such thin shell structures, multiple post-buckling responses can compete in what is referred to as “spatial chaos” [105]. To guide the solver towards specific post-buckling paths, geometric perturbations based on the eigenmodes of the column are seeded in the initial geometry. More details about this procedure are given in Section 5.4.

## 5.3 Results

The experimental load-displacement curves for compression of the four Bend-Formed isogrid columns are plotted in Fig. 5-4, along with images of the columns at various points during the test. Table 5.2 lists the measured axial stiffness and maximum load of the Bend-Formed columns. For each column, we observed an initially linear response, followed by nonlinear softening, a local maximum in load, and a region of negative stiffness. Comparing the initially linear responses of the four columns, we see that the columns with smaller side length and larger diameter (Fig. 5-4b, 5-4c) achieved both a higher axial stiffness and maximum load than the baseline column

(Fig. 5-4a). Comparatively, the longer column (Fig. 5-4d) achieved both a lower axial stiffness and maximum load. These trends match with analytical expressions for axial stiffness and buckling load of isogrid columns, as derived in [50] using the effective properties of a planar triangular lattice.

After the maximum load was reached in the experiments, there was a gradual decrease in load-carrying capability of each column as the compressive displacement was increased. This region of negative stiffness corresponded to the formation of localized buckling deformations (i.e., “dimples”) at various locations along the height of the column. For the smaller sidelength and wide columns Fig. (5-4b, 5-4c), asymmetric localized deformations formed on one side of the cylinder, near the center and top bays, respectively. These deformations resulted in a large rotation of the top endcap at a displacement of 8 mm, as well as a sharp drop in load. This sharp drop corresponded to the conversion of strain energy to kinetic energy, an unstable behavior similar to that observed during compression of thin cylindrical shells [106]. In contrast, the baseline column showed the formation of a symmetric localized deformations at a central bay, which grew in amplitude with increasing displacement (Fig. 5-4a). Finally the long column showed the simultaneous formation of two localized deformations near the top and bottom bays (Fig. 5-4d).

Table 5.2: Experimentally measured axial stiffness and maximum compressive load of four Bend-Formed isogrid columns.

Column	$k_{axial}$ [N/mm]	$P_{max}$ [N]
Baseline	68.6	187
Small sidelength	182	324
Wide	98.6	221
Long	47.5	170



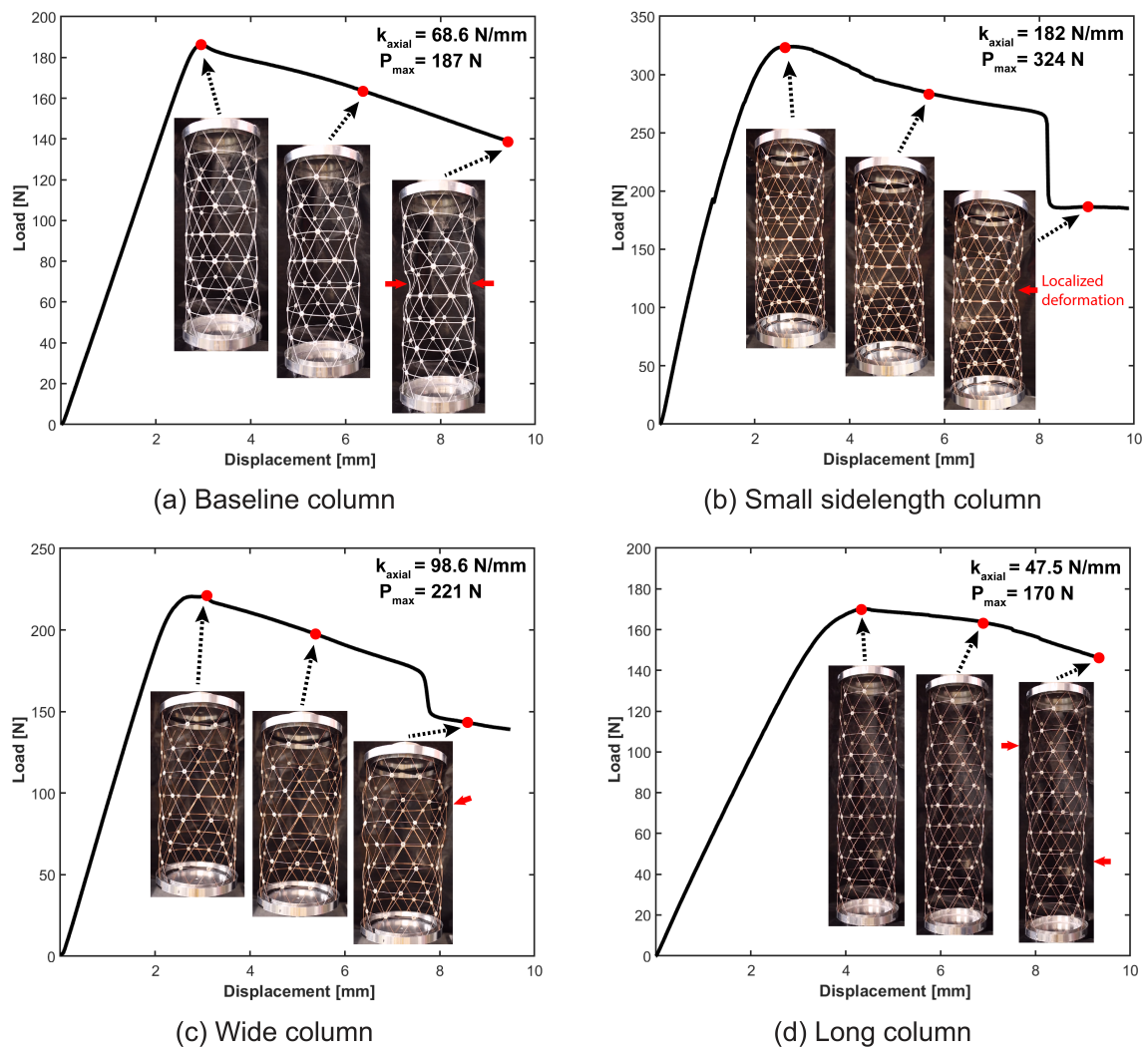


Figure 5-4: Experimental results for compression of four Bend-Formed isogrid columns. The load-displacement curve is plotted for each column with images at three points during the test. The locations of the largest-amplitude deformations are highlighted with red arrows. All four columns display an initially linear response, followed by nonlinear softening, and a gradual decrease of the load which corresponds the formation of localized deformations along the height of the column.

## 5.4 Discussion

### 5.4.1 Initial Geometry

As buckling of thin cylindrical columns is generally sensitive to geometrical imperfections [109], we first assessed the magnitude of imperfections in the experimentally-tested prototypes. Specifically, we compared the geometry of the baseline column predicted by the rolling step of the finite element analysis (Fig. 5-3a) to the physical shape of the fabricated column, obtained as a point cloud via a white light 3D scanner [104]. Fig. 5-5 shows deviations between the predicted and actual column geometries. Here the two column geometries are aligned using circles fitted to the middle plane of the column (i.e., at a height of 281 mm).

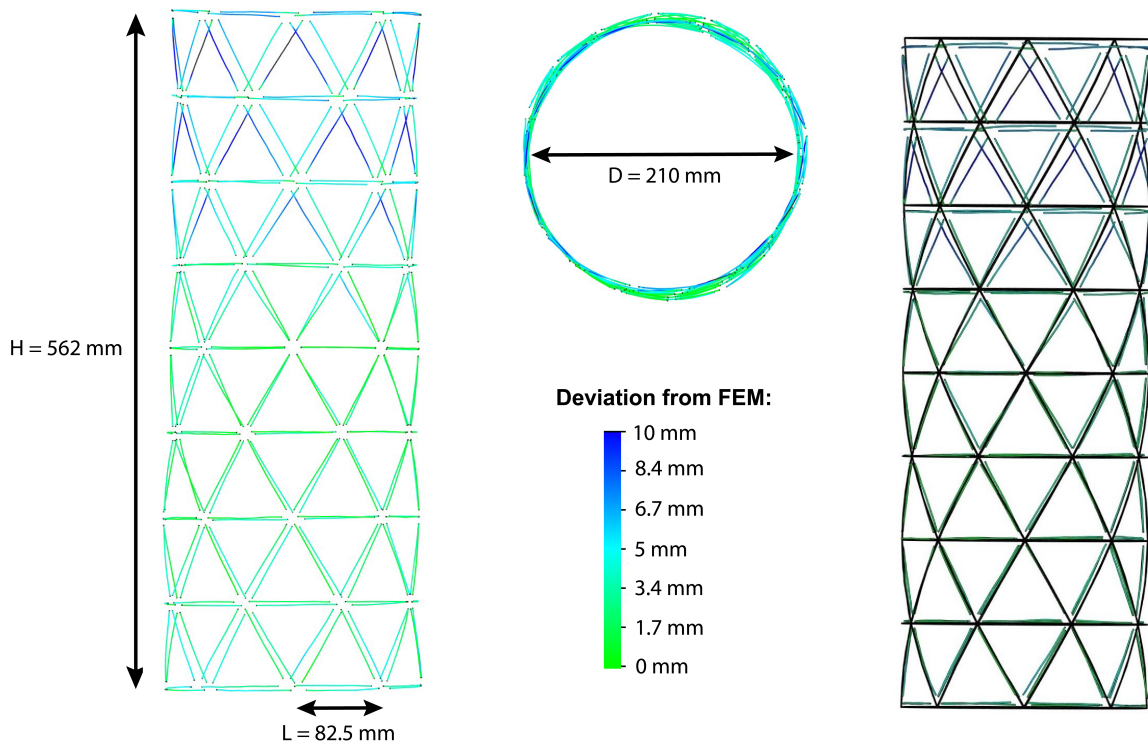


Figure 5-5: Shape deviations between the simulated and actual shape of a Bend-Formed isogrid column. The simulated shape is calculated through a finite element analysis while the actual shape is measured using a white light 3D scanner [104]. The maximum deviations occur near the top of the column.

In the immediate vicinity of the middle plane, we see that deviations between the predicted and actual shape are below 1 mm. Farther from the middle plane, however,

the deviations increase and reach a maximum of 1 cm at the top end of the column. To understand these deviations, experimental and simulated shapes are superimposed in Fig. 5-5, which highlights a global twist in the structure. From this comparison, we see that most of the deviations result from a rotation of the struts along the cylinder axis, rather than a mismatch in curvature of each strut. In addition, a top view of the experimental column, shown in Fig. 5-5, reveals an ovalization of the cross-section. These two global imperfections, twist and ovalization, may arise from the last step of the fabrication process, when joints are applied to the boundary nodes of the column after rolling. This process requires local flattening and clamping of the struts near the boundary nodes, which potentially introduces inaccuracies and angular variations in the adjacent struts. This manufacturing step may thus be responsible for the observed deviations in shape.

#### 5.4.2 Buckling and Post-Buckling Response

To understand the experimental results, we simulated compression of Bend-Formed isogrid columns with buckling analyses in Abaqus. In particular, we performed linear eigenvalue analyses and computed various post-buckling responses with the Riks solver by seeding the initial geometry with eigenmodes. We then compared the simulated load-displacement curves and deformed shapes with the experimental results. Below we describe this process for the baseline column and present comparisons between simulation and experiment for all four isogrid columns.

First a buckling eigenvalue analysis is performed for the undeformed baseline column, including the prestress resulting from the rolling step. The analysis computed three buckling eigenvalues under 200 N (the maximum load observed in the experiment), for which the corresponding eigenmodes are shown in Fig. 5-6a. The first buckling eigenvalue,  $F1 = 168.7$  N, corresponds to an axisymmetric eigenmode with sinusoidal deformations at a wavelength equal to twice the bay height. By contrast, the second and third eigenvalues,  $F2 = 181.9$  N and  $F3 = 182.3$  N, correspond to antisymmetric eigenmodes rotated by  $90^\circ$  about the column axis.

In order to simulate the load-displacement response of the baseline column past

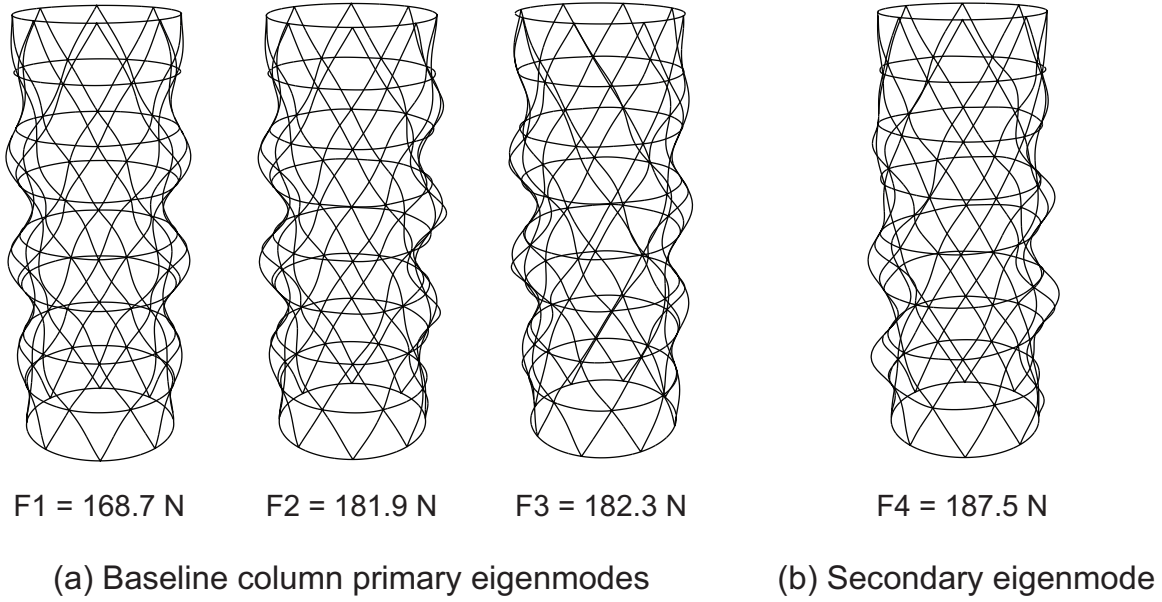


Figure 5-6: Buckling eigenmodes of the baseline isogrid column, computed using a linear buckling analysis in Abaqus. (a) Primary eigenmodes of the baseline column, only one of which is axisymmetric. (b) Secondary eigenmode calculated using an iterative solver.

the first bifurcation, a geometric imperfection based on the first eigenmode (F1) is seeded into the initial geometry. This imperfection is a numerical perturbation which biases the Abaqus solver at the bifurcation, rather than a representation of the actual geometrical imperfections of the column [107, 108]. Several analyses are performed with different amplitudes of the first eigenmode, to determine the smallest imperfection amplitude for which the load-displacement curve transitions from the perfect response to the post-buckling response. For the baseline column, this critical amplitude was found to be 27% of the wire radius, and the resulting post-buckling response is shown in Fig. 5-7 in blue, together with the experimental response.

As depicted in Fig. 5-7, the simulation predicts an initially linear load-displacement path for the baseline column. However, a discrepancy in stiffness is observed between experiment and simulation. This discrepancy may be explained by our modeling setup of the joints, as we assumed perfect load transfer by kinematically coupling all adjacent struts. In reality, the fabricated columns contain snap-fit joints at each node which are made of a softer plastic than the metallic feedstock (as depicted in Fig.

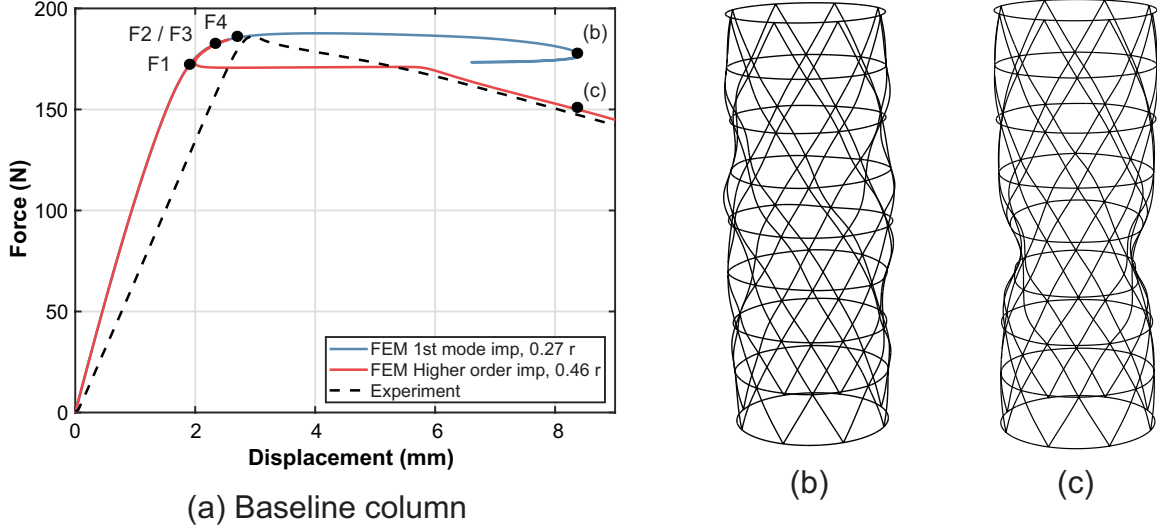


Figure 5-7: Comparison of the load-displacement curve for the baseline column, obtained via experiment (dotted) and simulation (red and blue). Here F1 - F4 correspond to the various buckling eigenvalues of the structure. The blue path is obtained by seeding the initial geometry with the first eigenmode (F1) while the red path is obtained by using the secondary eigenmode (F4) as the imperfection. Deformed shapes at the end of the simulation are shown in (b) and (c).

4-7). Hence, certain adjacent struts transfer load through the softer joint material, which may explain the lower axial stiffness of the fabricated column.

After the first bifurcation (F1), the simulation predicts a stable, nonlinear post-buckling response, as deformations characteristic of the first eigenmode appear in the structure. Given the shape of the first eigenmode, we suspect that the post-buckling stiffness of the column depends mostly on the local bending stiffness of the truss unit cell. Past the second eigenvalue (F2), deformations become antisymmetric and uniformly distributed along the column height, until the maximum load is reached. This maximum load matches well between experiment and simulation, as depicted in Fig. 5-7. In addition, the simulation showed that the maximum load does not depend on the imperfection amplitude, once the critical amplitude used to trigger bifurcation is used. This behavior differs significantly from the high imperfection sensitivity observed in thin cylindrical shells [109], therefore enabling a robust prediction of the maximum load the Bend-Formed column can withstand. Past the maximum load, the simulation predicts a reduction in load-carrying capability which corresponds to

a localization of deformations at two separate locations in the structure, as seen in Fig. 5-7b. At a displacement of 8.2 mm, a snap-back instability is encountered and the simulation is stopped.

By seeding the initial geometry with the first eigenmode, we observe a mismatch between the experimental and simulated post-buckling responses. In addition, the deformed shape obtained at the end of the blue path, shown in Fig. 5-7b, is significantly different from the shape observed in the experiment. This difference suggests that there may be additional bifurcations on the primary post-buckling path. To find them, we iteratively solve the buckling eigenvalue problem [110, 111], between the first eigenvalue and the maximum load. With this process, we found a secondary bifurcation at a critical load of  $F4 = 187.5$  N, the corresponding eigenmode of which is shown in Fig. 5-6b. To trace the secondary post-buckling path stemming from this secondary bifurcation, the corresponding eigenmode is seeded in the initial column geometry, in addition to the first mode imperfection considered previously. A parametric study showed that a minimum imperfection amplitude of 46% of the wire radius is needed for the solver to bifurcate when the load reaches  $F4 = 187.5$  N. For this value of imperfection, we obtain the secondary post-buckling path shown in red in Fig. 5-7a.

The red path follows a similar shape as the primary post-buckling path in blue, up to the second bifurcation (F2). After that, it becomes unstable and restabilizes at a load of 171 N, followed by a plateau in load. At a displacement of 5.9 mm, the load starts decreasing again and the post-buckling path follows the experimental response closely. At the end of path, the deformed shape, shown in Fig. 5-7c, features symmetric deformations which localize below the column mid-plane, very close to that observed experimentally. However, while the simulated response exhibits a snap-back instability after the second bifurcation (F2), a gradual decrease in load is observed in the experiment. This difference in behavior may be a result of real imperfections in the structure such as the global cross-section ovalization mentioned in Section 5.4.1. Indeed, the post-buckling shape also features a local ovalization of the cross-section, and therefore the initial imperfection is most likely the seed for this type of

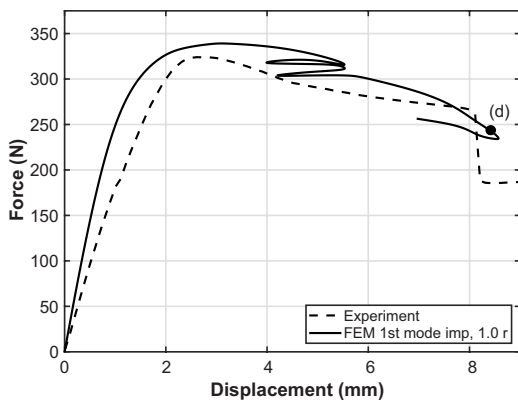
deformation. Since the onset of the mode is already present in the structure, the post-buckling regime consists in the amplitude growth and localization of the initial imperfection, rather than an unstable bifurcation and kinetic energy release which would be observed for a perfect structure. This reasoning also offers an explanation to why the structure would bifurcate at the secondary bifurcation rather than following the primary post-buckling path.

A similar simulation procedure to that outlined above was implemented for the other three Bend-Formed columns—small sidelength, wide, long—to obtain their buckling and post-buckling responses. In particular, an eigenvalue analysis was carried out about the undeformed shape, and the first buckling eigenmode was seeded as an imperfection in the initial shape to trace the post-buckling response. For these analyses, we did not search for additional bifurcations along the post-buckling path and traced only the primary path (i.e., blue path in Fig. 5-7). The resulting post-buckling responses are shown in Fig. 5-8, and the relative errors in initial stiffness and maximum load between simulation and experiment are reported in Table 5.3.

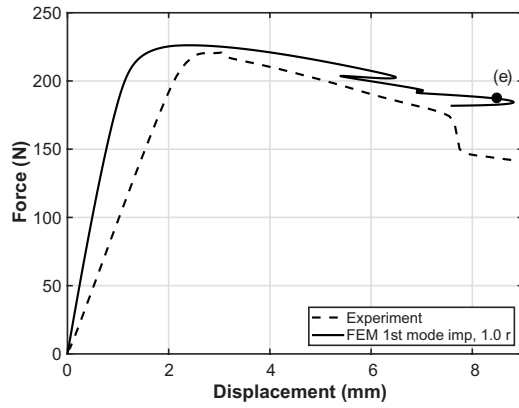
Table 5.3: Relative error between experimental and simulated values of axial stiffness and maximum load for Bend-Formed isogrid columns tested in compression. The simulation consistently overpredicts the axial stiffness but accurately predicts the maximum load.

Column	$k_{axial}$ relative error [%]	$P_{max}$ relative error [%]
Baseline	56.3	0.6
Small sidelength	54.8	4.6
Wide	107	2.4
Long	47.9	3.9

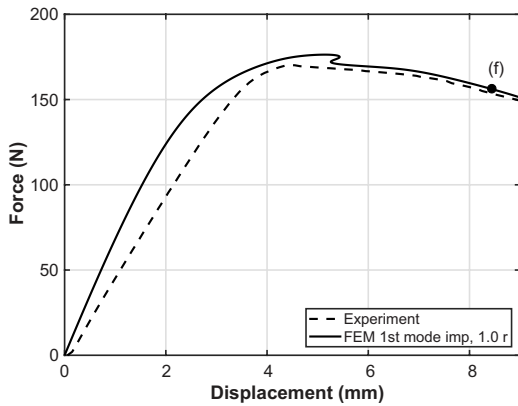
Fig. 5-8 shows a close match between load-displacement curves from experiment and simulation. The simulations predict initially linear paths which quickly become nonlinear as they approach the maximum load, which match well with experimental results. Beyond the maximum load, the simulations predict interesting phenomenon, such as a series of destabilizations and restabilizations for the small sidelength and wide columns. This phenomenon, referred to as “snaking”, is commonly observed in



(a) Small sidelength column



(b) Wide column



(c) Long column

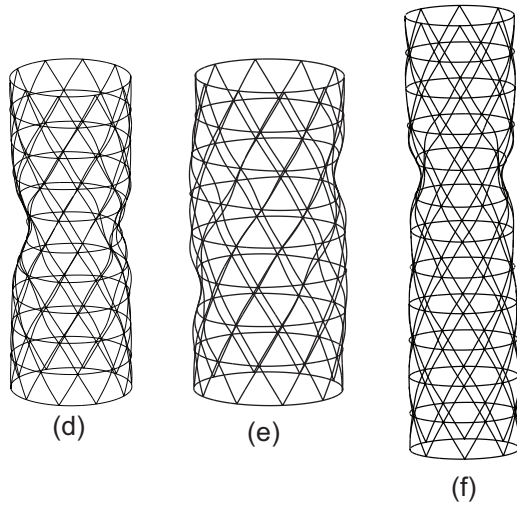


Figure 5-8: Comparison of load-displacement curves for three Bend-Formed isogrid columns, obtained via experiment (dotted) and simulation (solid). The simulated post-buckling paths match well with experimental results, as do the maximum loads. Deformed shapes at the end of the simulations are shown in (d)-(f).



thin cylindrical shells [105] and physically corresponds to the sequential formation of buckles in the columns. In the experiments, these instabilities are likely overshadowed by geometrical imperfections which result in a smooth formation of localized deformations. The simulated post-buckling responses terminate by folding of the path, which coincides with the drop in load observed in experiment when deformations localize on one side of the column.

Comparing the deformed shapes between experiment (Fig. 5-4b-d) and simulation (Fig. 5-8d-f), we observe a good match for the wide and small sidelength columns. However, for the long column, the simulated deformed shape differs from that observed experimentally. In particular, two symmetric localized deformations form in the simulation whereas antisymmetric deformations are observed in experiment. This observation suggests a competition between buckling modes and post-buckling responses, similar to the two paths highlighted for the baseline column (blue and red paths in Fig. 5-7). To fully capture the post-buckling response and deformed shape of each column, an additional search for secondary bifurcations would have to be performed, as presented for the baseline column. Note that the post-buckling load-displacement path is primarily driven by the number of localized buckles rather than their locations, which explains the good match between the two curves in Fig. 5-8c.

From Table 5.3, we observe that the simulation consistently overpredicts the initial axial stiffness of the Bend-Formed columns. This discrepancy is likely due to our assumption of rigid joints in the model, which does not consider the axial compliance of the joints. Nevertheless, an excellent match is observed between the computed and experimental maximum loads (with relative error lower than 5%), suggesting that the buckling behavior of Bend-Formed isogrid columns is imperfection insensitive. This may be a result of the geometry and fabrication process of the Bend-Formed columns, which results in initially curved struts which behave as beam-columns. Consequently, they do not experience Euler buckling and instead follow a nonlinear load-displacement behavior which is less sensitive to imperfections. Conversely, if straight struts were present in the isogrid columns, their buckling behavior would be different and the response would likely be more sensitive to imperfections.

## 5.5 Summary

In this chapter, mechanical tests and finite element analyses were performed on isogrid columns fabricated via Bend-Forming, to guide their design for structural applications. In particular, four column prototypes, each with one geometric parameter independently varied, were axially loaded using an electromechanical load frame to characterize their buckling and post-buckling responses. For all columns, we observed an initially linear load-displacement response, followed by nonlinear softening, a maximum in load, and a gradual decrease in load as the displacement was increased. This region of negative stiffness physically corresponded to the localization of buckling deformations at specific locations along the height of the column.

The corresponding finite element simulations revealed a series of bifurcations on the pre-buckling and post-buckling paths. As multiple post-buckling paths can originate from each bifurcation, we seeded the initial geometries with a series of imperfections based on the buckling eigenmodes to trace the full post-buckling response. The simulations consistently overpredicted the initial stiffness due to the axial compliance of the joints in the experimental specimens, which was not considered in our simulations. However, the simulations accurately predicted the maximum load for all columns before the onset of buckling localization. The simulations showed that these specific columns are imperfection-insensitive beyond the critical imperfection amplitude threshold required to numerically trigger the post-buckling response. Therefore, simulating the compression experiments with near-perfect column models enabled the accurate prediction of maximum load, as well as the full post-buckling response and deformed shape. Considered together, these results provide a simulation framework for accurately predicting the maximum compressive strength of Bend-Formed isogrid columns, for various structural applications.

# Chapter 6

## Application of Bend-Forming for Fabricating Support Structure for an Electrostatically-Actuated Reflector Antenna

### 6.1 Introduction

Having described the Bend-Forming process and investigated the mechanical behavior of columns fabricated with the process, we now present a potential application of Bend-Forming as an ISM approach. Specifically, we study the concept of fabricating supporting structure for a large electrostatically-actuated reflector antenna in space. This antenna concept, originally pioneered in 1980 [112], relies on using electrostatic forces to contour a conductive membrane into a reflector surface. The shape of the membrane can be precisely controlled with a distributed power supply and various electrodes on a command surface below, as depicted in Fig. 6-1.

This concept has been previously ground-tested for antenna and mirror applications. In 2006, for instance, Northrop Grumman successfully retrofitted an AstroMesh antenna with thin film electrodes, demonstrating electrostatic actuation on a 5-m di-

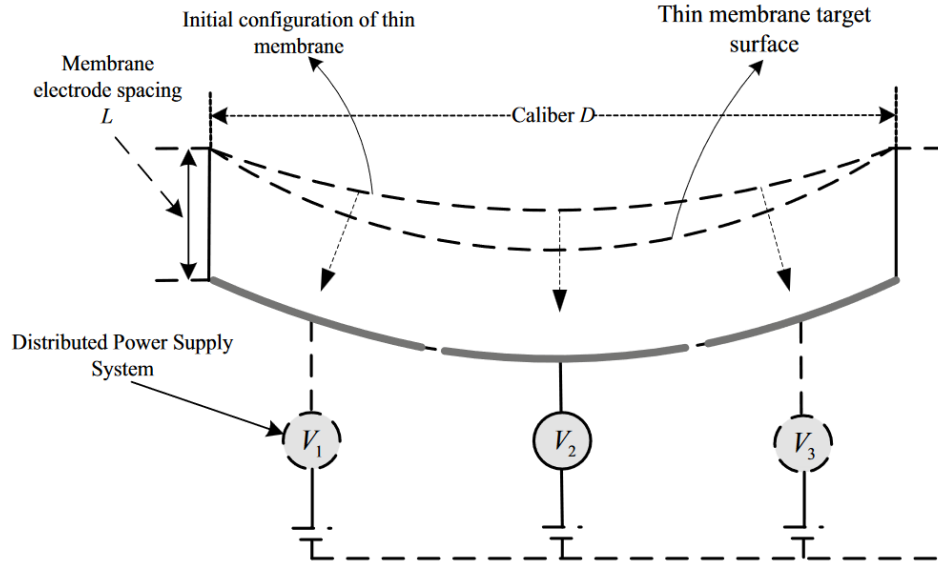


Figure 6-1: Illustration of an electrostatically-actuated reflector antenna. The curved reflector surface is achieved via distributed electrodes on a command surface, which deforms a thin membrane into the target shape. Note this illustration is adapted from [113].

ameter mesh reflector antenna [114]. In addition, electrostatic actuation has been demonstrated for correction of wavefront error in membrane mirrors [115]. These concepts were not pursued further for flight demonstrations, due to lack of funding and technical challenges of electrostatic actuation in the space environment.

As a deformation process which fabricates trusses from continuous feedstock, Bend-Forming can potentially enable such a concept by constructing support structure for the antenna on orbit. To investigate this application, in this chapter we present a structural concept for an electrostatically-actuated reflector antenna, fabricated with Bend-Forming. Below we describe its design and demonstrate the concept with a 1-m diameter prototype, using the fabrication algorithms from Chapter 4 and the understanding of mechanical behavior from Chapter 5. This prototype serves as a demonstration of Bend-Forming for fabricating useful truss structures in space, as well as of electrostatic actuation for antenna applications. Here we focus on the support structure fabricated with Bend-Forming; the description of electrostatic actuation and its control will be summarized in future work. The performance of the prototype as an antenna will also be detailed in future work, after experiments in an

anechoic chamber.

## 6.2 Structural Concept

The key design requirements for support structure of an electrostatically-actuated reflector antenna are based on the dimensions and loads of the membrane and command surface. The first requirement is the aperture size of the antenna, which we assume to be circular with diameter  $D$ . Hence, to support both the membrane and command surface, the surrounding truss structure must at least encompass the dimension  $D$ .

The second requirement relates to the required deflection of the conductive membrane. Since the electrostatically-actuated antenna works by deflecting a thin membrane into a curved shape, the supporting truss structure must be designed to offset the membrane from the command surface by a distance  $\delta$ , which is greater than or equal to the necessary deflection of the membrane. Assuming an initially flat membrane and a parabolic target shape with focal length-to-diameter ratio  $F/D$ , this offset is given by the height of the parabola,  $\delta = D^2/(16F)$ . Thus, the supporting structure must offset the membrane from the command surface by a distance  $H > D^2/(16F)$ .

The third requirement of the support structure is to withstand the tension in the membrane and the electrostatic force as it deflects downwards. Initially, the tension in the membrane acts radially inward, but it develops a vertical component balanced by the electrostatic force as the membrane deflects downwards. Hence the structure must be designed to support these loads in equilibrium without buckling and excessive deflection.

Considering these design requirements, we present in Fig. 6-2 a structural concept for an electrostatically-actuated reflector antenna fabricated with Bend-Forming. The support structure consists of a truss hoop attached to an inner triangular grid. The truss hoop is defined by its inner diameter  $D_{inner}$ , triangular cross section of height  $H$ , and number of attachment points  $N_{hoop}$ . This truss hoop geometry is similar to that presented in Section 4.3 (i.e., with  $N_{CS} = 3$ ,  $N_{side} = 1$ , and  $D_{CS} = 4/3H$ ), but here the cross section has been rotated such that one plane coincides with the inner

triangular grid. This triangular grid is meshed with Delaunay triangulation using an approximate sidelength  $L$  [94], and boundary nodes are adjusted to align with the truss hoop.

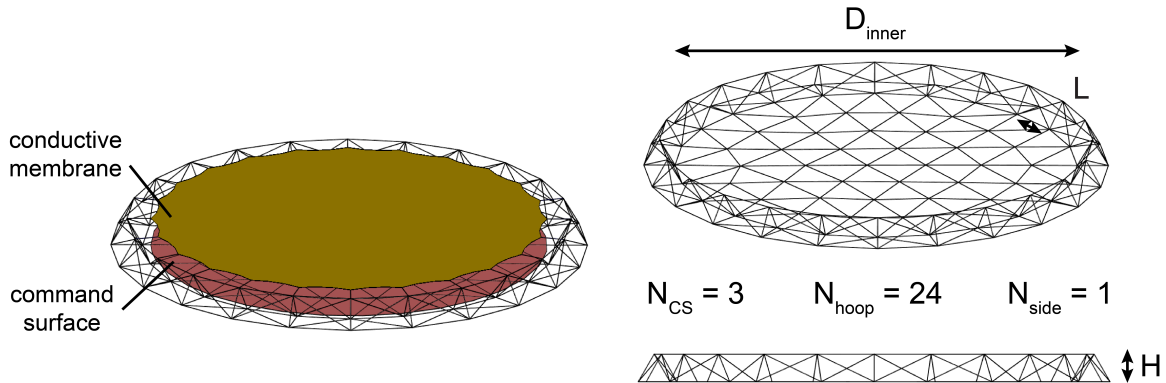


Figure 6-2: Structural concept for an electrostatically-actuated reflector antenna fabricated with Bend-Forming. On the left, an illustration of the conductive membrane and command surface attached to the support structure. On the right, a perspective and side view of the supporting truss structure fabricated with Bend-Forming.

To serve as a reflector antenna, a conductive membrane is connected to the attachment points on the top plane of the truss hoop, and the electrodes of the command surface are attached to the triangular grid below. The gap between the two planes is given by the cross-section height  $H$ , which is designed to be larger than the vertical deflection  $\delta$  required to achieve the desired focal length-to-diameter ratio of the reflector. Additionally, the dimensions of the truss hoop and triangular grid are chosen such that the structure does not buckle due to the tension of the membrane.

Below we present a 1-m diameter prototype of this structural concept, fabricated with Bend-Forming. We verify its design with finite element modeling and a preliminary experiment, demonstrating a potential application of Bend-Formed trusses in space.

### 6.3 Antenna Prototype

For our prototype of the structural concept presented in Fig. 6-2, we targeted an aperture size of  $D = 1$  m and focal length-to-diameter of  $F/D = 1$ , corresponding

to a vertical deflection of  $\delta = 6.25$  cm for the conductive membrane. To account for tolerance stack-up during fabrication of the structure, we selected  $D_{inner} = 1.04$  m for the inner diameter of the truss hoop and  $H = 7$  cm for height of the triangular cross section. Additionally, we chose  $N_{hoop} = 24$  attachment points and an approximate triangle sidelength of  $L = 13$  cm.

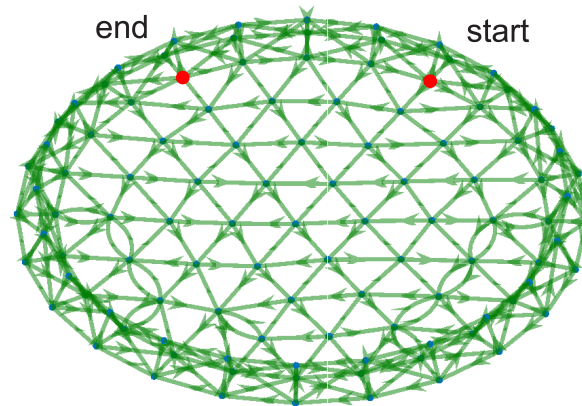
For the conductive membrane, we selected a 40 OPI (openings per inch) gold-molybdenum mesh, a material commonly used in mesh reflector antennas such as the AstroMesh [12]. This mesh must be tensioned within an acceptable range for reflective properties at the desired operation frequency of the antenna. Hence for our prototype, we targeted an X-band application and attached the mesh with an appropriate flat pretension, such that when it deflected to the desired curvature, the tension remained within the acceptable range.

### 6.3.1 Fabrication

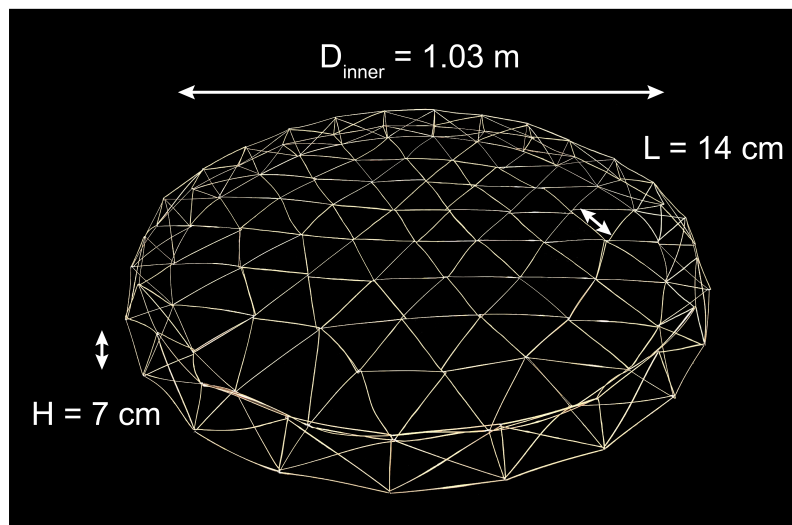
To fabricate the support structure for the antenna prototype with Bend-Forming, we used the fabrication algorithms of Chapter 4. Specifically, we computed 3D bend paths for both the truss hoop and triangular grid, and combined them into a single bend path which traversed the entire geometry, as illustrated in Fig. 6-3a. We converted the resulting bend path into a series of machine instructions and fabricated the structure using the D.I. Wire Pro machine, manually implementing the out-of-plane rotations required for the 3D structure. Finally we added soldered joints at each node, resulting in the prototype shown in Fig. 6-3b.

### 6.3.2 Finite Element Analysis

To verify that the support structure of our antenna prototype would not buckle under the mesh tension and electrostatic forces, we conducted finite element simulations on the truss geometry. Specifically, we imported the geometry into Abaqus and meshed it with linear beam elements (B31), following an identical procedure to that presented for compression of isogrid columns in Chapter 5. However, in this case, we



(a) Continuous bend path



(b) Bend-Formed support structure

Figure 6-3: Fabrication process for Bend-Formed support structure of an electrostatically-actuated reflector antenna. A continuous bend path (a) which traverses both the truss hoop and inner triangular grid is converted to machine instructions for a CNC wire bender, resulting in the fabricated prototype shown in (b). Here soldered joints are used at each node.



simulated tension of the mesh by applying concentrated compressive loads at each attachment point. To account for both the radial and vertical components of the mesh tension, we simulated two loadings: one with forces pointed radially inward and another with forces pointed vertically downwards, as depicted in Fig. 6-4. For both loading scenarios, we implemented simply supported boundary conditions at the outer nodes of the truss hoop.

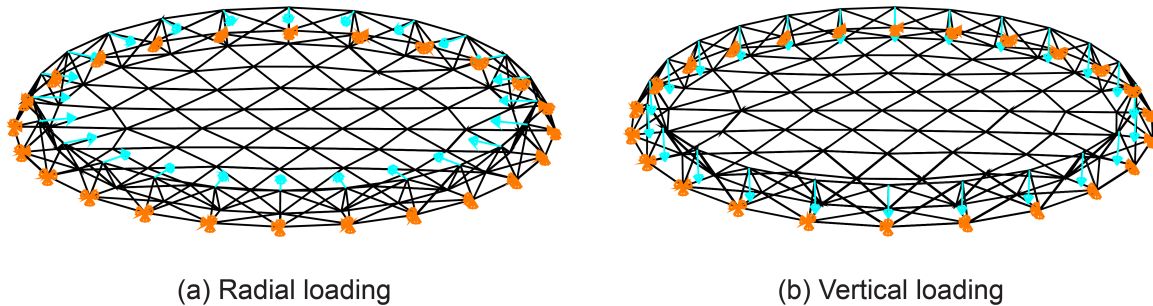


Figure 6-4: Finite element model for compression of the Bend-Formed support structure, with both radial and vertical components of the mesh tension. The load is applied at each attachment point, and simply supported boundary conditions are applied at the outer nodes of the truss hoop. The buckling eigenvalues are found via a linear analysis about the undeformed structure, and a post-buckling path is obtained with the Riks solver by seeding the initial geometry with the first buckling eigenmode.

The goal of the simulation is to understand the buckling behavior of the support structure and verify that the mesh tension will not cause structural failure. To this end, we implemented a buckling eigenvalue analysis linearized about the undeformed geometry, to determine the critical load for both radial and vertical loading. The results, presented in Fig. 6-5, show a radial eigenvalue of 2.11 N and a vertical eigenvalue of 3.70 N at each attachment point, equivalent to a mesh tension of 14.4 N/m and 25.3 N/m, respectively. The corresponding eigenmodes, depicted in Fig. 6-5, are identical and consist of axisymmetric deformations of the circumferential struts. The critical mesh tension of 14.4 N/m is larger than that expected for our mesh at the desired curvature of our antenna prototype, and hence the structure satisfies the design requirement.

To further understand the buckling behavior of the Bend-Formed support structure, we simulated its post-buckling path with the Riks solver, by seeding the initial

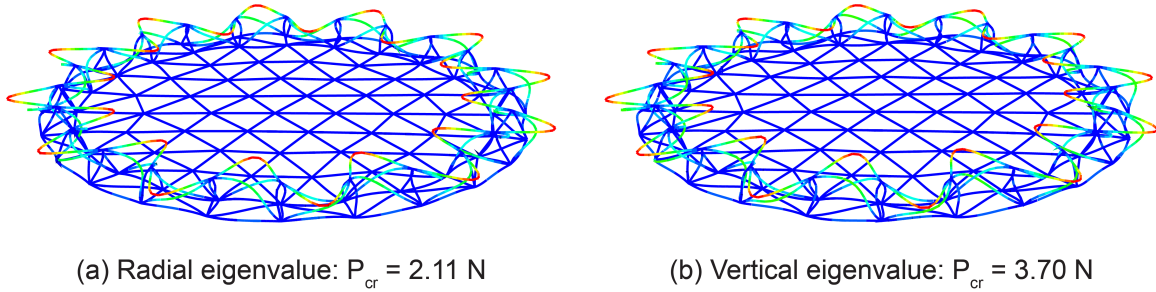


Figure 6-5: Buckling eigenvalues for radial and vertical loading on the Bend-Formed support structure. Here the eigenvalue is the load applied at each attachment point of the perfect structure to cause a bifurcation.

geometry with an imperfection in the shape of the first buckling eigenmode (following a similar procedure as in Chapter 5). We implemented this for radial loading of the structure using the eigenmode shown in Fig. 6-5 and an imperfection amplitude of 10% of the wire radius. The resulting load-displacement curve at one attachment point is plotted in Fig. 6-6, along with the deformed shape at the end of the simulation. We see in Fig. 6-6 that the radial load causes large deformations of the circumferential struts as well as struts in the triangular cross section of the truss hoop. Nonetheless, the simulation predicts a stable post-buckling path, as the stiffness of the structure increases after the first bifurcation. This suggests that the Bend-Formed support structure does not fail catastrophically and continues to support the mesh tension after initial buckling.

### 6.3.3 Experiment

To validate the finite element analysis presented in Section 6.3.2, we conducted a compression experiment on a similar truss geometry to the support structure of the 1-meter diameter antenna prototype. Specifically, we tested the radial compression of a truss hoop fabricated with Bend-Forming on an Instron load frame, in order to compare with the buckling and post-buckling behaviors predicted by simulation.

The truss hoop geometry we tested is depicted in Fig. 6-7 with labeled dimensions and was fabricated with the bend path presented in Section 4.3.3. Soldered joints were used at each node. Note that this truss hoop has a triangular cross section which has

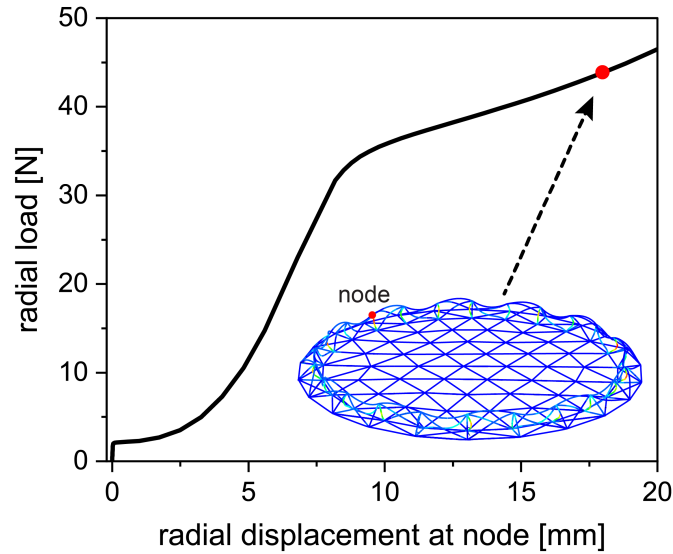


Figure 6-6: Simulated load-displacement curve for radial loading of the Bend-Formed support structure, measured at the labeled node. Here the y-axis represents the radial load applied at each attachment point of the truss hoop. The deformed shape depicts buckling of the circumferential struts as well as struts in the triangular cross section of the truss hoop.

been rotated compared to the structural concept presented in Section 6.2.

To simulate the mesh tension on the truss hoop, we loaded the structure radially at each attachment point. Experimentally, we achieved this via a whiffle tree setup which redirected the vertical displacement of the Instron crosshead to radial displacement at each attachment point. The whiffle tree consisted of six pulleys, two levels of spreader bars, and 1-mm diameter steel wire rope between each level, as depicted in Fig. 6-8a. During the test, we measured the crosshead displacement at the top of the whiffle tree and filmed the structure from above to infer the radial displacement at one of the attachment points. In the simulation, we used the same modeling setup as in Section 6.3.2 to apply concentrated radial loads at each attachment point. The simulation setup is depicted in Fig. 6-8b.

The experimental results are illustrated in Fig. 6-9. Initially we saw a gradual increase in stiffness of the structure, as the steel wire rope used in the whiffle tree became taut. Afterwards, the structure exhibited a relatively linear response with

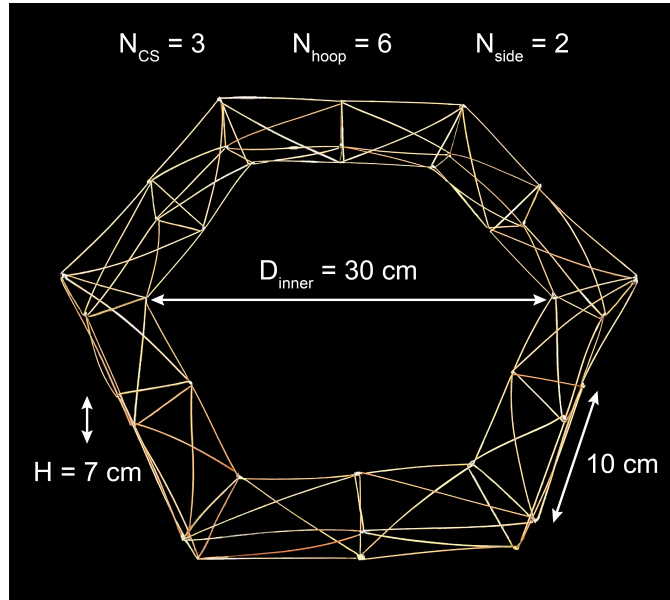


Figure 6-7: Truss hoop fabricated with Bend-Forming, experimentally tested for radial compression with a whiffle tree experimental setup.

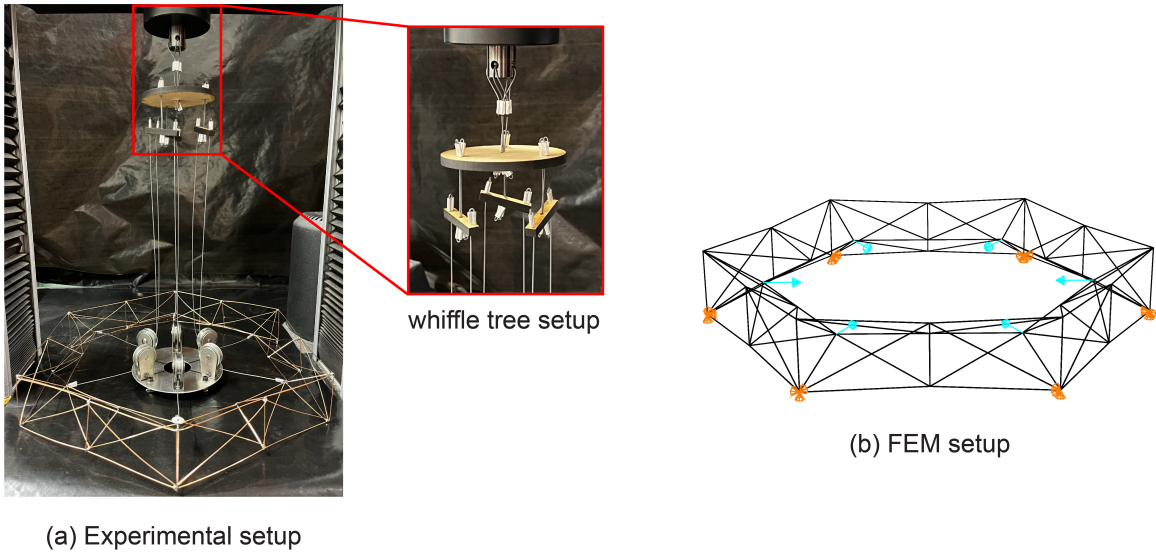


Figure 6-8: Experimental and simulation setups for radial compression of a truss hoop fabricated with Bend-Forming. A whiffle tree setup with pulleys and spreader bars is used to translate the vertical displacement of the crosshead into radial displacement at each attachment point. In the simulation, we apply concentrated radial loads at each attachment point and use simply support boundary conditions at the outer nodes of the truss hoop.

stiffness  $k_{exp} = 31.5 \text{ N/mm}$ , followed by a maximum in load at  $P_{max} = 189 \text{ N}$ . Then, large deformations formed on the right side of the truss hoop as two circumferential struts buckled inward, corresponding to sudden drops in the load. Finally, a soldered joint broke near the buckled struts, causing a larger drop in load and structural failure.

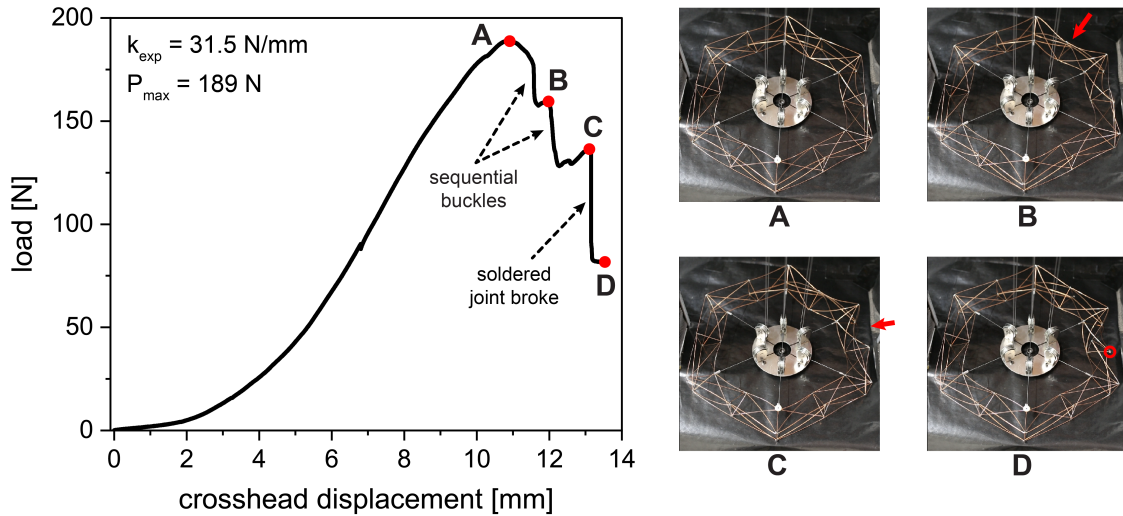
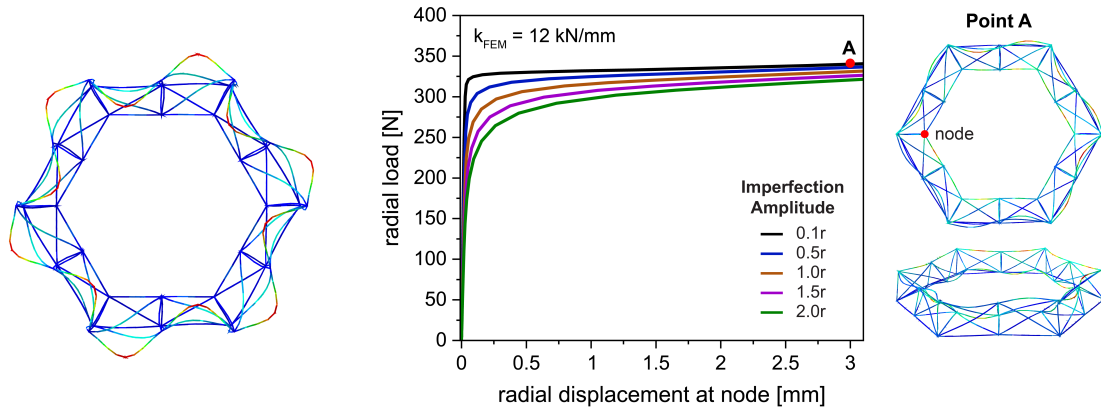


Figure 6-9: Experimental results for radial compression of a truss hoop fabricated with Bend-Forming. The structure achieves a maximum load of  $P_{max} = 189 \text{ N}$  before sequential buckles form on the right side of the hoop (highlighted with red arrows). The final drop in load occurs when a soldered joint breaks (highlighted with the red circle).

To compare these experimental results with simulation, we implemented a buckling eigenvalue analysis about the undeformed truss geometry, following the simulation setup shown in Fig. 6-8b. The resulting buckling eigenmode is depicted in Fig. 6-10a. To simulate the load-displacement curve after the first bifurcation, we seeded this buckling eigenmode as an imperfection on the initial geometry, with varying amplitudes as a function of the wire radius. The resulting post-buckling paths, shown in Fig. 6-10b, feature an initially linear region with stiffness  $k_{FEM} = 12 \text{ kN/mm}$ , followed by a large decrease in stiffness and an asymptotic response. As the imperfection amplitude increases, the maximum load of the structure decreases and the path becomes more nonlinear. The simulated deformed shape consists of circumferential struts buckled both in-plane and out-of-plane, as depicted in in Fig. 6-10b.



(a) Radial eigenvalue:  $P_{cr} = 292.8 \text{ N}$

(b) Simulated post-buckling paths with varying imperfection amplitudes

Figure 6-10: Simulation results for radial compression of a truss hoop fabricated with Bend-Forming. On the left, the first buckling eigenmode of the perfect structure. On the right, five simulated post-buckling paths, using the first buckling eigenmode as an imperfection on the initial geometry with varying amplitudes, and images of the deformed shape.

We observe that the simulated response is quite different from that observed experimentally. First, the maximum load from the experiment is 65% lower than the first buckling eigenvalue, likely due to geometric imperfections in the Bend-Formed structure. For instance, inaccuracies during fabrication caused some struts in the truss hoop to be initially curved and some nodes in the inner circumference to deviate from the central plane of the cross section. These imperfections cause a knockdown in the buckling load of the structure as well as a more nonlinear response, as predicted by the simulated post-buckling paths with large imperfection amplitudes. Second, the simulation predicts a stable post-buckling path while the experiment showed large drops after the maximum load as sequential buckles formed in the structure. This discrepancy could be the result of variations in strength of the soldered joints. In the model we used simplified joints with kinematic coupling, while in reality, the soldered joints have imperfections which cause stress concentrations and failure at some joints before others. Third, it is difficult to directly compare the simulated and experimental load-displacement curves because the experimentally-measured displacement includes the imperfections of the whiffle tree setup (e.g., stretching of the steel wire

rope and bending of the pulleys/spreader bars), which the radial displacement in the simulation does not consider. Hence, to achieve a better match between simulation and experiment, a stiffer whiffle tree setup should be used.

Despite these discrepancies, the above experiment demonstrates the load-carrying capability of the Bend-Formed truss hoop for applications such as supporting a mesh reflector antenna. Future work will explore modeling the soldered joints in greater detail to account for variations in their strength; implementing a more robust experimental setup for testing radial compression of the structure; and testing different hoop geometries with larger diameters and varying cross sections. This will lead to a framework for designing optimized truss hoop geometries, for application as support structure for large antennas in space.

## 6.4 Summary

In this chapter, we explored a potential application of Bend-Forming in space: the fabrication of support structure for an electrostatically-actuated reflector antenna. To this end, we presented a structural concept for this application, consisting of a circular truss hoop connected to an inner triangular grid (Fig. 6-2). We demonstrated this structural concept with a 1-meter diameter antenna prototype, fabricated with Bend-Forming. Additionally, we conducted finite element analyses to verify the strength of the design for supporting a curved reflector membrane. We further validated the finite element models with a preliminary experiment which replicated the tension of the membrane on the Bend-Formed support structure with a whiffle tree setup, and highlighted possible discrepancies between simulation and experiment. Considered together, these results demonstrate the potential of Bend-Forming for fabricating a large electrostatically-actuated reflector antenna in space, for various sensing and communication applications.

While this chapter focused primarily on the structural design of the Bend-Formed support structure, future work will research the electrostatic actuation and control required to deform the membrane into the curved reflector shape of the antenna.

Additionally, the performance of the antenna prototype presented in Section 6.3 will be determined via measurements of its radiation pattern in an anechoic chamber.



# Chapter 7

## Conclusions and Recommendations

### 7.1 Summary and Conclusions

Motivated by the applications of large space structures and the opportunities offered by manufacturing in space, this thesis presented four research contributions to the growing field of in-space manufacturing (ISM).

In Chapter 3 (adapted from the published article in [48]), we presented an engineering framework for comparing potential feedstock materials and processes for ISM. By using quantitative performance metrics such as thermal stability and specific energy consumption, we highlighted feedstock materials and manufacturing approaches particularly suitable to space. Among metals, composites, and plastics, we found that carbon fiber-aluminum, beryllium, and PLA offer the greatest thermal stability, minimal-mass buckling strength, and resistance to disturbance loads, respectively. However, there is no one material which maximizes all performance metrics, motivating the development of multi-material feedstock which combine the strengths of each material class. Additionally, our comparison of ISM approaches using specific energy consumption found that deformation processes require the least energy per kilogram of feedstock, as they do not require any heating of the material. With simplified analyses, we found that deformation processes are 5 to 10 times less energy intensive than melt-based or extrusion-based processes, potentially enabling the fabrication of 100-meter diameter structures in less than a day.

Motivated by this comparison of ISM approaches, in Chapter 4, we introduced a deformation process called Bend-Forming, with potential application to manufacturing truss structures in space. The method relies on the combination of CNC wire bending with mechanical joints to create trusses from a continuous strand of feedstock, via plastic deformation. We presented algorithms for fabricating arbitrary 2D and 3D trusses with Bend-Forming, which are summarized in Appendix B and can also be downloaded from [75]. These algorithms rely on the solution to the route inspection problem for finding continuous bend paths, as well as a geometric algorithm for converting the bend paths into machine instructions for a CNC wire bender. Using this framework, we presented exemplar structures fabricated with Bend-Forming, including reticulated columns, curved gridshells, tetrahedral trusses, and the Stanford bunny.

To guide the design of Bend-Formed trusses for useful applications, in Chapter 5 (adapted from the published article in [103]), we investigated the compressive behavior of isogrid columns fabricated with Bend-Forming. Here we conducted displacement-controlled compression tests on four columns with varying geometries and compared the experimental responses with finite element analyses. We found that for each column, the load-displacement curve is initially linear, becomes nonlinear near the maximum load, and subsequently shows a decrease in load as localized deformations form along the height of the column. With finite element analyses, we accurately predicted the maximum load and localized deformations in the deformed shape of each column, using beam elements and a simplified model of the joints. However, our analyses consistently overpredicted the stiffness of each column, likely due to our modeling choice of the snap-fit joints used to fabricate the physical columns.

Finally, in Chapter 6, we described a potential space application of Bend-Forming: the fabrication of support structure for an electrostatically-actuated reflector antenna. We presented a structural concept for this application, consisting of a truss hoop and an inner triangular grid, and fabricated a 1-meter diameter prototype with Bend-Forming. We verified the strength of the design with finite element simulations and a preliminary experiment which tested radial compression of the truss hoop. From these

analyses we found that the Bend-Formed support structure is capable of holding a thin reflector surface in tension, thereby demonstrating the feasibility of the structural concept.

The various conclusions and lessons from this research are summarized below:

- Three important considerations for choosing feedstock materials for ISM are thermal stability, resistance to disturbance loads, and minimal-mass buckling strength. These considerations can be quantified with three separate material indices as a function of relevant material properties, which can then be used to compare various feedstock materials using property diagrams.
- For thermal stability, the relevant material index is  $M_1 = \frac{\lambda}{\alpha}$ , where  $\lambda$  is the thermal conductivity and  $\alpha$  the coefficient of thermal expansion. For resistance to disturbance loads, the material index is  $M_2 = \eta \left( \frac{E^{1/3}}{\rho} \right)^{(k-1)/2}$ , where  $\eta$  is the material loss coefficient,  $E$  the Young's modulus,  $\rho$  the density, and  $k$  a constant which represents the power spectral density of the disturbance loading. For minimal-mass buckling strength, the material index is  $M_3 = \frac{(\phi_{max}E)^{1/2}}{\rho}$ , where  $\phi_{max}$  is the maximum shape factor of the relevant cross section.
- For thermal stability, promising feedstock materials are Invar and carbon fiber-aluminum composites; for resistance to disturbance loads, carbon fiber-reinforced polymers like CF/PEEK and neat polymers like PLA; and for minimal-mass buckling strength, metals like beryllium and composites like CF/cyanate ester. However, no optimum feedstock materials exist which maximize all three material indices, motivating the development of multi-material feedstocks which leverage the unique properties of each material class.
- Two important considerations for choosing processing methods for ISM are the energy required and the achievable accuracy. These considerations can be quantified with the specific energy consumption per kilogram of feedstock and factors which limit accuracy in the space environment.
- The specific energy consumption of various ISM processes can be estimated us-

ing the physics of their primary shaping mechanisms. For melt-based processes like fused deposition molding and directed energy deposition, the specific energy consumption is a function of the specific heat and melting temperature of the feedstock material. For extrusion processes like pultrusion of carbon fiber-reinforced polymers, the specific energy consumption is a function of the composite specific heat and melting/glass transition temperatures of the polymer matrix. For deformation processes, the specific energy consumption is a function of the strength and density of the feedstock material.

- By comparing the specific energy consumption of melt-based, extrusion, and deformation processes for various feedstock materials, it becomes clear that deformation processes require the least energy per kilogram of feedstock, almost an order of magnitude less than melt-based and extrusion processes. For geometries like the tetrahedral truss, this low energy consumption enables deformation processing of 100-meter diameter structures in less than a day.
- The achievable accuracy of various ISM processes can be compared via limiting factors unique to the space environment. For melt-based AM processes, the lack of convective cooling and the presence of solar heating may magnify thermal stresses during fabrication and cause degradation of mechanical properties. For composite extrusion processes, achieving uniform heating and curing in space may be difficult given varying heat fluxes and thermal radiation. For deformation processes, the primary source of inaccuracy is springback, which may be affected by the varying thermal environment of space, but to a lesser extent than other processes.
- An exemplar deformation process for ISM of truss structures is Bend-Forming, which uses CNC wire bending and mechanical joints to form trusses from a spool of raw feedstock via plastic deformation. With classical algorithms from graph theory and geometry, Bend-Forming can fabricate arbitrary 2D and 3D trusses from a continuous strand of feedstock, such as reticulated columns, curved gridshells, and tetrahedral trusses. The joining methods of interference snap-fits

and soldering show promise for fabricating stiff trusses with Bend-Forming. For implementation in space, other low-power joining methods can be considered, including spot welding, friction stir welding, and ultrasonic welding.

- Before Bend-Formed trusses can be used for space applications, an understanding is needed of their mechanical behavior. To this end, compression experiments on four Bend-Formed isogrid columns reveal a constitutive response different from thin cylindrical shells, with a smooth formation of localized deformations after the maximum load. Finite element analyses with beam elements accurately predict the maximum load of these structures, but consistently overestimate their axial stiffness, likely due to the simplified model of joints used in the analyses.
- One potential application of Bend-Forming is the fabrication of large support structures on orbit, such as for an electrostatically-actuated reflector antenna. A structural concept for this application, consisting of a truss hoop and an inner triangular grid, shows promise for supporting a thin membrane in tension, which deflects downward in response to electrostatic forces to form a reflector surface. Preliminary finite element analyses and experiments show that preventing radial buckling of the truss hoop is a primary structural requirement which is sensitive to geometrical imperfections.

## 7.2 Recommendations for Future Work

The Bend-Forming process described in this thesis is nascent technology in the concept phase. To move to higher technological readiness levels (i.e., TRL 4-6) for Bend-Forming as a manufacturing method in space, further research needs to be conducted. The future research directions can be divided into four main categories: process improvements; feedstock development; considerations for the space environment; and multidisciplinary optimization.

The first category refers to research on improving the Bend-Forming process it-

self. In this category, one task would be to automate all degrees of freedom of the CNC wire bender to enable automatic fabrication. In particular, the out-of-plane rotations of the feedstock for fabricating 3D trusses need to be automated for end-to-end robotic fabrication in space. Second, robust and low-power joining methods need to be implemented simultaneously with the Bend-Forming process, to achieve stiff trusses at each step of the fabrication. For all prototypes presented in this thesis, the joints were manually attached to the truss after fabrication; whereas in space, a robotic system for attaching the joints would need to be integrated with the CNC wire bender. Third, to increase the accuracy of Bend-Formed trusses, an accuracy model of the fabrication process can be developed, incorporating the tolerances of each step. For instance, by using the tolerances of the feed lengths, bend angles, and out-of-plane rotations, the fabrication instructions can be modeled in reverse to determine which tolerances most affect the accuracy of the final structure, as well as the magnitude of the tolerance stack-up.

The second category of future research relates to development of novel feedstock materials compatible with Bend-Forming. As discussed in Chapter 3, the ideal feedstock for ISM applications leverages the unique properties of multiple material classes. This principle can be applied to Bend-Forming, motivating the development of multi-material feedstock such as a spool of carbon fiber-aluminum with high thermal stability. While the plastic deformation required for Bend-Forming restricts potential feedstock options to ductile materials, novel material architectures can be developed which are amenable to both the Bend-Forming process and to the space environment. For instance, high-strain composite tape springs, currently used as deployable booms for spacecraft, can be integrated with metallic wire feedstock to achieve both thermal stability and minimal-mass buckling strength with each Bend-Formed strut. Another concept is to design functionally-graded feedstock with brittle and ductile materials, which are purposefully aligned with regions of plastic deformation during Bend-Forming.

The third research category relates to considerations of Bend-Forming in the space environment, particularly microgravity and temperature variations during orbit. As

the process of CNC wire bending has not been previously tested in space, it is unclear how the space environment affects important process parameters such as springback of the feedstock. Additionally, a machine with forms feedstock via plastic deformation would likely undergo changes in center of mass and moment of inertia during fabrication in microgravity, affecting the attitude and stability of the spacecraft. To study these various effects of the space environment on Bend-Forming, experiments and modeling are needed in representative environments, such as in thermal-vacuum chambers and on parabolic flights.

The final research direction is to pursue multidisciplinary optimization of Bend-Forming in space. Various aspects of the fabrication approach can be optimized for space, such as the algorithms for finding bend paths and the truss geometries themselves. By incorporating additional constraints, bend paths can be found which avoid collision of the fabricated structure with the machine; and with structural optimization, trusses can be designed for specific applications while optimizing for criteria like natural frequency and stiffness. Principles from the established fields of multidisciplinary design optimization and truss topological optimization can be implemented with Bend-Forming, guiding a comprehensive optimization framework for fabrication in space.

With future work in the above research directions, Bend-Forming has potential to enable a new generation of large space structures with increased sensing, communication, and power capabilities.





# Appendix A

## ISM Case Study Expressions

Here we present relevant expressions to the case study in Chapter 3.4 on the in-space manufacturing of a tetrahedral truss supporting a reflector surface. For this truss, each member is assumed to be a straight strut with circular cross section, and the nodal joints are assumed to be massless pin connections. Below we present expressions for the truss mass  $M_t$ , fundamental natural frequency  $f_0$ , mass of deformed material  $M_d$ , and arclength of feedstock  $L_{tot}$  (for deformation processes). Note that some of these expressions are results from an earlier study by Lake et al. on an identical truss geometry [4].

The mass of a tetrahedral truss with corner-to-corner diameter  $D$  and depth  $h$  is

$$M_t = \pi \sqrt{\frac{3}{2}} h \rho r^2 N_{struts}, \quad (\text{A.1})$$

where  $\rho$  is the strut density,  $r$  the strut radius, and  $N_{struts}$  the total number of struts, given by [4]

$$N_{struts} \approx \frac{13}{3} \left( \frac{D}{h} \right)^2. \quad (\text{A.2})$$

The fundamental free-free vibration frequency of the tetrahedral truss is approximated as [4]

$$f_0 = 0.852 \frac{h}{D^2} \sqrt{\eta \frac{E}{\rho}}, \quad (\text{A.3})$$

where  $E$  is the strut Young's modulus and  $\eta$  is the truss mass fraction, defined as

$$\eta = \frac{\text{truss mass}}{\text{total mass}} = \frac{M_t}{M_t + M_r}. \quad (\text{A.4})$$

Here  $M_t$  is the truss mass given in Eq. A.1 and  $M_r$  is the hexagonal reflector mass, approximated with areal density  $\rho_A$  as

$$M_r = \frac{3\sqrt{3}}{8} \rho_A D^2. \quad (\text{A.5})$$

For fixed  $D$  and  $f_0$ , Eq. A.3 shows that an increase in depth-to-diameter ratio decreases the mass fraction, resulting in increased efficiency. However, above the critical ratio of 0.2, the truss can no longer be modeled as a thin plate and Eq. A.3 becomes invalid [4]. Hence, for simplicity, we choose geometries with a fixed depth-to-diameter ratio of 0.2. With this chosen ratio and the areal density of  $\rho_A = 18 \text{ kg/m}^2$  specified in Section 3.4, Eqs. A.1 and A.3 can be expressed as functions of diameter for various feedstock materials of interest.

Next, for deformation processes, assuming the length of deformed material at each node is equal to the strut diameter, the mass of deformed material is given by:

$$M_d = 2\pi \rho r^3 N_{struts}. \quad (\text{A.6})$$

Finally, assuming the total arclength of feedstock for deformation processes equals the total length of struts,

$$L_{tot} = N_{struts} \sqrt{\frac{3}{2}} h. \quad (\text{A.7})$$

# Appendix B

## Bend-Forming Algorithms

Here we present pseudocode for the fabrication algorithms of Bend-Forming. These algorithms can be used to fabricate arbitrary 2D and 3D truss structures with a CNC wire bender, as described in Chapter 4. Working code for these algorithms can be downloaded from [75].

---

**Algorithm 1**

---

```
1: function MAKEEULERIAN( $g, pos$ )
2:    $g_{Eulerian} \leftarrow g$ 
3:   oddnodes = nodes in  $g$  with odd connectivity
4:    $N_{odd} \leftarrow \text{length}(\text{oddnodes})$ 
5:    $N_{pathstoadd} \leftarrow N_{odd}/2 - 1$ 
6:   alloddpairs = all possible pairings of oddnodes
7:   for oddpair in alloddpairs do
8:     oddpath = list of edges in shortest path between oddpair in  $g$ 
9:     oddpathlength = total length of edges in oddpath using  $pos$ 
10:  Sort oddpaths by oddpathlength
11:  for 1 to  $N_{pathstoadd}$  do
12:    Add edges in shortest oddpath to  $g_{Eulerian}$  as doubled struts
13:    Remove oddpaths which contain nodes in the added oddpath
14:  return  $g_{Eulerian}$ 
```

---

---

**Algorithm 2**

---

```
1: function HIERHOLZER( $g_{Eulerian}$ )
2:    $bendpath \leftarrow \emptyset$ 
3:   oddnodes = nodes in  $g_{Eulerian}$  with odd connectivity
4:   if oddnodes empty then
5:     firstnode  $\leftarrow$  random node in  $g_{Eulerian}$ 
6:   else
7:     firstnode  $\leftarrow$  random node in oddnodes
8:   closedpath  $\leftarrow$  [firstnode]
9:   repeat
10:    currentnode = closedpath(end)
11:    neighbors = neighbors of currentnode
12:    if neighbors empty then
13:      Append currentnode to  $bendpath$ 
14:      Remove currentnode from closedpath
15:    else
16:      randneighbor = random member of neighbors
17:      Append randneighbor to closedpath
18:      Remove edge between currentnode and randneighbor from  $g_{Eulerian}$ 
19:    until closedpath empty
20:  return  $bendpath$ 
```

---

---

**Algorithm 3**

---

```
1: function GEOMETRICALGORITHM(bendpath, pos)
2:   MachineInstructions  $\leftarrow \emptyset$ 
3:   for node in first node to second to last node of bendpath do
4:     if node = second to last node then ▷ Edge case: last nodes
5:        $\vec{x}_1$  = coords of node
6:        $\vec{x}_2$  = coords of last node
7:        $L_{feed} = \vec{x}_2 - \vec{x}_1$  ▷ Calculate  $L_{feed}$ 
8:       Add "FEED  $L_{feed}$ " to MachineInstructions
9:     else
10:       $\vec{x}_1$  = coords of node
11:       $\vec{x}_2$  = coords of next node
12:       $\vec{x}_3$  = coords of next next node
13:      doubledwire = 0
14:      if node = first node then ▷ Edge case: first nodes
15:         $\text{sign}(\theta_{bend}) = 1$ 
16:         $\hat{n}_{current} = ((\vec{x}_3 - \vec{x}_2) \times (\vec{x}_1 - \vec{x}_2))$ 
17:      else if  $\vec{x}_1 = \vec{x}_3$  then ▷ Edge case: doubled wire
18:        doubledwire = 1
19:         $\text{sign}(\theta_{bend}) = -\text{sign}(\theta_{bend})$ 
20:      else ▷ All other nodes
21:         $\hat{n}_{next} = ((\vec{x}_3 - \vec{x}_2) \times (\vec{x}_1 - \vec{x}_2)) * \text{sign}(\theta_{bend})$ 
22:        if  $\hat{n}_{next}$  parallel to  $\hat{n}_{current}$  then
23:           $\theta_{rotate} = 0^\circ$ 
24:          if  $\hat{n}_{next}$  in opposite direction as  $\hat{n}_{current}$  then
25:             $\text{sign}(\theta_{bend}) = -\text{sign}(\theta_{bend})$ 
26:          else
27:             $\vec{v}_{rotaxis} = (\vec{x}_2 - \vec{x}_1) * \text{sign}(\theta_{bend})$  ▷ Allowed rotation axis
28:             $\vec{v}_{rotvec} = \text{proj}(\hat{n}_{next} \times \hat{n}_{current}, \vec{v}_{rotaxis})$ 
29:            if  $\vec{v}_{rotvec}$  in same direction as  $\vec{v}_{rotaxis}$  then
30:               $\theta_{rotate} = 180^\circ - \text{anglebtw}(\hat{n}_{current}, \hat{n}_{next})$  ▷ Calculate  $\theta_{rotate}$ 
31:               $\hat{n}_{current} = \hat{n}_{next}$ 
32:            else
33:               $\theta_{rotate} = 180^\circ - \text{anglebtw}(-\hat{n}_{current}, \hat{n}_{next})$ 
34:               $\hat{n}_{current} = -\hat{n}_{next}$ 
35:               $\text{sign}(\theta_{bend}) = -\text{sign}(\theta_{bend})$ 
36:          if  $\theta_{rotate} \neq 0^\circ$  then
37:            Add "ROTATE  $\theta_{rotate}$ " to MachineInstructions
```

---

---

```

38:       $L_{feed} = \vec{x}_2 - \vec{x}_1$                                 ▷ Calculate  $L_{feed}$ 
39:      Add "FEED  $L_{feed}$ " to MachineInstructions
40:      if doubledwire then
41:           $|\theta_{bend}| = 180^\circ$                                 ▷ Edge case: doubled wire
42:      else
43:           $|\theta_{bend}| = 180^\circ - \text{anglebtw}(\vec{x}_3 - \vec{x}_2, \vec{x}_1 - \vec{x}_2)$     ▷ Calculate  $\theta_{bend}$ 
44:           $\theta_{bend} = |\theta_{bend}| * \text{sign}(\theta_{bend})$ 
45:          Add "BEND  $\theta_{bend}$ " to MachineInstructions
46:      return MachineInstructions

```

---

# Bibliography

- [1] R.V. Powell, "A Future for Large Space Antennas," *7th Communications Satellite Systems Conference*, April 24–27, 1978 (San Diego, CA), AIAA, 1978, p 407–414
- [2] J.M. Hedgepeth and L.R. Adams, "*Design Concepts for Large Reflector Antenna Structures*," 1983, NASA Contractor Report 3663
- [3] R.A. Russell, T.G. Campbell, and R.E. Freeland, "A Technology Development Program for Large Space Antennas," *Inter. Astronautical Congr. of the Intern. Astronautical Federation*, September 22–29, 1980 (Tokyo, Japan), NASA Technical Memorandum 81902
- [4] M.S. Lake, L.D. Peterson, and M.B. Levine, Rationale for Defining Structural Requirements for Large Space Telescopes, *J. Spacecr. Rocket.*, 2002, 39(5), p 674–681. <https://doi.org/10.2514/2.3889>
- [5] P.E. Glaser, Power from the Sun: Its Future, *Science*, 1968, 162, p 857–861. <https://doi.org/10.1126/science.162.3856.857>
- [6] R.H. MacNeal, J.M. Hedgepeth, and H.U. Schuerch, "*Heliogyro Solar Sailer Summary Report*," 1969, NASA Contractor Report 1329
- [7] B.H. Lambrigtsen, S.T. Brown, S.J. Dinardo, T.C. Gaier, P.P. Kangaslahti, and A.B. Tanner, "GeoSTAR: A Geostationary Microwave Sounder for the Future," *Proc. SPIE 6677, Earth Observing Systems XII*, September 27, 2007 (San Diego, CA), SPIE, 2007, p 66771B. <https://doi.org/10.1117/12.731933>
- [8] M. Arya, N. Lee, and S. Pellegrino, "Ultralight Structures for Space Solar Power Satellites," *3rd AIAA Spacecraft Structures Conference*, January 4–8, 2016 (San Diego, CA), AIAA, 2016. <https://doi.org/10.2514/6.2016-1950>
- [9] M. Straubel, J. Block, M. Sinapius, and C. Hu"hne, "Deployable Composite Booms for Various Gossamer Space Structures," *52nd AIAA/ASME/ASCE/AHS/ASC Structures, Structural Dynamics and Materials Conference*, April 4–7, 2011 (Denver, CO), AIAA, 2011. <https://doi.org/10.2514/6.2011-2023>

- [10] M.K. Chamberlain, S.H. Kiefer, and J. Banik, "On-Orbit Structural Dynamics Performance of the Roll-Out Solar Array," *2018 AIAA Spacecraft Structures Conference*, January 8–12, 2018 (Kissimmee, FL), AIAA, 2018. <https://doi.org/10.2514/6.2018-1942>
- [11] L. Johnson, M. Whorton, A. Heaton, R. Pinson, G. Laue, and C. Adams, NanoSail-D: A Solar Sail Demonstration Mission, *Acta Astronaut.*, 2011, 68(5–6), p 571–575. <https://doi.org/10.1016/j.actaastro.2010.02.008>
- [12] M. Mobrem, S. Kuehn, C. Spier, and E. Slimko, "Design and Performance of Astromesh Reflector Onboard Soil Moisture Active Passive Spacecraft," *2012 IEEE Aerospace Conference*, March 3–10, 2012 (Big Sky, MT), IEEE, 2012. <https://doi.org/10.1109/AERO.2012.6187094>
- [13] J.A. Banik, "Realizing Large Structures in Space," *2015 US Frontiers of Engineering*, September 9–11, 2015 (Irvine, CA), National Academy of Engineering
- [14] A. Brinkmeyer, S. Pellegrino, and P.M. Weaver, Effects of Long-term Stowage on the Deployment of Bistable Tape Springs, *J. Appl. Mech.*, 2016, 83(1), 011008. <https://doi.org/10.1115/1.4031618>
- [15] K. Taminger and R.A. Hafley, "Electron Beam Freeform Fabrication: A Rapid Metal Deposition Process," *Proc. 3rd Automotive Composites Conference*, September 9–10, 2003 (Troy, MI), Society of Plastics Engineers, 2003
- [16] J. Kugler, J. Cherston, E.R. Joyce, P. Shestople, and M.P. Snyder, "Applications for the Archinaut In Space Manufacturing and Assembly Capability," *AIAA SPACE and Astronautics Forum and Exposition*, September 12–14, 2017 (Orlando, FL), AIAA, 2017. <https://doi.org/10.2514/6.2017-5365>
- [17] B. Levedahl, R. Hoyt, J. Gorges, T. Silagy, N. Britton, G. Jimmerson, M. Bodnar, and J. Slostad, "Trusselator™ Technology for In-Situ Fabrication of Solar Array Support Structures," *2018 AIAA Spacecraft Structures Conference*, January 8–12, 2018 (Kissimmee, FL), AIAA, 2018. <https://doi.org/10.2514/6.2018-2203>
- [18] Kleos Space, "Futurism," <https://kleos.space/futurism/>. Accessed 4 October 2021
- [19] Grumman Aerospace Corp., "Space Fabrication Demonstration System: Final Report, Technical Volume," Bethpage, NY, 1979, NASA Report N79-29213
- [20] L. Browning and J.B. Hunt, "Space Construction Automated Fabrication Experiment Definition Study (SCAFEDS): Final Report, Volume II, Study Results," San Diego, CA, 1978, NASA Contractor Report 160288
- [21] H.L. Eaker, "Significant Electronic Applications and Experimental Results from Project Echo," WESCON/65, August 24–27, 1965 (San Francisco, CA), NASA Technical Memorandum X-733-65-448



- [22] R.E. Freeland, G.D. Bilyeu, G.R. Veal, M.D. Steiner, and D.E. Carson, Large Inflatable Deployable Antenna Flight Experiment Results, *Acta Astronaut.*, 1997, 41(4), p 267–277. [https://doi.org/10.1016/S0094-5765\(98\)00057-5](https://doi.org/10.1016/S0094-5765(98)00057-5)
- [23] J.F. Garibotti, A.J. Cwiertny, and R. Johnson, On Orbit Fabrication and Assembly of Large Space Structural Subsystems, *Acta Astronaut.*, 1980, 7(7), p 847–865. [https://doi.org/10.1016/0094-5765\(80\)90075-2](https://doi.org/10.1016/0094-5765(80)90075-2)
- [24] J.J. Watson, T.J. Collins, and H.G. Bush, “A History of Astronaut Construction of Large Space Structures at NASA Langley Research Center,” *Proc. IEEE Aerospace Conference*, March 9–16, 2002 (Big Sky, MT), IEEE, 2002, 7-3569–7-3587. <https://doi.org/10.1109/AERO.2002.1035334>
- [25] S. Ahmed and J.F. Clemmet. “Requirements, Design and Development of Large Space Antenna Structures,” *49th Structures and Materials Panel Meeting*, October 7–12, 1979 (Porz-Wahn, Germany), NATO, 1980
- [26] T. Murphey, “Historical Perspectives on the Development of Deployable Reflectors,” *50th AIAA/ASME/ASCE/AHS/ASC Structures, Structural Dynamics and Materials Conference*, May 4–7, 2009 (Palm Springs, CA), AIAA, 2009. <https://doi.org/10.2514/6.2009-2605>
- [27] K. Miura and Y. Miyazaki, Concept of the Tension Truss Antenna, *AIAA J.*, 1990, 28(6), p 1098–1104. <https://doi.org/10.2514/3.25172>
- [28] E.O. Adams and C.N. Irvine, “*MSFC Evaluation of the Space Fabrication Demonstration System (Beam Builder)*,” Marshall Space Flight Center, 1981, NASA Technical Memorandum 82440
- [29] M. Moraguez and O. de Weck, "Benefits of In-Space Manufacturing Technology Development for Human Spaceflight," *2020 IEEE Aerospace Conference*, March 7-14, 2020 (Big Sky, MT), IEEE, 2020. <https://doi.org/10.1109/AERO47225.2020.9172304>
- [30] A. E. Trujillo, M. T. Moraguez, A. Owens, S. I. Wald, and O. De Weck, “Feasibility Analysis of Commercial In-Space Manufacturing Applications,” *AIAA SPACE and Astronautics Forum and Exposition*, September 12-14, 2017 (Orlando, FL), AIAA, 2017. <https://doi.org/10.2514/6.2017-5360>
- [31] M. T. Moraguez, “Modeling and Optimization of In-Space Manufacturing to Inform Technology Development,” Ph.D. Dissertation, Department of Aeronautics and Astronautics, Massachusetts Institute of Technology, Cambridge, MA, 2021. <https://dspace.mit.edu/handle/1721.1/139928>
- [32] USA National Science and Technology Council, "In-Space Servicing, Assembly, and Manufacturing National Strategy," April 2022. <https://www.whitehouse.gov/wp-content/uploads/2022/04/04-2022-ISAM-National-Strategy-Final.pdf>

- [33] NASA, "OSAM-1 Mission: On-Orbit Servicing, Assembly, and Manufacturing 1," <https://nexis.gsfc.nasa.gov/osam-1.html>. Accessed 11 May 2022
- [34] NASA, "On-Orbit Servicing, Assembly, and Manufacturing 2 (OSAM-2)," [https://www.nasa.gov/mission\\_pages/tdm/osam-2.html](https://www.nasa.gov/mission_pages/tdm/osam-2.html). Accessed 11 May 2022
- [35] ESA, "The Future is Here: Advanced Manufacturing for Space," [https://www.esa.int/Enabling\\_Support/Space\\_Engineering\\_Technology/The\\_future\\_is\\_here\\_Advanced\\_Manufacturing\\_for\\_space](https://www.esa.int/Enabling_Support/Space_Engineering_Technology/The_future_is_here_Advanced_Manufacturing_for_space). Accessed 11 May 2022
- [36] A. Makaya, L. Pambaguian, T. Ghidini, T. Rohr, U. Lafont, and A. Meurisse, 2022. Towards Out of Earth Manufacturing: Overview of the ESA Materials and Processes Activities on Manufacturing in Space. *CEAS Space J.*, 2022. <https://doi.org/10.1007/s12567-022-00428-1>
- [37] Scientific American, "China Wants to Build a Mega Spaceship That's Nearly a Mile Long," <https://www.scientificamerican.com/article/china-wants-to-build-a-mega-spaceship-thats-nearly-a-mile-long/>. Accessed 11 May 2022
- [38] Redwire Space, "Additive Manufacturing Facility (AMF)," <https://redwirespace.com/products/amf/>. Accessed 11 May 2022
- [39] Redwire Space, "Ceramics Manufacturing Module (CMM)," <https://redwirespace.com/products/cmm/>. Accessed 11 May 2022
- [40] Redwire Space, "3D BioFabrication Facility (BFF)," <https://redwirespace.com/products/bff/>. Accessed 11 May 2022
- [41] NASA, "NextSTEP B: FabLab," <https://www.nasa.gov/nextstep/fablab>, Accessed 11 May 2022
- [42] Axiom Space, "Manufacturing," <https://www.axiomspace.com/manufacturing>. Accessed 11 May 2022
- [43] Orbital Assembly Corporation, "Pioneer Station," <https://orbitalassembly.com/voyager>. Accessed 11 May 2022
- [44] A. Ekblaw, "Self-Aware Self-Assembly for Space Architecture: Growth Paradigms for In-Space Manufacturing," Ph.D. Dissertation, Program in Media Arts and Sciences, Massachusetts Institute of Technology, Cambridge, MA, 2020. <https://dspace.mit.edu/handle/1721.1/129269>
- [45] R.P. Mueller, N.J. Gelino, J.D. Smith, B.C. Buckles, T. Lippitt, J.M. Schuler, A.J. Nick, M.W. Nugent, and I.I. Townsend, "Zero Launch Mass Three-Dimensional Print Head," *16th Biennial International Conference on Engineering, Science, Construction, and Operations in Challenging Environments*, April

- 9-12, 2018 (Cleveland, OH), ASCE, 2018, p. 219–232. <https://doi.org/10.1061/9780784481899.022>
- [46] AI SpaceFactory, "MARSHA: AI SpaceFactory's Mars Habitat," <https://www.aispacefactory.com/marsha>. Accessed 11 May 2022
- [47] M. von Unwerth, A. Voss, S. Stapperfend, S. Linke, and E. Stoll, "Simulation of the Robotic Lunar Prototype MIRA3D," *German Aerospace Congress 2019*, Germany Aerospace Society, 2020. <https://doi.org/10.25967/490161>
- [48] H. G. Bhundiya, F. Royer, and Z. Cordero, Engineering Framework for Assessing Materials and Processes for In-Space Manufacturing, *J. of Materi Eng and Perform*, 2022, 31(2). <https://doi.org/10.1007/s11665-022-06755-y>
- [49] J.M. Hedgepeth, Accuracy Potentials for Large Space Antenna Reflectors with Passive Structure, *J. Spacecr. Rocket.*, 1982, 19(3), p 211–217. <https://doi.org/10.2514/3.62239>
- [50] M.M. Mikulas, "Structural Efficiency of Long Lightly Loaded Truss and Isogrid Columns for Space Applications," 1978, NASA Technical Memorandum 78687
- [51] M.F. Ashby, "Materials Selection in Mechanical Design," 4th ed., Elsevier Ltd., 2011
- [52] H.G. Bush, M.M. Mikulas, and W.L. Heard, Some Design Considerations for Large Space Structures, *AIAA J.*, 1978, 16(4), p 352–359. <https://doi.org/10.2514/3.60897>
- [53] D. Cebon and N.F. Ashby, Materials Selection for Precision Instruments, *Meas. Sci. Technol.*, 1994, 5(3), p 296–306. <https://doi.org/10.1088/0957-0233/5/3/014>
- [54] Ansys Granta EduPack Software, ANSYS, Inc., Cambridge, UK, 2022
- [55] H.P. Stahl, L.D. Feinberg, and S.C. Texter, "JWST Primary Mirror Material Selection," *Proc. SPIE 5487, Optical, Infrared, and Millimeter Space Telescopes*, October 12, 2004 (Glasgow, UK), SPIE, 2004, p 818–824. <https://doi.org/10.1117/12.549582>
- [56] Materion Corp., "SupremEX Metal Matrix Composites Improve Precision in Space and Defense Systems," <https://materion.com/products/metal-matrix-composites/supremex/space-defense-and-optical-systems>. Accessed 18 April 2022
- [57] T. Gutowski, S. Jiang, D. Cooper, G. Corman, M. Hausman, J. Manson, T. Schudeleit, K. Wegener, M. Sabelle, J. Ramos-Grez, and D.P. Sekulic, Note on the Rate and Energy Efficiency Limits for Additive Manufacturing: Rate and Energy Efficiency Limits for AM, *J. Ind. Ecol.*, 2017, 21(S1), p S69–S79. <https://doi.org/10.1111/jiec.12664>

- [58] Z. Liu, Q. Jiang, F. Ning, H. Kim, W. Cong, C. Xu, and H. Zhang, Investigation of Energy Requirements and Environmental Performance for Additive Manufacturing Processes, *Sustainability*, 2018, 10(10), p 3606. <https://doi.org/10.3390/su10103606>
- [59] S.W. Tsai and H.T. Hahn, *Introduction to Composite Materials*, Technomic Publishing Co., Inc., Pennsylvania, 1980
- [60] J.A. Schey, *Introduction to Manufacturing Processes*, McGraw-Hill Inc., New York, 1977
- [61] A. Deignan, L. Figiel, and M.A. McCarthy, Insights into Complex Rheological Behaviour of Carbon Fibre/PEEK from a Novel Numerical Methodology Incorporating Fibre Friction and Melt Viscosity, *Compos. Struct.*, 2018, 189, p 614–626. <https://doi.org/10.1016/j.compstruct.2018.01.084>
- [62] J.M. Hedgepeth, Influence of Fabrication Tolerances on the Surface Accuracy of Large Antenna Structures, *AIAA J.*, 1982, 20(5), p 680–686. <https://doi.org/10.2514/3.7936>
- [63] A. Boschetto and L. Bottini, Accuracy Prediction in Fused Deposition Modeling, *Int. J. Adv. Manuf. Technol.*, 2014, 73(5–8), p 913–928. <https://doi.org/10.1007/s00170-014-5886-4>
- [64] W.J. Sames, F.A. List, S. Pannala, R.R. Dehoff, and S.S. Babu, The Metallurgy and Processing Science of Metal Additive Manufacturing, *Int. Mater. Rev.*, 2016, 61(5), p 315–360. <https://doi.org/10.1080/09506608.2015.1116649>
- [65] R. Hafley, K. Taminger, and R. Bird, “Electron Beam Freeform Fabrication in the Space Environment,” *45th AIAA Aerospace Sciences Meeting and Exhibit*, January 8–11, 2007 (Reno, NV), AIAA, 2007. <https://doi.org/10.2514/6.2007-1154>
- [66] K. Minchenkov, A. Vedernikov, A. Safonov, and I. Akhatov, Thermoplastic Pultrusion: A Review, *Polymers*, 2021, 13(2), p 180. <https://doi.org/10.3390/polym13020180>
- [67] C. Ajinjeru, V. Kishore, J. Lindahl, Z. Sudbury, A.A. Hassen, B. Post, L. Love, V. Kunc, and C. Duty, The Influence of Dynamic Rheological Properties on Carbon Fiber-Reinforced Polyetherimide for Large-Scale Extrusion-based Additive Manufacturing, *Int. J. Adv. Manuf. Technol.*, 2018, 99(1–4), p 411–418. <https://doi.org/10.1007/s00170-018-2510-z>
- [68] S.K. Romberg, M.A. Islam, C.J. Hershey, M. DeVinney, C.E. Duty, V. Kunc, and B.G. Compton, Linking Thermoset Ink Rheology to the Stability of 3D-printed Structures, *Addit. Manuf.*, 2021, 37, 101621. <https://doi.org/10.1016/j.addma.2020.101621>

- [69] COMSOL Multiphysics Reference Manual, v. 5.6, COMSOL, Inc., [www.comsol.com](http://www.comsol.com)
- [70] O.G. Kravchenko, S.G. Kravchenko, and R.B. Pipes, Chemical and Thermal Shrinkage in Thermosetting Prepreg, *Compos. A Appl. Sci. Manuf.*, 2016, 80, p 72–81. <https://doi.org/10.1016/j.compositesa.2015.10.001>
- [71] H. Yu, S.G. Mhaisalkar, and E.H. Wong, Observations of Gelation and Vitrification of a Thermosetting Resin During the Evolution of Polymerization Shrinkage, *Macromol. Rapid Commun.*, 2005, 26(18), p 1483–1487. <https://doi.org/10.1002/marc.200500333>
- [72] K.J. Yoon and J.S. Kim, Effect of Thermal Deformation and Chemical Shrinkage on the Process Induced Distortion of Carbon/Epoxy Curved Laminates, *J. Compos. Mater.*, 2001, 35(3), p 253–263. <https://doi.org/10.1177/002199801772662244>
- [73] W.F. Hosford and R.M. Caddell, *Metal Forming: Mechanics and Metallurgy*, Cambridge University Press, Cambridge, 2011
- [74] NASA, “Observatory Webb’s Mirrors,” <https://www.jwst.nasa.gov/content/observatory/ote/mirrors/index.html>. Accessed 18 April 2021
- [75] Harsh Bhundiya, “Bend-Forming-Algorithms,” <https://www.mathworks.com/matlabcentral/fileexchange/111195-bend-forming-algorithms>. Accessed 8 May 2022
- [76] Pensa Labs, “D.I. Wire Pro Info,” <https://aetlabs.com/wp-content/uploads/D.I.WireProinfo.pdf>. Accessed 12 April 2022
- [77] D. Jungnickel, “*Graphs, Networks and Algorithms*,” 4th ed., Springer-Verlag Berlin Heidelberg, 2013
- [78] G. Dreifus, K. Goodrick, S. Giles, M. Patel, R.M. Foster, C. Williams, J. Lindahl, B. Post, A. Roschli, L. Love, and V. Kunc, Path Optimization Along Lattices in Additive Manufacturing Using the Chinese Postman Problem, *3D Printing and Additive Manufacturing*, 2017, 4(2), p. 98–104. <https://doi.org/10.1089/3dp.2017.0007>
- [79] Z. Gali, Efficient algorithms for finding maximum matching in graphs. *ACM Comput. Surv.*, 1986, 18(1), p. 23–38. <https://doi.org/10.1145/6462.6502>
- [80] V. S. Deshpande, M. F. Ashby, and N. A. Fleck, Foam Topology: Bending Versus Stretching Dominated Architectures, *Acta Materialia*, 2001, 49(6), p. 1035–1040. [https://doi.org/10.1016/S1359-6454\(00\)00379-7](https://doi.org/10.1016/S1359-6454(00)00379-7)
- [81] Y. Huang, J.V. Carstensen, and C.T. Mueller, 3D Truss Topology Optimization for Automated Robotic Spatial Extrusion, *Proceedings of the IASS Symposium*, 2018, p. 1-8. [https://web.mit.edu/yijiangh/www/papers/HuangCarstensenMueller\\_IASS2018.pdf](https://web.mit.edu/yijiangh/www/papers/HuangCarstensenMueller_IASS2018.pdf)

- [82] K-M.M. Tam, D.J. Marshall, M. Gu, J. Kim, Y. Huang, J. Lavallee, and C.T. Mueller, Fabrication-Aware Structural Optimisation of Lattice Additive-Manufactured with Robot-Arm, *Int. J. Rapid Manufacturing*, 2018, 7(2/3), p. 120-168. [http://web.mit.edu/yijiangh/www/papers/IJRapidM2018\\_KMMTetal.pdf](http://web.mit.edu/yijiangh/www/papers/IJRapidM2018_KMMTetal.pdf)
- [83] IP Automation Inc., "Wire Formers," <https://ipautomationinc.com/wire-formers/>. Accessed 12 April 2022
- [84] FormLabs, "Form 3+," <https://formlabs.com/3d-printers/form-3/>. Accessed 29 April 2022
- [85] M. Pouranvari and S.P.H. Marashi, Critical Review of Automotive Steels Spot Welding: Process, Structure and Properties, *Science and Technology of Welding and Joining*, 2013, 18(5), p. 361-403. <https://doi.org/10.1179/1362171813Y.0000000120>
- [86] N.T. Williams and J.D. Parker, Review of Resistance Spot Welding of Steel Sheets, Part 1 Modelling and Control of weld Nugget Format, *International Materials Reviews*, 2004, 49(2), p. 45-75. <https://doi.org/10.1179/095066004225010523>
- [87] N.T. Williams and J.D. Parker, Review of Resistance Spot Welding of Steel Sheets, Part 2 Factors Influencing Electrode Life, *International Materials Reviews*, 2004, 49(2), p. 77-108. <https://doi.org/10.1179/095066004225010541>
- [88] W. Cai, G. Daehn, A. Vivek, J. Li, H. Khan, R.S. Mishra, and M. Komarasamy, A State-of-the-Art Review on Solid-State Metal Joining, *J. Manuf. Sci. Eng.*, 2019, 141(3), p. 031012. <https://doi.org/10.1115/1.4041182>
- [89] R. S. Mishra and Z. Y. Ma, Friction Stir Welding and Processing, *Mater. Sci. Eng., R*, 2005, 50(1-2), p. 1-78. <https://doi.org/10.1016/j.mser.2005.07.001>
- [90] M. P. Matheny and K. F. Graff, Ultrasonic Welding of Metals, in *Power Ultrasonics*, Elsevier, 2015, p. 259-293. <https://doi.org/10.1016/B978-1-78242-028-6.00011-9>
- [91] S. Matsuoka and H. Imai, Direct Welding of Different Metals used Ultrasonic Vibration, *J. Mater. Process. Technol.*, 2009, 209(2), p. 954-960. <https://doi.org/10.1016/j.jmatprotec.2008.03.006>
- [92] A. A. Ward, M. R. French, D. N. Leonard, and Z. C. Cordero, Grain Growth During Ultrasonic Welding of Nanocrystalline Alloys, *J. Mater. Process. Technol.*, 2018, 254, p. 373-382. <https://doi.org/10.1016/j.jmatprotec.2017.11.049>

- [93] A. Merstallinger, M. Sales, E. Semerad, and B.D. Dunn, “*Assessment of the Cold Welding between Separable Contact due to Impact and Fretting under Vacuum*,” 2009, ESA STM-279. [http://esmat.esa.int/Publications/Published\\_papers/STM-279.pdf](http://esmat.esa.int/Publications/Published_papers/STM-279.pdf)
- [94] P.-O. Persson and G. Strang, A Simple Mesh Generator in MATLAB, *SIAM Rev.*, 2004, 46(2), p. 329-345. <https://doi.org/10.1137/S0036144503429121>
- [95] M.-S. Hartig, Approximation of Gaussian Curvature by the Angular Defect: An Error Analysis, *Math. Comput. Appl.*, 2021, 26(1), 15, <https://doi.org/10.3390/mca26010015>
- [96] K. Watanabe and A.G. Belyaev, Detection of Salient Curvature Features on Polygonal Surfaces, *Computer Graphics Forum*, 2001, 20(3), p. 385-392, <https://doi.org/10.1111/1467-8659.00531>.
- [97] S. Pellegrino and C.R. Calladine, Matrix Analysis of Statically and Kinematically Indeterminate Frameworks, *Int. J. Solids Struct.*, 1986, 22(4), p. 409–428. [https://doi.org/10.1016/0020-7683\(86\)90014-4](https://doi.org/10.1016/0020-7683(86)90014-4)
- [98] NASA JPL, “NuSTAR Deployable Mast,” <https://www.nustar.caltech.edu/page/mast>. Accessed 29 April 2022
- [99] S.E. Forman and J.W. Hutchinson, Buckling of Reticulated Shell Structures, *Int. J. Solids Struct.*, 1970, 6(7), p. 909–932. [https://doi.org/10.1016/0020-7683\(70\)90004-1](https://doi.org/10.1016/0020-7683(70)90004-1)
- [100] S.P. Mai and N.A. Fleck, Reticulated Tubes: Effective Elastic Properties and Actuation Response, *Proc. R. Soc. A.*, 2009, 465(2103), p. 685–708. <https://doi.org/10.1098/rspa.2008.0328>
- [101] S. Malek, T. Wierzbicki, and J. Ochsendorf, Buckling of Spherical Cap Gridshells: A Numerical and Analytical Study Revisiting the Concept of the Equivalent Continuum, *Engineering Structures*, 2014, 75(15), p. 288–298. <https://doi.org/10.1016/j.engstruct.2014.05.049>
- [102] J.D. Hinkle, P. Warren, and L.D. Peterson, Geometric Imperfection Effects in an Elastically Deployable Isogrid Column, *J. Spacecr. Rockets*, 2002, 39(5), p. 662–668. <https://doi.org/10.2514/2.3887>
- [103] H.G. Bhundiya, F. Royer, and Z. Cordero, “Compressive Behavior of Isogrid Columns Fabricated with Bend-Forming,” *AIAA Scitech 2022 Forum*, January 3–7, 2022 (San Diego, CA), AIAA, 2022. <https://doi.org/10.2514/6.2022-2263>
- [104] Creaform, “Go!SCAN 3D,” <https://get.creaform3d.com/lp-goscan-3d/>. Accessed 29 April 2022

- [105] R.M.J. Groh and A. Pirrera, On the Role of Localizations in Buckling of Axially Compressed Cylinders, *Proc. R. Soc. A.*, 2019, 475(2224). <https://doi.org/10.1098/rspa.2019.0006>
- [106] T. Von Karman and H.-S. Tsien, The Buckling of Thin Cylindrical Shells Under Axial Compression, *J. Aeronaut. Sci.*, 1941, 8(8), p. 303–312. <https://doi.org/10.2514/8.10722>
- [107] E. Riks, An Incremental Approach to the Solution of Snapping and Buckling Problems, *Int. J. Solids Struct.*, 1979, 15(7), p. 529–551. [https://doi.org/10.1016/0020-7683\(79\)90081-7](https://doi.org/10.1016/0020-7683(79)90081-7)
- [108] T. Rahman and E.L. Jansen, Finite Element Based Coupled Mode Initial Post-Buckling Analysis of a Composite Cylindrical Shell, *Thin-Walled Structures*, 2010, 48(1), p. 25–32. <https://doi.org/10.1016/j.tws.2009.08.003>
- [109] J.G. Teng, Buckling of Thin Shells: Recent Advances and Trends, *Appl. Mech. Rev.*, 1996, 49(4), p. 263–274. <https://doi.org/10.1115/1.3101927>
- [110] C. Leclerc and S. Pellegrino, Nonlinear Elastic Buckling of Ultra-Thin Coilable Booms. *Int. J. Solids Struct.*, 2020, 203(15), p. 46–56. <https://doi.org/10.1016/j.ijsolstr.2020.06.042>
- [111] F. Royer and S. Pellegrino, “Buckling of Ultralight Ladder-type Coilable Space Structures,” *AIAA Scitech 2020 Forum*, January 6–10, 2020 (Orlando, FL), AIAA, 2020. <https://doi.org/10.2514/6.2020-1437>
- [112] J. H. Lang and D. H. Staelin, "Electrostatically-Controlled Large-Aperture Reflecting Satellite Antennas," *1980 19th IEEE Conference on Decision and Control including the Symposium on Adaptive Processes*, 1980 (Albuquerque, NM), IEEE, p. 991–993. <https://doi.org/10.1109/CDC.1980.271950>
- [113] B. Duan, Y. Zhang, and J. Du, Electrostatic Forming Membrane Reflector Antenna, in *Large Deployable Satellite Antennas*, Springer Tracts in Mechanical Engineering, Springer, 2020, p. 241–271. [https://doi.org/10.1007/978-981-15-6033-0\\_10](https://doi.org/10.1007/978-981-15-6033-0_10)
- [114] S. Chodimella, J. Moore, J. Otto, and H. Fang, "Design Evaluation of a Large Aperture Deployable Antenna," *47th AIAA/ASME/ASCE/AHS/ASC Structures, Structural Dynamics, and Materials Conference*, May 1-4, 2006 (Newport, RI), AIAA, 2006. <https://doi.org/10.2514/6.2006-1603>
- [115] J. D. Moore, Jr., B. Patrick, P. A. Gierow, and E. Troy, “Design, Test, and Evaluation of an Electrostatically Figured Membrane Mirror,” *Proc. SPIE 5166, UV/Optical/IR Space Telescopes: Innovative Technologies and Concepts*, January 30, 2004 (San Diego, CA), SPIE, 2004. <https://doi.org/10.1117/12.509172>